

Copyright

by

Aaron Douglas Edens

2005

The Dissertation Committee for Aaron Douglas Edens certifies that this is the approved
version of the following dissertation:

Experimental Study of the Hydrodynamics of High Mach Number Blast Waves

Committee:

Todd Ditmire, Supervisor

Roger Bengtson

Herbert Berk

Richard Hazeltine

J. Craig Wheeler

Experimental Study of the Hydrodynamics of High Mach Number Blast Waves

by

Aaron Douglas Edens, B.S.

Dissertation

Presented to the Faculty of the Graduate School of

the University of Texas at Austin

in Partial Fulfillment

of the Requirements

for the Degree of

Doctor of Philosophy

The University of Texas at Austin

August, 2005

Acknowledgements

The work presented in this thesis would not have been possible without the help and support of far more people than I can recognize in this space. First and foremost I would like to thank my family, especially my parents Lynn and Gene Edens, for all their guidance and continued support over the years. They have provided the foundation on which the person I am has been built. I owe a debt of gratitude to my high school physics teacher, Richard Taylor, for sparking my interest in physics and first setting me down the path that has led me to this point and the faculty of the physics department at Harvey Mudd College for nurturing and refining that interest. I would like to thank my collaborators on the experiments I performed, with special thanks to John Edwards and John Porter, for helping to provide me with the resources and knowledge I needed to complete my research.

I would not have made it through graduate school without the help of the coworkers and friends that I have shared an office with for the better part of five years, Gilliss, Greg, and Will, who have unfailingly provided ideas when I've needed inspiration, hands when I've needed help, and friendship when I've needed support. Finally, I would like to thank my advisor, Todd Ditmire, who demonstrated an amazing ability to provide the resources and support necessary for an experiment enabling me to concentrate solely on the science of the experiment. Furthermore, he has been a constant input of energy and inspiration when my motivation was low or it did not seem like my efforts were bearing fruit and has provided knowledge and insight at every turn that has deepened my understanding of the physics I have studied.

Experimental Study of the Hydrodynamics of High Mach Number Blast Waves

Publication No. _____

Aaron Douglas Edens, Ph.D.

The University of Texas at Austin, 2005

Supervisor: Todd Ditmire

We have performed a series of experiments examining the properties of high Mach number blast waves. Preliminary experiments were conducted on the Janus laser at Lawrence Livermore National Laboratory while the majority of experiments were carried out on the Z-Beamlet laser at Sandia National Laboratories. We created blast waves in the laboratory by using 10 J- 1000 J laser pulses to illuminate millimeter scale solid targets immersed in gas. The experimental results can be grouped into three categories. Firstly, we confirmed the importance of line radiation on the evolution of the blast wave and that this importance increased with the atomic number of the gas used. This was determined through three measurements: Interferometric measurements of the size of the radiative precursor preceding the blast front, measurements of the blast wave trajectory, and measurements of the size of additional blast waves created by the radiation ablating material in the blast wave path. The second set of experiments examined the effect of the passage of a laser pulse on the subsequent evolution of the created blast wave. We find that the laser's passage creates a warm channel of gas where a blast wave travels at higher velocity than it does through unperturbed gas. This creates a bulge-like feature on the blast wave surface. This effect is magnified in higher atomic number gases where

multi-photon ionization is more prevalent, causing additional energy to be deposited in the gas. The final set of experiments studied the validity of theories forwarded to explain the dynamics of perturbations on astrophysical blast waves. These experiments consisted of a systematic scan of the decay rates of perturbations of known primary mode number induced on the surface of blast waves by means of a regularly spaced wire array. The amplitude of the induced perturbations relative to the radius of the blast wave was tracked and fit to a power law in time. Measurements were taken for a number of different mode numbers and background gasses and the results show qualitative agreement with previously published theories for the hydrodynamics of thin shell blast wave.

Table Of Contents

1. Introduction	1
1.1 Laser Astrophysics	2
1.2 Pulsed Laser Technology	4
1.2.1 High Power Lasers	4
1.2.2 High Energy Lasers	5
1.3 Supernova Remnant Studies	6
1.4 Plan for this Thesis	8
2. Shock Wave Physics	10
2.1 Acoustic Waves	10
2.2 Basic Shock Physics	15
2.3 Blast Waves	20
2.4 Radiative Processes	29
2.4.1 Bremsstrahlung	29
2.4.2 Free-Bound Radiation	34
2.4.3 Line Radiation	36
2.5 The Effect of Radiation on Blast Waves	39
3. Radiative Supernova Remnants	41
3.1 Supernova Remnants	41
3.2 Vishniac Overstability	48
3.3 Hydrodynamic Scaling for Blast Waves	58
4. Blast Wave Simulations	61
4.1 Astrophysical Simulations	61
4.2 Simulations of Laboratory Experiments	62
5. Experimental Setup	71
5.1 Laser Systems	72
5.2 Gasses and Target Materials	75
5.3 Wire Arrays	80
5.4 Diagnostic Systems	84
6. Diagnostics	89
6.1 Interferometers	89
6.1.1 Michelson Interferometer	92
6.1.2 Nomarski Interferometer	95
6.1.3 Mach-Zehnder Interferometer	96
6.1.4 Abel Inversion	98
6.2 Dark-Field Imaging	100
7. Experimental Description	103
7.1 Diagnosis of Radiation	103
7.1.1 Effect of Radiation on Blast Wave Trajectory	104
7.1.2 The Radiative Precursor	109
7.1.3 Ablation of Wires by Radiation	114
7.1.4 Estimate of Radiated Energy	116
7.2 Effect of Drive Laser on Blast Wave Evolution	118
7.3 Evolution of Induced Perturbations on Blast Waves	128
7.3.1 Planar Wire Array	129

7.3.2	Cylindrical Wire Array.....	136
7.3.3	Analysis Method.....	142
7.3.4	Comparison of Experimental Results to Theory.....	151
7.4	Conclusions.....	157
8.	Conclusion.....	158
8.1	Summary.....	158
8.2	Future Work.....	160
8.2.1	Growth of Perturbations.....	160
8.2.2	Collisionless Shocks.....	161
8.2.3	Extension of Mode Numbers.....	162
8.3	Conclusions.....	163
	References.....	164
	Vita.....	166

1. Introduction

The stars have always held a fascination for mankind. As technology has advanced our ability to study the stars has increased accordingly. Ancient peoples looked up at the stars and created stories for the figures they saw in the patterns and thus were born the constellations. Galileo used a telescope to examine the surface of Earth's moon and to see the moons of Jupiter launching a series of increasingly powerful optical telescopes including the 10 meter Keck telescope in Hawaii. In the last century telescopes have moved from the optical to a number of other regions of the electromagnetic spectrum, notably radio frequencies including the Very Large Array in New Mexico and the 305 meter Arecibo radio telescope in Puerto Rico. Space based telescopes such as the Hubble telescope and satellites avoid the distortions caused by the Earth's atmosphere and have further expanded our understanding of astrophysical phenomenon. At this point we are able to look across the sky and back billions of years to the early stages of the universe, and the precision of these observations continues to grow with time.

Unfortunately, even the most sensitive instrument can only observe the information that reaches Earth. Despite the sophistication of our instruments, this limits us to one view of a given event and keeps us at a distance. Computer simulations¹ provide a tool to help understand the implications of theories advanced to understand observation, and significant advances have been made in this area. However, computer simulations require validation and verification to be reliable. Observational data is limited in its applicability for this purpose as the exact conditions surrounding the onset of a given phenomena are rarely available. Furthermore, it is impossible to subtly change the conditions of an astrophysical event so that one can ensure that all of the important

physics is being included in a computer model. For this type of purpose, data from laboratory experiments is invaluable. These experiments are difficult as most astrophysical phenomena involve conditions that are very different from those on Earth. Advancements in laser technology have helped make examination of some astrophysical phenomena possible.

1.1 Laser Astrophysics

Lasers can provide a concentrated burst of energy in a small target volume over a short period of time which allows access to extreme states of matter. As laser science has advanced, the amounts of energy have increased and the time scales have shortened allowing access to increasingly extreme states of matter. However, even early on in their development in the 1960s, the promise of lasers for modeling astrophysical phenomenon was considered² but at that time the existing technology was inadequate to the task. Since that time lasers have consistently increased in power and energy, opening up increasingly exotic experimental conditions for laboratory study and now laser science has sufficiently matured to allow many astrophysical phenomena to be scaled for study in the laboratory. We can now test theories applicable to astrophysical systems in a controlled fashion, allowing measurement and control of parameters that previously could only be inferred from observations. This allows for the systematic testing of theories relevant to astrophysics and allows data to be gathered that enables the validation and verification of increasingly complex laser codes.

In 2001, Takabe³ conducted a survey of the state of laser astrophysics and its applicability to the laser fusion community and broke potential areas of study into eighteen areas based on two criteria. The first criteria was the type of physics and Takabe identified six potential areas of physics that would be of interest to the laser fusion community: laser-plasma interactions, electron energy transport, hydrodynamics and shocks, hydrodynamic instability, atomic physics and x-ray transport, and laser-produced relativistic plasma. The second criteria examined was the type of relationship to astrophysics: sameness, similarity, or resemblance. These criteria describe how close the physics in an experiment is to that of an astrophysical phenomenon. Sameness means there is no difference in the physics, similarity means that the physics in the laboratory is related to that in the astrophysical phenomenon by scaling laws, and resemblance means that no scaling law exists but that the phenomenon resemble each other. Based on these two criteria, Takabe identified fifteen astrophysical phenomena that could be studied in the lab and provide insight into laser fusion science ranging from examinations of the equation of state of the interiors of giant planets to studying relativistic cosmological jets. Number twelve on this list of fifteen is study of the Vishniac overstability, which Takabe sorts under the criteria of atomic physics and x-ray transport as the type of physics and that the laboratory experiments resemble the astrophysical phenomena.

1.2 Pulsed Laser Technology

Lasers are able to access increasingly exotic states of matter through improvement in one of three main areas of the laser, typified by three different types of laser systems.

The laser energy can be increased, an avenue epitomized by increasingly large and expensive long pulse laser facilities. Alternatively, the peak power of the laser pulse can be increased by shortening the duration of a laser pulse and lasers utilizing chirped pulse amplification (CPA) concentrate on this parameter. Finally, the wavelength of the laser can be reduced, creating higher energy photons which can penetrate deep into matter and provide unique benefits. X-ray lasers are typical of this path but facilities are just now being built that can reach the types of power and energy levels required for use in laboratory astrophysics experiments.

1.2.1 High Power Lasers

As the intensity of a laser pulse increases nonlinear effects such as self focusing become increasingly important⁴. These effects can begin to cause damage in the materials that make up a laser chain. Prior to 1985 the only way to increase the intensity of a laser pulse and avoid this problem was to lower the intensity of the laser beam while it is in the laser chain and amplify to full energy by increasing the area of the beam. The beam could then be focused once the danger to materials in the laser chain had passed enabling the increase in laser intensity desired. This method leads to increasingly large optics in the laser chain and correspondingly high costs. However in 1985 Strickland and

Mourou⁵ developed the technique of chirped pulse amplification (CPA). In lasers systems designed on this technique a very short duration laser pulse (down to a few femtoseconds in duration) is spread out spectrally in time by use of diffraction gratings. This allows the laser pulse to be amplified at a relatively low intensity. At the end of the laser chain a second set of gratings undo the temporal chirp, shortening the laser pulse once again and dramatically increasing the intensity. Using this technique very high power pulses ($> 10^{12}$ W) can be created by a system that fits in a university laboratory and is affordable for an independent researcher. Larger multi-million dollar high-power facilities employing this technique are capable of powers greater than 10^{15} W per pulse.

There are a number of laboratory astrophysics experiments that have been undertaken using high power short-pulse lasers. Utilizing the high magnetic fields that accompany the high electric field present when a high power laser pulse is focused to a small area, researchers on the Vulcan laser at Rutherford Appleton Laboratory^{6,7} have performed experiments examining the properties of collisionless shocks much like those common in the magnetized plasma of the interstellar medium. In addition, researchers at Lawrence Livermore National Laboratory have designed experiments⁸ looking at electron-positron plasmas. More experiments are listed in a survey of the state of collisionless plasmas in laser astrophysics done by Zakharov⁹.

1.2.2 High Energy Lasers

Alternatively to increasing the power of a laser pulse by shortening the length of a pulse, one can access new physics by increasing the energy in a laser pulse. In order to

do this, one needs a large amount of energy stored in an amplifier material leading to the need for large pulsed power electronics and large amounts of amplifier material. These concerns lead to high costs and require large physical areas limiting these types of lasers to large facilities. The most common type of large laser amplifier utilizes neodymium-doped glass as an amplifier material. This type of amplifier is utilized in the highest energy pulsed lasers currently under construction: the National Ignition Facility (NIF) at Lawrence Livermore National Laboratory in Livermore, California and the Laser Megajoule in Bordeaux, France. These are both multiple beam laser facilities capable of illuminating a target with several megaJoules of energy.

Use of high energy lasers in general allow for longer lasting, larger scale experiments as compared to the high power lasers described in the previous section, but at the cost of examining less extreme states of matter. One example of the type of astrophysically relevant experiment possible with large energy laser systems is the proposed experiment of Remington et al.¹⁰ on the NIF facility to study the equation of state of large planetary cores using laser generated shocks.

1.3 Supernova Remnant Studies

One of the areas discussed by Takabe in his survey of laser astrophysics is the physics of hydrodynamics and shocks, which has been one of the first areas available for study. Ryutov et al.¹¹ calculated scaling parameters to allow laboratory experiments to be hydrodynamically relevant to supernova remnants (SNRs) based on the dimensionless Euler number. Various experiments have looked at physics associated with early and late

time supernova remnants as well as general properties of collisionless shocks. Studies have been done looking at the early time behavior of SNRs have examined the onset of various instabilities, such as the Rayleigh-Taylor¹² and Richtmyer-Meshkov¹³ instabilities relevant to the mixing of material from different layers of the original star. Experiments in these areas are primarily done using high-energy laser systems.

The studies of late time SNRs have concentrated on radiative supernova remnants, such as portions of the Cygnus Loop and the Vela supernova remnant. There have been experiments on the structure of radiative shocks¹⁴ as well as their behavior^{15, 16}. These shocks exhibit a large amount of structure and Vishniac et al.¹⁷⁻¹⁹ developed a theory for the behavior of perturbations on blast waves which has received significant attention. They proposed an instability they called the pressure driven thin shell overstability and is now known as the Vishniac overstability to account for the structure seen in radiative SNRs. It is believed this overstability may play an important role in star formation^{20, 21}. There has since been a great deal of work to verify the theory. Computer simulations have seen the overstability grow from a small seed²² and have confirmed some of the theoretically determined growth rates²³. Experimentally, Grun et al.¹⁶ performed important early work looking at this theory in spherical blast waves, and Edwards et al.¹⁵ performed experiments in cylindrical geometry. These previous experiments will be discussed in chapter 7. This thesis describes a series of experiments we have undertaken that have quantitatively examined the predictions of Vishniac et al.'s theory.

1.4 Plan for this Thesis

The main purpose of this thesis is to examine experimentally the evolution of perturbations on high Mach number blast waves and compare the results to theoretical predictions. In order to do this the physics of shock waves in general and blast waves in particular is examined in Chapter 2. This includes a general description of disturbances in a fluid leading to the formation of a shock front. In addition, the various types of shock waves including blast waves are discussed and the effects of radiation on a blast wave are examined in this chapter. Chapter 3 looks at the physics of supernova remnants (SNRs) and the factors that need to be considered when designing an experiment to study them in the laboratory as well as an explanation of the previously published theory¹⁷⁻¹⁹ of Vishniac et al. for the evolution of perturbations on blast waves. The results of various simulations looking at both astrophysical and laboratory produced blast waves is summarized in Chapter 4. This includes the results of simulations performed in support of our specific experiments. Chapter 5 looks at the setup of the experiments done at two different laser facilities: the Janus laser at Lawrence Livermore National Laboratory and the Z-Beamlet laser at Sandia National Laboratories. Chapter 6 describes the working of all the diagnostics fielded during the experiments including several types of interferometer and a schlieren telescope. Chapter 7 summarizes all the experimental data and the analysis performed. The experiments described are sorted into three major areas: diagnosis of radiative effects, the effect of the passage of a drive laser on the subsequent blast wave evolution, and measurement of the evolution of perturbations on blast waves.

This chapter also contains a comparison of the results of the perturbation evolution experiments to the theoretical predictions described in Chapter 3. Finally, Chapter 8 summarizes the thesis and provides conclusions as well as possibilities for future work.

2. Shock Wave Physics

2.1 Acoustic Waves

All waves traveling through a fluid, including shock waves, are governed by conservation equations, including conservation of mass and momentum. The most commonly used forms of the equations for conservation of mass and momentum in hydrodynamics are the equation of continuity and Euler's equation²⁴⁻²⁶:

$$\frac{\partial \rho}{\partial t} + \vec{\nabla} \cdot (\rho \vec{v}) = 0 \quad (2.1.1)$$

$$\frac{\partial \vec{v}}{\partial t} + (\vec{v} \cdot \vec{\nabla}) \vec{v} = -\frac{1}{\rho} \vec{\nabla} p \quad (2.1.2)$$

Here ρ is the density of the fluid, \vec{v} is the fluid velocity, t is time, and p is the pressure of the fluid. If the wave is weak, a weak wave being one for which the velocity of fluid particles in the wave is small compared to the sound speed of the medium, then these equations can be linearized. Following Landau and Lifshitz²⁴, the pressure and density can be separated into mean values and small variations due to the wave according to $p = p_0 + p'$ and $\rho = \rho_0 + \rho'$, where the subscript 0 indicates the mean value and the primed variables are the small variations due to the wave. Also, the velocity of the particles, \vec{v} , is treated as a small parameter. Substituting into the equation of

continuity(2.1.1) and Euler's equation(2.1.2) and neglecting small quantities of second order or higher yields:

$$\frac{\partial \rho'}{\partial t} + \rho_0 \vec{\nabla} \cdot \vec{v} = 0 \quad (2.1.3)$$

for the equation of continuity and

$$\frac{\partial \vec{v}}{\partial t} + \frac{1}{\rho_0} \vec{\nabla} p' = 0 \quad (2.1.4)$$

for Euler's equation. Using these two equations and the assumption that the wave is adiabatic, the behavior of the wave can be described in terms of the velocity potential ϕ , where $\mathbf{v} = \nabla \phi$:

$$\frac{\partial^2 \phi}{\partial t^2} - c^2 \nabla^2 \phi = 0 \quad (2.1.5)$$

where

$$c^2 = \left(\frac{\partial p}{\partial \rho} \right)_s \quad (2.1.6)$$

Equation (2.1.5) has the form of a wave equation. The solutions to this equation are waves traveling with a characteristic speed c . In a fluid, such waves are known as sound waves and c is the sound speed.

As the speed of the particles in the wave increases towards the sound speed the small terms that were neglected in the above analysis become increasingly significant. The effect of these terms can be understood by examining the case of a plane wave defined to be traveling along the x-axis²⁴. In this case the equation of continuity(2.1.1) becomes:

$$\frac{\partial \rho}{\partial t} + \frac{\partial(\rho v)}{\partial x} = 0 \quad (2.1.7)$$

and Euler's equation(2.1.2) can be written as:

$$\frac{\partial v}{\partial t} + v \frac{\partial v}{\partial x} + \frac{1}{\rho} \frac{\partial p}{\partial x} = 0 \quad (2.1.8)$$

Equation (2.1.7) can be rewritten as:

$$\frac{\partial \rho}{\partial t} + \frac{d(\rho v)}{d\rho} \frac{\partial \rho}{\partial x} = 0 \quad (2.1.9)$$

and equation (2.1.8) as

$$\frac{\partial v}{\partial t} + \left(v + \frac{1}{\rho} \frac{dp}{dv}\right) \frac{\partial v}{\partial x} = 0 \quad (2.1.10)$$

Rearranging (2.1.9) we get:

$$\frac{\partial \rho / \partial t}{\partial \rho / \partial x} = - \frac{d(\rho v)}{d \rho} \quad (2.1.11)$$

or

$$\left(\frac{\partial x}{\partial t} \right)_{\rho} = \frac{d(\rho v)}{d \rho} = v + \rho \frac{dv}{d \rho} \quad (2.1.12)$$

This is an equation for the velocity of the wave at constant density. Similarly, (2.1.10) can be rearranged to obtain an equation for the velocity of the wave at constant fluid velocity:

$$\left(\frac{\partial x}{\partial t} \right)_v = v + \frac{1}{\rho} \frac{dp}{dv} \quad (2.1.13)$$

Noting that velocity of the wave is a function of only the fluid density implying constant v is the same as constant ρ , we can combine (2.1.12) and (2.1.13):

$$\rho \frac{dv}{d \rho} = \frac{1}{\rho} \frac{dp}{dv} \quad (2.1.14)$$

The right side of this equation can be rewritten using

$$\frac{dp}{dv} = \frac{dp}{d \rho} \frac{d \rho}{dv} = c^2 \frac{d \rho}{dv} \quad (2.1.15)$$

leading to the equation

$$\rho \frac{dv}{d\rho} = \frac{c^2}{\rho} \frac{d\rho}{dv} \quad (2.1.16)$$

or, rearranging

$$\frac{dv}{d\rho} = \pm \frac{c}{\rho} \quad (2.1.17)$$

Integrating this equation yields an expression for the fluid velocity, v .

$$v = \pm \int \frac{c}{\rho} d\rho = \pm \int \frac{dp}{\rho c} \quad (2.1.18)$$

This final form can be differentiated to get an equation for the speed of sound:

$$c(v) = \frac{1}{\rho} \frac{dp}{dv} \quad (2.1.19)$$

We can use this with (2.1.13) to get

$$\left(\frac{\partial x}{\partial t} \right)_v = v + c(v) \quad (2.1.20)$$

Integrating this equation yields:

$$x = t * (v + c(v)) + f(v) \quad (2.1.21)$$

Here $f(v)$ is an arbitrary function of the particle velocity. This equation describes a wave traveling with a velocity $u = v + c$. Because $c(v)$ varies with density, the speed of the wave varies with the position in the wave front and the shape of the wave changes with time. Landau and Lifshitz²⁴ show that $d(v + c)/d\rho > 0$, meaning that the speed of the wave increases with density. Because of this, the density peak of a compression wave travels faster than the front edge of the wave, causing the profile of the wave to steepen until the peak catches the front edge and the density ceases to be single valued as a function of position. This is a physical impossibility, and instead a discontinuity arises in the flow variables. This discontinuity is known as a shock front²⁴⁻²⁶.

2.2 Basic Shock Physics

A shock can be characterized by applying conservation laws across the shock front. Conservation of mass, momentum, and energy can be applied to deduce the properties of the shocked gas from the shock speed and the properties of the unshocked gas. In the rest frame of the shock front the equations for the conservation of mass, momentum and energy are:

$$\rho_1 u_1 = \rho_0 u_0 \quad (2.2.1)$$

$$p_1 + \rho_1 u_1^2 = p_0 + \rho_0 u_0^2 \quad (2.2.2)$$

$$\varepsilon_1 + \frac{p_1}{\rho_1} + \frac{u_1^2}{2} = \varepsilon_0 + \frac{p_0}{\rho_0} + \frac{u_0^2}{2} \quad (2.2.3)$$

Here

$$u_0 = -D \quad (2.2.4)$$

and

$$u_1 = -(D - v) \quad (2.2.5)$$

Where D is the velocity of the shock wave, v is the gas velocity in the rest frame of the undisturbed gas, u is the velocity of the gas in the rest frame of the shock front, p is the pressure of the gas, ρ denotes the gas's density and ε is the internal energy of the gas.

The subscript 0 denotes a property of the undisturbed gas and 1 denotes a property of the shocked gas an infinitesimal distance behind the shock front.

Using the conservation of mass equation (2.2.1) to eliminate u_1 from the conservation of momentum equation (2.2.2) we are left with:

$$u_0^2 = V_0^2 \frac{p_1 - p_0}{V_0 - V_1} \quad (2.2.6)$$

V here is the specific volume of the gas, i.e. $1/\rho$. If we instead eliminate u_0 the equation becomes

$$u_1^2 = V_1^2 \frac{p_1 - p_0}{V_0 - V_1} \quad (2.2.7)$$

Equations (2.2.6) and (2.2.7) can be used to eliminate the fluid velocity from equation (2.2.3). This yields a form of what is known as the Rankine-Hugoniot relations:

$$\varepsilon_1 - \varepsilon_0 = \frac{1}{2}(p_1 - p_0)(V_1 - V_0) \quad (2.2.8)$$

To solve this equation, the equation of state for the gas, $\varepsilon(p, \rho)$, must be known. Every material has its own equation of state. For most gasses the equation of state of a perfect gas with constant specific heats is used. This equation of state has the form:

$$\varepsilon = c_v T = \frac{1}{\gamma - 1} pV \quad (2.2.9)$$

c_v is the specific heat at constant volume and γ is the adiabatic index of the gas also known as the polytropic index or the isentropic exponent. The adiabatic index is equal to the ratio of the specific heats of the gas and is a measure of the number of energetic degrees of freedom the gas possesses, n .

$$\gamma = \frac{c_p}{c_v} = \frac{n+2}{n} \quad (2.2.10)$$

c_p is the specific heat at constant pressure. Applying equation (2.2.9) on either side of a shock front and taking the ratio we can see that

$$\frac{T_1}{T_0} = \frac{p_1 V_1}{p_0 V_0} \quad (2.2.11)$$

The equation of state (2.2.9) can be inserted into the conservation of energy equation(2.2.3):

$$\frac{\gamma}{\gamma-1} \frac{p_1}{\rho_1} + \frac{u_1^2}{2} = \frac{\gamma}{\gamma-1} \frac{p_0}{\rho_0} + \frac{u_0^2}{2} \quad (2.2.12)$$

Using equations (2.2.6) and (2.2.7), we can eliminate the velocities from this equation leaving what are known as the jump conditions.

$$\frac{p_1}{p_0} = \frac{(\gamma+1)V_0 - (\gamma-1)V_1}{(\gamma+1)V_1 - (\gamma-1)V_0} \quad (2.2.13)$$

$$\frac{V_1}{V_0} = \frac{(\gamma-1)p_1 + (\gamma+1)p_0}{(\gamma+1)p_1 + (\gamma-1)p_0} \quad (2.2.14)$$

In the limit of a very strong shock, i.e. that $p_0 \ll p_1$, (2.2.14) simplifies to:

$$\frac{V_1}{V_0} = \frac{\rho_0}{\rho_1} = \frac{\gamma-1}{\gamma+1} \quad (2.2.15)$$

As a shock increases in strength the pressure, velocity and temperature ratios across the shock front all increase and the density approached the limiting value of the strong shock conditions.

For real gasses a number of physical processes violate the assumption of constant specific heats used to formulate the equation of state used in this analysis. If molecular

disassociation or ionization occurs in the gas due to shock heating then the specific heats of the gas will change. Also, energy losses due to radiation mean the blast wave is no longer adiabatic. Despite these processes, the general formalism outlined above is often useful in describing a shock. When there is radiation or disassociation ongoing, an effective adiabatic index can be employed that treats processes such as ionization and radiation as effective degrees of freedom. As the amount of radiation increases, the number of effective degrees of freedom increases and the value of the effective adiabatic index approaches 1. It is often considered more appropriate to refer to the effective adiabatic index as the polytropic index as the system is no longer adiabatic.

The jump conditions for a shock wave assume time independence. To determine if they can be applied to a changing shock wave, the Knudsen number must be examined. The Knudsen number is the ratio of a mean free path of a shocked particle to the scale length over which the shock properties change. To the extent this parameter is small the steady state conservation laws may be used. Most astrophysical shocks are collisionless, and in this case the ion gyro-radius takes the place of the mean free path of the particles. The mean free path of a charged particle in cm, l , assuming single ionization of the gas is given by Zel'dovich and Raizer²⁶ as:

$$l \sim 3.5 * 10^4 \frac{T^2}{n} \quad (2.2.16)$$

Here T is the average temperature in degrees and n is the density in particles per cubic centimeter. For our experiments, given a 3 eV average temperature and 10 Torr pressure, the average mean free path is of the order of nanometers and from experiments the shock

thickness is of the order of tens of microns. This means the Knudson number is less than 10^{-4} and the analysis in this section is applicable to a high degree of accuracy.

2.3 Blast Waves

The time evolution of a shock wave depends on how it is created. A shock driven by a piston traveling at a constant velocity will also travel at a constant velocity away from the piston. In addition, assuming the pre-shock gas is homogeneous, the properties of the shocked gas will be homogeneous and constant. However, if the drive of the shock changes over time then the strength of the shock will change correspondingly. Moreover the thermodynamic variables will no longer be constant in the shocked region. The most extreme example of this occurs if the shock is produced by a brief point explosion. In this case what is known as a blast wave is created. A blast wave is also known as a decaying shock wave and decreases in strength over time as the energy of the initial explosion is spread over an increasingly large volume.

Because the shock strength of a blast wave varies over time, the properties of the shocked gas vary depending on position. If a homogenous pre-explosion material is assumed then there is a simple description explaining the general variation in thermodynamic variables behind the shock front. Initially, the explosion that creates the blast wave creates a small region of highly heated gas. This gas exerts a substantial pressure on the surrounding material and the heated material from this region begins to expand into the surrounding region. This material collides with and heats the surrounding material in an increasingly large volume. This volume expands faster than

the surrounding material can react, causing the heated material and thus the pressure of the region to pile up at the shock front and the profile of the density and pressure is thus peaked at the shock front. As the heated volume becomes larger, the initial energy of the explosion is spread over an increasing amount of gas, lowering the average temperature of the gas. Therefore the temperature of the shocked gas tends to rise as one approaches the center of a blast wave as these regions were shocked earlier and thus experienced a stronger shock. The pressure equilibrates over time and thus approaches a constant value at the center of the blast wave. As a result the density varies inversely with the temperature so as to maintain a constant pressure in this region. This means that the density increases with the radius of the blast wave even prior to the peak at the shock front. The general distribution of hydrodynamic properties of a gas near a blast wave is illustrated in Figure 1.

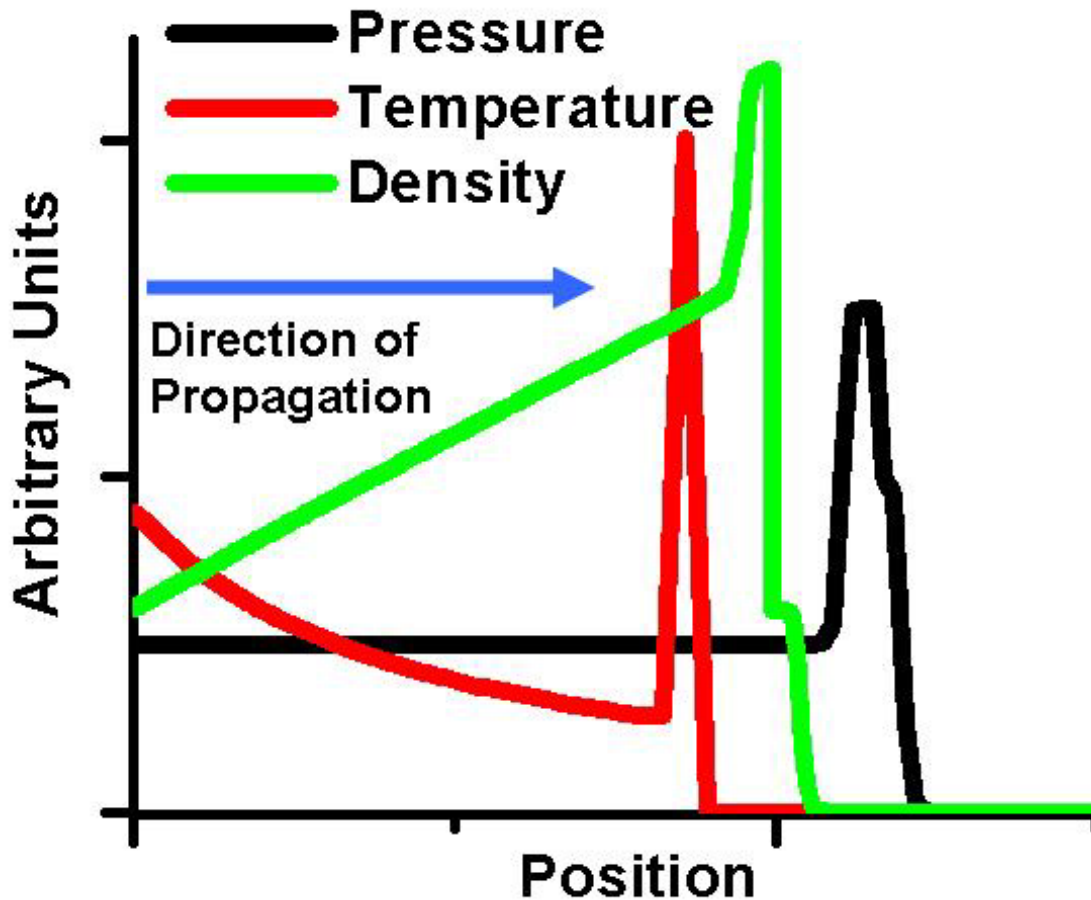


Figure 1. General distribution of hydrodynamic properties of gas near a blast wave. The three variables are offset from one another in position so they can all be seen.

A self-similar solution exists for the evolution of a blast wave assuming several conditions apply. The first is that the energy and pressure of the gas prior to being shocked are small compared to those of the shocked gas. The second condition is that the background material the blast is traveling into is uniform. Additionally the effect of viscosity must be negligible. Finally, the energy of the blast wave must be conserved. If these conditions are met then the only characteristic parameters of the system are the energy of the explosion and the density of the background gas. The blast wave evolution can then be described by the well known Taylor-Sedov solution. The only combination of the energy of the explosion and the density of the background gas that has units of

only length and time is the ratio of the energy of the blast wave (E) to the density of the background gas (ρ_0). This ratio has the units of $\text{length}^5/\text{time}^2$. Consequently the similarity variable will be:

$$\xi = R \left(\frac{\rho_0}{Et^2} \right)^{\frac{1}{5}} \quad (2.3.1)$$

and the blast wave radius (R) will evolve according to the equation:

$$R = \xi \left(\frac{E}{\rho} \right)^{0.2} t^{0.4} \quad (2.3.2)$$

Sedov used conservation of energy²⁷ to determine the similarity variable ξ in his original solution. The pressure behind the shock front varies as the average energy per unit volume, i.e. $p_1 \propto E/R^3$.

Zel'dovich and Raizer²⁶ present a simple analytical approximation proposed by Chernyi to understand strong explosions in a homogeneous medium that I shall follow here. The primary assumption of this approximation is that all of the mass in the blast wave is contained inside a thin shell behind the blast front. The density inside this layer is governed by the strong shock equations(2.2.15). The total mass swept up by the blast front, M , is equal to:

$$M = \frac{4}{3} \pi R^3 \rho_0 \quad (2.3.3)$$

Setting this equal to the mass in the thin shell determines the thickness of the shell, ΔR :

$$4\pi R^2 \Delta R \rho_1 = \frac{4\pi R^3}{3} \rho_0 \quad (2.3.4)$$

solving this equation for ΔR and using the conditions for a strong shock (2.2.15) yields

$$\Delta R = \frac{R}{3} \frac{\rho_0}{\rho_1} = \frac{R}{3} \frac{\gamma - 1}{\gamma + 1} \quad (2.3.5)$$

If one assumes the shell of mass is very thin then it follows that velocity of the gas in it is constant throughout and corresponds to the gas velocity just behind the front u_1 . In order to determine the force exerted by the hot gas behind the thin shell, we assume the shell is infinitesimally thin. Newton's law for the change of momentum of the thin shell, noting that the mass inside the shell varies with time, becomes:

$$\frac{d}{dt}(Mu_1) = 4\pi R^2 p_c = 4\pi R^2 \alpha p_1 \quad (2.3.6)$$

where p_c is the pressure pushing on the inside of the thin shell and can be written as a fraction α of the pressure behind the shock front p_1 . u_1 and p_1 can be rewritten in terms of D , the shock velocity, using (2.2.1), (2.2.4), (2.2.15), and (2.2.2).

$$p_1 = \frac{2}{\gamma + 1} \rho_0 D^2 \quad (2.3.7)$$

$$u_1 = \frac{2}{\gamma + 1} D \quad (2.3.8)$$

Plugging (2.3.7) and (2.3.8) into (2.3.6) yields

$$\frac{1}{3} \frac{d}{dt} R^3 D = \alpha D^2 R^2 \quad (2.3.9)$$

The time derivative can be rewritten as

$$\frac{d}{dt} = \frac{dR}{dt} \frac{d}{dR} = D \frac{d}{dR} \quad (2.3.10)$$

and this used to integrate (2.3.9)

$$D = aR^{-3(1-\alpha)} \quad (2.3.11)$$

where a is a constant of integration. Values for the constants a and α can be determined using conservation of energy. The kinetic energy of the gas is given by

$$E_k = \frac{Mu_1^2}{2} \quad (2.3.12)$$

The internal energy is predominately in the gas inside the cavity bounded by the thin shell. The gas exerts a pressure p_c and its internal energy is:

$$E_T = \frac{1}{\gamma-1} \frac{4}{3} \pi R^3 p_c \quad (2.3.13)$$

Substituting for αp_1 for p_c the total energy can be written as the sum of the kinetic and internal energies

$$E = \frac{1}{\gamma-1} \frac{4}{3} \pi R^3 \alpha p_1 + M \frac{u_1^2}{2} \quad (2.3.14)$$

We can use (2.3.7) and (2.3.8) to write the equation in terms of D

$$E = \frac{2}{\gamma^2-1} \frac{4}{3} \pi R^3 \alpha \rho_0 D^2 + \frac{2M}{(\gamma+1)^2} D^2 \quad (2.3.15)$$

Using equation for the total mass M (2.3.3) and the shock velocity D (2.3.11) we can rewrite this equation as

$$E = \frac{4\pi}{3} \rho_0 a^2 \left[\frac{2\alpha}{\gamma^2-1} + \frac{2}{(\gamma+1)^2} \right] R^{3-6(1-\alpha)} \quad (2.3.16)$$

For an energy conserving blast wave the energy is constant and so the dependence on R must disappear implying $\alpha = 1/2$. Using this result along with (2.3.11), (2.3.7), and (2.3.8) leads to some of the relationships previously mentioned for an energy conserving blast wave, such as

$$R \sim t^{2/5}, p_1 \sim R^{-3}, u_1 \sim R^{-3/2}, \text{ and } D \sim R^{-3/2}.$$

Similarly, using $\frac{1}{2}$ for α we solve (2.3.16) for a

$$a = \left[\frac{3}{4\pi} \frac{(\gamma-1)(\gamma+1)^2}{(3\gamma-1)} \right]^{\frac{1}{2}} \left(\frac{E}{\rho_0} \right)^{\frac{1}{2}} \quad (2.3.17)$$

This equation can be used to get an approximate value for the similarity variable if we note the fact that

$$R = \left(\frac{5}{2} a \right)^{\frac{2}{5}} t^{\frac{2}{5}} = \xi \left(\frac{E}{\rho_0} \right)^{\frac{1}{5}} t^{\frac{2}{5}} \quad (2.3.18)$$

The similarity variable can then be written as

$$\xi = \left(\frac{5a}{2} \sqrt{\frac{E}{\rho_0}} \right)^{\frac{2}{5}} \quad (2.3.19)$$

The analysis resulting from the Chernyi approximation can be repeated for cylindrical and planar expanding blast waves and in those cases the relationship between the radius of the blast wave and the other variables changes. In cylindrical geometry this relationship becomes:

$$R = \xi \left(\frac{Et^2}{\rho_0} \right)^{\frac{1}{4}} \quad (2.3.20)$$

and in planar coordinates:

$$R = \xi \left(\frac{Et^2}{\rho_0} \right)^{\frac{1}{3}} \quad (2.3.21)$$

If the condition of energy conservation is violated then this behavior is modified. If there is energy lost, via radiation or some other means, then the blast wave will tend to slow down faster than the Taylor-Sedov solution. There are only two scenarios where exact analytical solutions exist for the behavior of a radiative blast wave. If all of the gas in the blast front is cooled by radiation but the inner gas remains hot then the blast wave will follow what is known as the pressure driven snowplow solution. In this case a cold dense shell of gas is pushed out by the pressure of the low density hot gas interior to the blast front. In this solution the blast wave trajectory, R , goes as $t^{2/7}$ instead of the $t^{0.4}$ behavior of the Taylor-Sedov solution. If the gas interior to the blast front is also cooled by radiation then the momentum conserving snowplow regime is reached. Here the thin dense shell of cold gas coasts into the surrounding medium with constant momentum. In this solution the blast wave slows down very quickly and R goes as $t^{2/8}$. The derivation of the pressure driven snowplow solution is fairly complicated and relies on assumptions about the polytropic index of the gas. However, the momentum conserving snowplow solution is relatively straightforward and can be found by setting the change of momentum of the blast wave equal to zero. We first start with a definition of the momentum (P) in terms of the blast wave mass (M) and its velocity (U):

$$P = MU \quad (2.3.22)$$

The rate of change of the momentum of the blast wave is then given by:

$$\dot{P} = M\dot{U} + \dot{M}U = 0 \quad (2.3.23)$$

A dot above a quantity denotes a derivative with respect with time. The mass of the blast wave can be approximated by the product of the total volume swept up by the blast wave and the density of background gas (ρ):

$$M = \frac{4}{3} \pi R^3 \rho \quad (2.3.24)$$

Here R is the radius of the blast wave. The derivative of the mass is then:

$$\dot{M} = 4\pi R^2 U \rho \quad (2.3.25)$$

U is again the velocity of the blast wave and is equal to the derivative of its radius.

Plugging these equations into (2.3.23) yields:

$$0 = 4\pi R^2 \rho \left(\frac{R\dot{U}}{3} + U^2 \right) \quad (2.3.26)$$

The coefficient of the right side of this equation can be ignored as $R = 0$ is not a case of interest. This leaves us with:

$$-U^2 = \frac{R\dot{U}}{3} \quad (2.3.27)$$

Noting that U is the time derivative of R, this equation can be rewritten as:

$$\frac{\dot{U}}{U} = -\frac{3U}{R} = \frac{-3\dot{R}}{R} \quad (2.3.28)$$

Integrating the outside parts of this equation give us:

$$\ln(U) = \ln(R^{-3}) + c \quad (2.3.29)$$

c is a constant of integration. Raising e to both sides yields:

$$U = e^c R^{-3} \quad (2.3.30)$$

but $U = \frac{dR}{dt}$ and so (2.3.30) can be rewritten as:

$$R^3 dR = e^c dt \quad (2.3.31)$$

this can be integrated to yield:

$$\frac{1}{4}R^4 = e^c t + d \quad (2.3.32)$$

Ignoring our second constant of integration d , we get the result we were looking for that $R \propto t^{2/8}$.

2.4 Radiative Processes

There are three main radiative processes that can occur in a blast wave: free-free or bremsstrahlung radiation, free-bound radiation, and bound-bound or line radiation.

2.4.1 Bremsstrahlung^{26, 28}

Bremsstrahlung radiation occurs when one charged particle is accelerated in the Coulomb field of another charged particle. Quantum mechanically, since bremsstrahlung radiation involves transitions in the continuum of the ion energy levels, the spectrum of radiation produced is continuous and in general governed by energy spectrum of the electrons in the plasma.

A general understanding of the radiation can be gathered by looking at the classical dipole approximation to the radiation. The radiated power of a system of moving particles, P , in the dipole approximation goes as

$$P = \frac{2\ddot{d}^2}{3c^3} \quad (2.4.1)$$

Where c is the speed of light and d is the dipole moment of the system, which can be written as:

$$d = \sum_i q_i \vec{r}_i \quad (2.4.2)$$

Where q_i and r_i are the charge and position of element i of the dipole. Because the dipole moment of two like particles goes as the center of mass, and is therefore constant, radiation from two body collisions must involve unlike particles. The most common situation in a plasma is when an unbound electron encounters an ion and is accelerated by its' Coulomb field. Some of the energy of the electron is radiated away causing the electron to slow down. Quantum mechanically this can be thought of as the electron entering the continuum energy levels of the potential of the ion and decaying to a lower continuum state with the emission of a photon with appropriate energy.

A general understanding of the bremsstrahlung process can be obtained by using the small scattering approximation. This approximation assumes several things. The first is use of the dipole approximation. The second assumption arises from the fact that the acceleration of the electron in the electron-ion collision is larger than the acceleration of the ion by the inverse ratio of their masses; therefore the acceleration of the ion can be neglected. The final assumption of the small scattering approximation is that the motion of the electron is unchanged by the encounter, in other words the momentum and energy

of the emitted photon are a small fraction of that of the electron. In this assumption the second derivative of the dipole moment can be written as

$$\ddot{\vec{d}} = -e\dot{\vec{v}} \quad (2.4.3)$$

An estimate can be obtained for the derivative of the velocity. Since we are assuming the change of motion of the electron is small, the total velocity change of the electron can be estimated by looking only at the component of acceleration due to the Coulomb force normal to the path of the electron:

$$\dot{\vec{v}} = \frac{F_{\text{coulomb}}}{m} = \frac{Ze^2}{mr^2} \quad (2.4.4)$$

Here Z is the effective charge state of the ion, Z is the charge state of the ion, r is the distance from the ion and F_{coulomb} is the Coulomb force. The impact parameter, b , can be used in place of the radius. The impact parameter is the distance of closest approach of the electron to the ion. The time over which the electron interacts with the ion can be estimated as $\tau=b/v$, where again b is the impact parameter and v is the velocity of the electron.

The emitted power therefore goes as

$$P = \frac{2e^2\dot{\vec{v}}^2}{3c^3} = \frac{2Z^2e^6}{3c^3m^2b^4} \quad (2.4.5)$$

The time over which the electron radiates can be estimated as $t = b/v$. Therefore the total energy emitted by an electron during a bremsstrahlung event is approximately given by:

$$\Delta E = P^* t = \frac{2}{3} \frac{Z^2 e^6}{m^2 c^3 b^3 v} \quad (2.4.6)$$

For comparison with free-bound radiation, it will be convenient to follow Zeldovich and Raizer²⁶ and consider the total radiated energy from an infinite ring of electrons of unit flux incident on a single ion. The total emitted power is then given by:

$$q = \int_0^\infty \Delta E 2\pi b db \quad (2.4.7)$$

The majority of power radiated during a bremsstrahlung event occurs at frequencies ν of the order of $1/(2\pi t) \sim \nu/(2\pi b)$. Therefore, the majority of electrons within a small band $\Delta\nu$ of a given frequency ν are predominantly produced by electrons with impact parameters within a small range Δb of b , where $b \sim \nu/2\pi\nu$. The range of impact parameters Δb is given by taking the derivative of the estimate for b :

$$\Delta b \approx \frac{\nu}{2\pi\nu^2} d\nu \approx \frac{2\pi b^2}{\nu} d\nu \quad (2.4.8)$$

This implies that the total power radiated at a given frequency is

$$dq_\nu \approx \Delta E 2\pi b db \approx \frac{4\pi}{3} \frac{Z^2 e^6 db}{m^2 c^3 b^2 \nu} \approx \frac{8\pi^2}{3} \frac{Z^2 e^6}{m^2 c^3 \nu^2} d\nu \quad (2.4.9)$$

The exact solution is given in Landau and Lifshitz's book²⁹ and is given by:

$$dq_\nu = \frac{32\pi^2}{3\sqrt{3}} \frac{Z^2 e^6}{m^2 c^3 v^2} dv \quad (2.4.10)$$

for $\nu \gg \frac{mv^3}{2\pi Ze^2}$ and

$$dq_\nu = \frac{32\pi}{3} \frac{Z^2 e^6}{m^2 c^3 v^2} \ln\left(\frac{mv^3}{1.78\pi Ze^2}\right) dv \quad (2.4.11)$$

for $\nu \ll \frac{mv^3}{2\pi Ze^2}$. It will prove useful for later comparisons to integrate (2.4.10):

$$q_\nu = \frac{32\pi^2}{3\sqrt{3}} \frac{Z^2 e^6}{m^2 c^3 v^2} \nu = \frac{dq_\nu}{d\nu} \nu = \frac{dq_\nu}{d\nu} \frac{E}{h} \quad (2.4.12)$$

where in the last equality we have used the relation for the energy of a photon $E=h\nu$ and h is Planck's constant.

2.4.2 Free-Bound Radiation

If the energy lost by an electron during a bremsstrahlung event is large enough, it will cause the electron to be captured by the ion it is passing by. Quantum mechanically it can be thought of as a transition by the electron from a continuum state of the ion to a bound state. Since it involves transition from the continuum, the emitted radiation is continuous across its spectral range. Following Zel'dovich and Raizer, we can examine the capture of an electron by a hydrogen-like ion. The energy levels of such a hydrogenic atom are related to the principal quantum number n , which can be any positive integer value, according to:

$$E_n = -\frac{I_H Z^2}{n^2} = -\frac{I}{n^2} \quad (2.4.13)$$

I_H is the ground state potential of hydrogen and $I = I_H Z^2$ is the ground energy of an arbitrary hydrogenic atom. The time averaged kinetic energy of a bound electron is equal to the negative of one-half the potential energy and is also equal to the negative of the total energy. Therefore:

$$E_{kin} = \frac{m\bar{v}^2}{2} = \frac{I}{n^2} = \frac{I_H Z^2}{n^2} \quad (2.4.14)$$

For large n the levels look nearly continuous and motion of the electron is quasi-classical.

The cross section for electron capture into a specific energy level, σ_{cn} , is²⁶:

$$\sigma_{cn} = \frac{1}{h\nu} \frac{\Delta q_\nu}{\Delta n} = \frac{1}{h\nu} \left(\frac{dq_\nu}{d\nu} \right) \frac{\Delta \nu}{\Delta n} \quad (2.4.15)$$

In order to compare bound free radiation to bremsstrahlung radiation we can follow Zeldovich and Raizer²⁶ and look at the total energy radiated away by an infinite ring of electrons incident on an atom due to free-bound radiation, q_{bf} . This quantity is the energy of the radiated photon times the cross section for that photon to be emitted and given by:

$$q_{bf} = \sum_n h\nu \sigma_{cn} \quad (2.4.16)$$

This can be compared to the equivalent quantity for bremsstrahlung radiation, (2.4.12).

Using (2.4.14) we can estimate the spacing between high n energy levels.

$$\left| \frac{dE_n}{dn} \right| = -\frac{dE_n}{dn} = \frac{2I_H Z^2}{n^3} \quad (2.4.17)$$

Plugging this equation into (2.4.15) and then into (2.4.16) yields:

$$q_{bf} = \frac{I_H Z^2}{h} \left(\frac{dq_\nu}{d\nu} \right) \sum_n \frac{2}{n^3} \quad (2.4.18)$$

The summation is of order unity and can be ignored. Therefore the ratio of the energy due from free-bound transitions to that of bremsstrahlung radiation is:

$$\frac{q_{bf}}{q_{brems}} = \frac{I_H Z^2}{E} \quad (2.4.19)$$

where E is the energy of the emitted photon. Therefore the ratio of energy emitted is the ratio of the energies of the transitions involved in each process. Since the free-bound transitions can involve bound states with substantial potential energy the transition energy can increase by a factor of several.

2.4.3 Line Radiation

Line radiation involves excited electrons bound to an atom. These electrons can emit a photon and decay into a lower energy state. Because of the discrete nature of energy levels in an atom, the possible frequencies of radiation are limited. This means the spectrum of line radiation appears as a series of discrete peaks, or lines. The intensity of radiation at a specific frequency is governed by the energy level populations in the atom and the transition rates between levels involved in the transition. While transitions between many levels can occur and line radiation in the visible portion of the spectra is a useful diagnostic, the majority of the energy dynamics will occur for transitions between the ground state and the excited states. The energy gap between the ground states of an atom and the 1st excited state represent the majority of the total binding energy of the ground state of the atom. Therefore any transitions between excited states will be less energetic than transitions between the ground states and excited states. A visual representation of this fact can be seen in the Grotian diagrams for neutral nitrogen and xenon (the gasses used in our experiments) shown in Figure 2 and Figure 3 respectively. The vertical axis on these graphs is the energy of each quantum level relative to the

ground state and the mauve line is the energy at which the neutral atom ionizes. It is clear that a majority of the energy of ionization is in the transition from the ground state to the 1st excited state. It should be noted that nitrogen has a triplet ground state which accounts for the 3 energy levels between 0 and 4 eV.

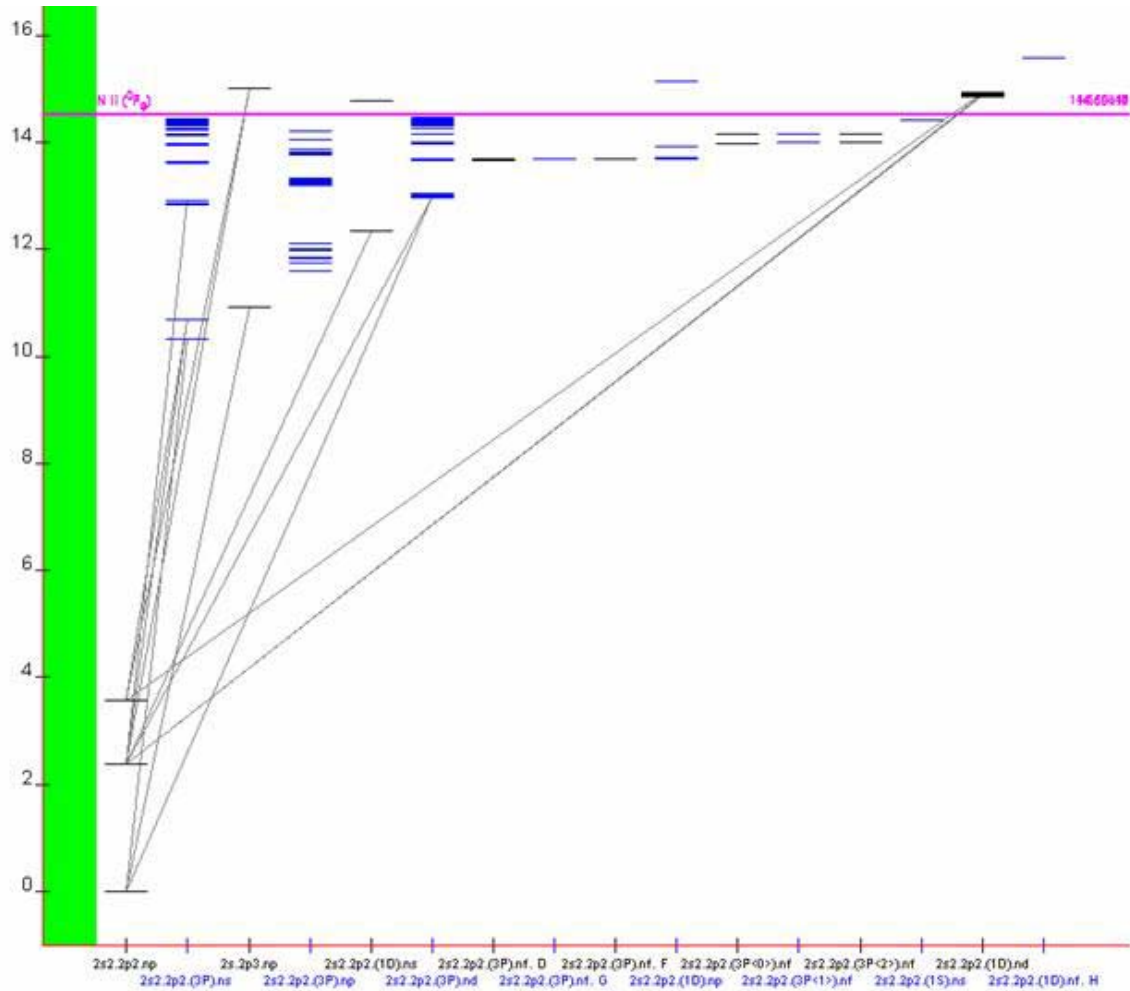


Figure 2. Grotian diagram for neutral nitrogen courtesy NIST (www.nist.gov). Energy levels are shown in eV and only the strongest transitions are listed. Notice that the shown transitions all have more than a 6 eV energy difference between levels.

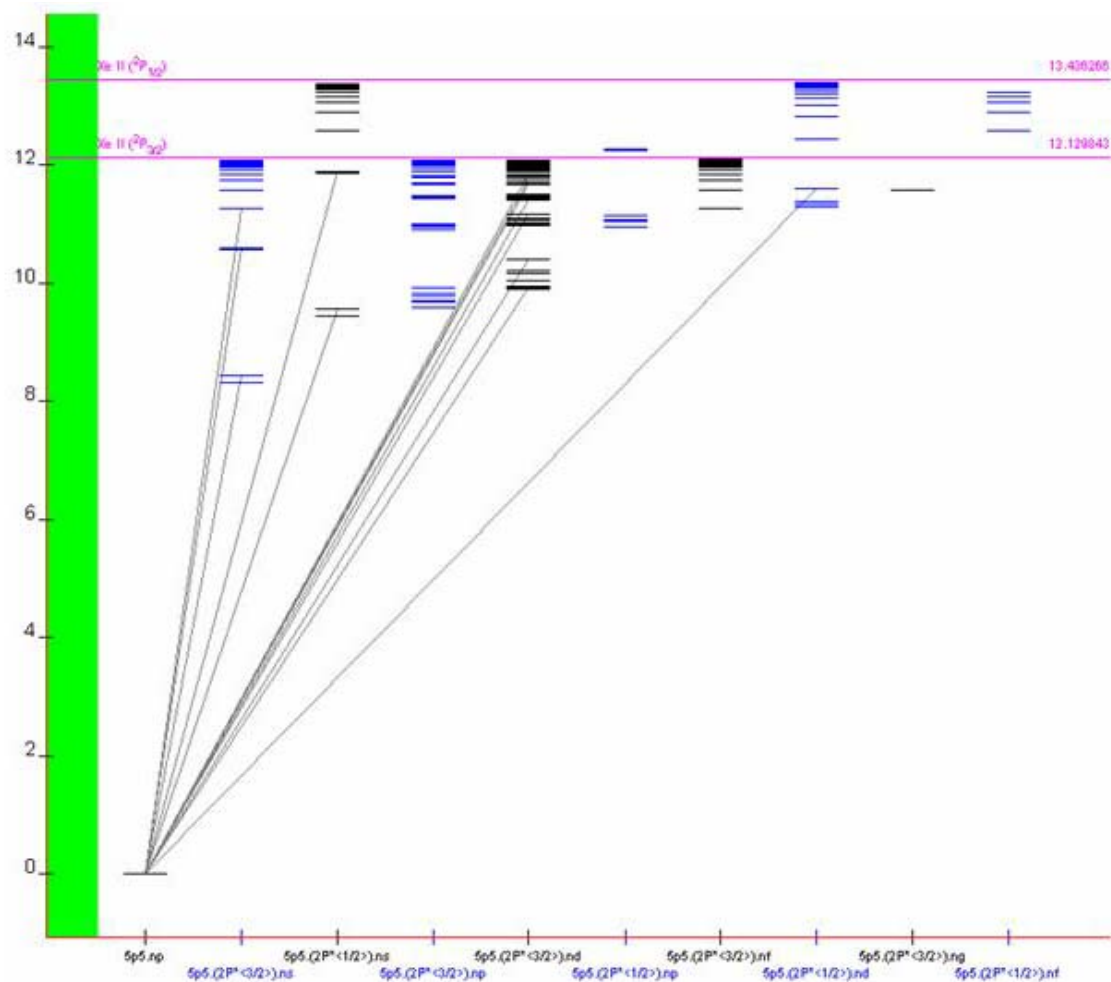


Figure 3. Grotian diagram for neutral xenon courtesy NIST (www.nist.gov). Energy levels are shown in eV and only the strongest transitions are listed. Notice that the shown transitions all have more than a 6 eV energy difference between levels.

2.5 The Effect of Radiation on Blast Waves

The importance of radiation energy losses on the hydrodynamics of the blast wave is measured by the dimensionless cooling parameter, ε^* ³⁰. This parameter measures the fraction of energy lost at the blast front by radiation. An ε^* of 0 indicates no net energy loss due to radiation, while an ε^* of 1 implies full radiative cooling and the onset of the snowplow regimes. An $\varepsilon^* < 0$ is indicative of a net absorption of energy and is known as the detonation case.

For the case of $1 > \varepsilon^* > 0$ Liang and Kielty³⁰ proposed an approximate analytical solution that attempted to quantify several effects of radiation on blast wave evolution. The first effect of radiation is on the polytropic index of the blast wave. The polytropic index of the radiating gas can be calculated from the polytropic index of the pre-shock gas and the cooling rate ε^* according to the formula:

$$\varepsilon^* = 4 \frac{(\gamma - \gamma_1)}{(\gamma - 1)(\gamma_1 + 1)^2} \quad (2.5.1)$$

Here γ is the polytropic index of the pre-shock gas and γ_1 is the polytropic index of the radiating gas. In the adiabatic case $\varepsilon^* = 0$ and one recovers that $\gamma_1 = \gamma$.

The second effect of radiation is a change in the time evolution of the blast wave trajectory. Depending on the size of ε^* , the trajectory of a spherical blast wave can evolve as anything from the Taylor-Sedov $t^{0.4}$ to the momentum conserving snowplow $t^{0.25}$. Liang and Kielty³⁰ modify the Chernyi approximation²⁶ described earlier in this

chapter to get an estimate of the temporal exponent as a function of the radiative energy loss. They show that the α in (2.3.11) is related to the polytropic indices index according to the equation

$$4\alpha^2 + 2\alpha(\gamma - 2) + (1 - \gamma_1) = 0 \quad (2.5.2)$$

Finally, the coefficient of the blast wave trajectory can be used to deduce the volume over which the initial energy was injected to create the blast wave. To do this Liang and Kielty³⁰ start with the following equation for the blast wave trajectory with an arbitrary α :

$$R = [(4 - 3\alpha)at]^{(4-3\alpha)} \quad (2.5.3)$$

They then solve the general form of (2.3.18) for the variable a and get

$$a = R_0^{(3-6\alpha)/2} \left(\frac{3E_0}{8\pi\rho_0} \right)^{0.5} \quad (2.5.4)$$

This provides a relationship between the initial deposited energy E_0 and the radius of the initial energy deposition sphere R_0 .

3. Radiative Supernova Remnants

3.1 Supernova Remnants

When a star explodes in a supernova it releases on the order of 10^{51} ergs of energy. This explosion moves out, sweeping up the surrounding interstellar medium (ISM). The expanding remains of the explosion are known as a supernova remnant (SNR). A SNR goes through up to four stages of evolution. The first stage is the explosion of the star. This phase is also known as the ejecta dominated phase and in it the constituents of the explosion fly ballistically into space with approximately constant velocity. This stage ends when approximately as much matter has been swept up as was in the initial explosion. At this point a shock front forms. Because of the low density of the interstellar medium and the relatively significant background magnetic field, most interstellar shocks are collisionless. For a collisionless shock energy is dissipated by interactions with the magnetic field instead of collisions between particles, as is common for shocks in denser media. Most SNRs at some point in their evolution meet the conditions described in the previous chapter for the self-similar Taylor-Sedov solution for blast wave evolution. Therefore, the 2nd stage of existence for a SNR is known as the Taylor-Sedov phase. During this phase the energy of the blast wave remains constant while the total mass swept up increases. This causes the energy of the blast wave to be spread over an increasingly large volume and the blast wave to slow down in time. The trajectory of the blast wave will follow the Taylor-Sedov $R \propto t^{0.4}$ solution. Once the

energy of the initial explosion is spread over a sufficient volume, the SNR enters its final phase of existence. At this point the strength of the SNR has decayed to the point it is no longer a blast wave but rather a sound wave. The strength of that sound wave continues to decrease and eventually the wave becomes indistinguishable from the background ISM.

If the conditions in the ISM encountered by the SNR are right then it is possible for a SNR to enter a stage between the Taylor-Sedov phase and the decay phase known as the radiative phase. When a star goes supernova the material in the initial explosion is heated to many keV average temperature. At these temperatures, the gas involved is fully ionized and there are no opportunities for bound-free or line radiation. Once the SNR cools below approximately 3 keV the constituent gas begins to recombine and line radiation and free-bound radiation become important. At this time the amount of energy lost via radiation increases significantly. The spectrum of light emitted by the SNR at this time changes from a smooth bremsstrahlung-like spectrum, to one dominated by spectral lines as is illustrated for the Cygnus Loop in Figure 4. If the density of the ISM is high enough this radiation becomes the dominant energy loss mechanism and the SNR will enter the radiative phase. In the radiative phase the energy loss via radiation causes the velocity of the SNR decreases more quickly than in the energy conserving Taylor-Sedov phase. The trajectory in this phase may follow the pressure-drive snowplow or momentum-conserving snowplow solutions mentioned in the previous chapter.

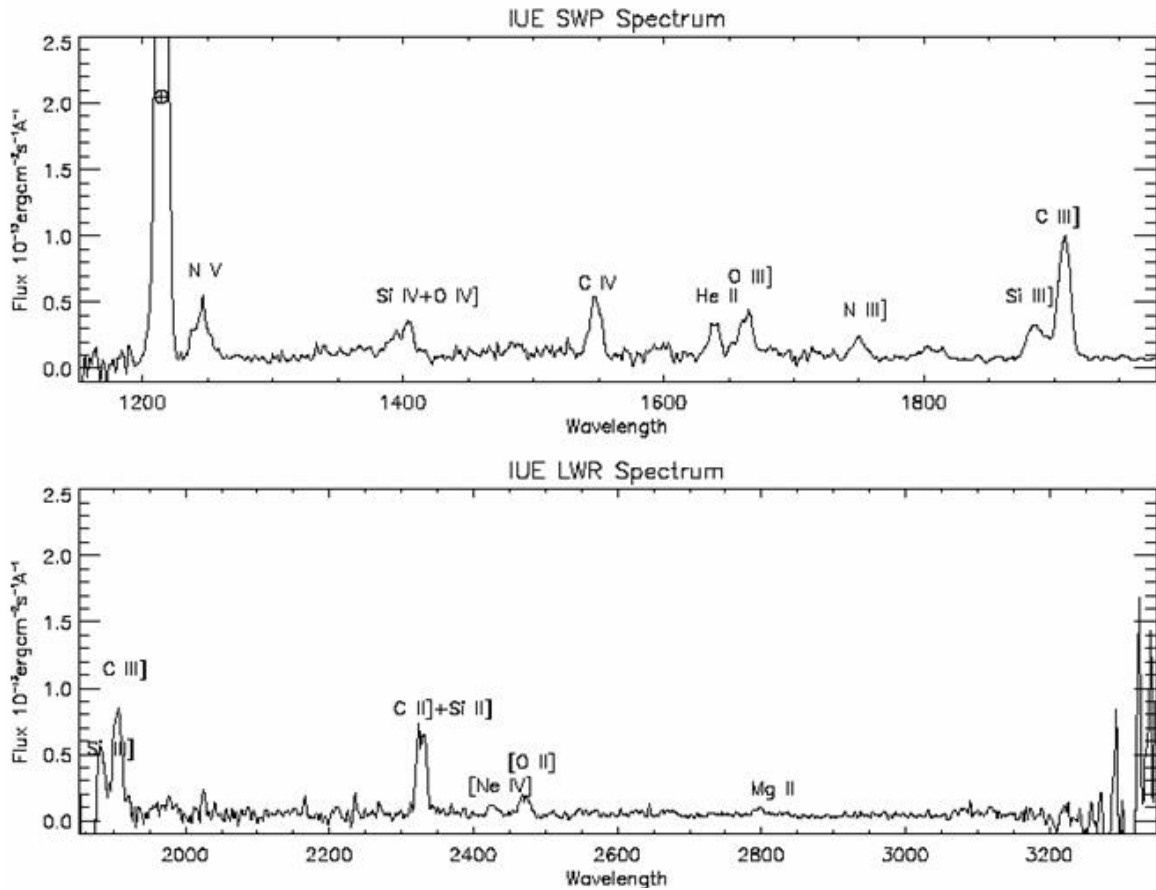


Figure 4. Spectrum of UV Emission from Miller Position 1 in the Cygnus Loop, one of the canonical examples of a radiative supernova remnant. This figure is taken from Raymond et al. *Ap. J*, 560, P.763. Notice that the spectrum is completely dominated by the spectral lines.

Ryutov et al.¹¹ suggested that there were two main conditions for a SNR to enter a radiative phase. The first condition is that radiation is the dominant cooling mechanism, exceeding any hydrodynamic cooling rates. To provide an estimate of when this condition would be met they compared the cooling time due to radiation to the characteristic convective cooling time. The convective cooling time is set by the characteristic gas dynamic time h/s , where h is the characteristic scale length of the SNR and s is the sound speed of the heated gas. In the paper they use the sound speed for a gas with an adiabatic index of $5/3$:

$$s \left[\frac{cm}{s} \right] = 1.3 * 10^6 \sqrt{\frac{(Z+1)T[eV]}{A}} \quad (3.1.1)$$

Here A is the atomic number of the gas, T is the temperature in electron volts, and Z is the average ion charge state. Quantities in [] are units. For the radiative cooling time, energy radiated away by bremsstrahlung radiation is calculated. To do this the energy density of the shocked gas in the SNR is divided by the radiated power per unit volume. This yields a radiative cooling time of:

$$\tau_{thin} [s] = 2.4 * 10^{-12} \frac{(Z+1)T[eV]}{Zn_i [cm^{-3}] \Lambda_n} \quad (3.1.2)$$

Where Λ_n is the normalized cooling rate³¹ in ergs cm³ sm⁻¹ and n_i is the density of ions. For bremsstrahlung radiation Λ_n is $1.7 * 10^{-25} Z_{eff}^2 T(eV)^{1/2}$. For regions that have a shocked temperature from 30 eV to 3 keV line and free-bound radiation can have a significant effect on the cooling time, reducing it by up to two orders of magnitude. However, as a first approximation the bremsstrahlung rate alone can be used.

The second condition for a SNR to be in a radiative phase is for the radiation produced to escape. This is necessary for there to be a net energy loss by the SNR. Saying that radiation can escape the region of the SNR is equivalent to saying the SNR is optically thin. Ryutov et al. examined this condition by comparing the mean free path of bremsstrahlung photons to the scale length of the SNR. The bremsstrahlung mean free

path was determined by averaging over a Planckian distribution of photons in a fully ionized plasma, also known the Rosseland mean. This yields a mean free path of:

$$\bar{l}_{brems} [cm] = 1.7 * 10^{37} \frac{(T[eV])^{\frac{7}{2}}}{Z^3 (n_i [cm^{-3}])^2} \quad (3.1.3)$$

Both conditions for a radiative SNR can be written as bounds on the scale length of the SNR for a given temperature and density, with the bremsstrahlung mean free path providing an upper bound and the product of the sound speed and radiative cooling time serving as the lower bound. Or, equivalently, for a given scale length of the SNR, these two equations define a region in temperature and density space where a SNR will enter a radiative phase. This region is shown visually in Figure 5 for both astrophysical and laboratory conditions. The black curves represent the condition that radiative cooling be dominant and the red curves show the boundary at which the SNR becomes optically thick. Radiative SNRs are possible in the region between these two curves. As previously mentioned, line and bound-free radiation can have a significant impact on the conditions for a radiative blast wave. In general, between a few eV and 3 keV, both curves in the figure will tend to bend towards lower density for the same temperature. Following Ryutov et al. hydrogen gas and a scale length of 10^{16} cm was chosen for the astrophysical parameters. In practice, the condition on the radiation cooling time is the critical one, and SNRs only enter a radiative phase when encountering clouds of matter in the ISM, often material sloughed off by a star prior to its going supernova. As a quick guide, McKee and Draine³² showed that radiative blast waves would travel with an

approximate velocity range of 110 km/s – 200 km/s. For the laboratory conditions, we looked at xenon gas and a 1 cm scale length. The green triangle in the laboratory graph section highlights the parameter range where we might expect radiative blast waves. These considerations were taken into account when designing the experiments described in later chapters.

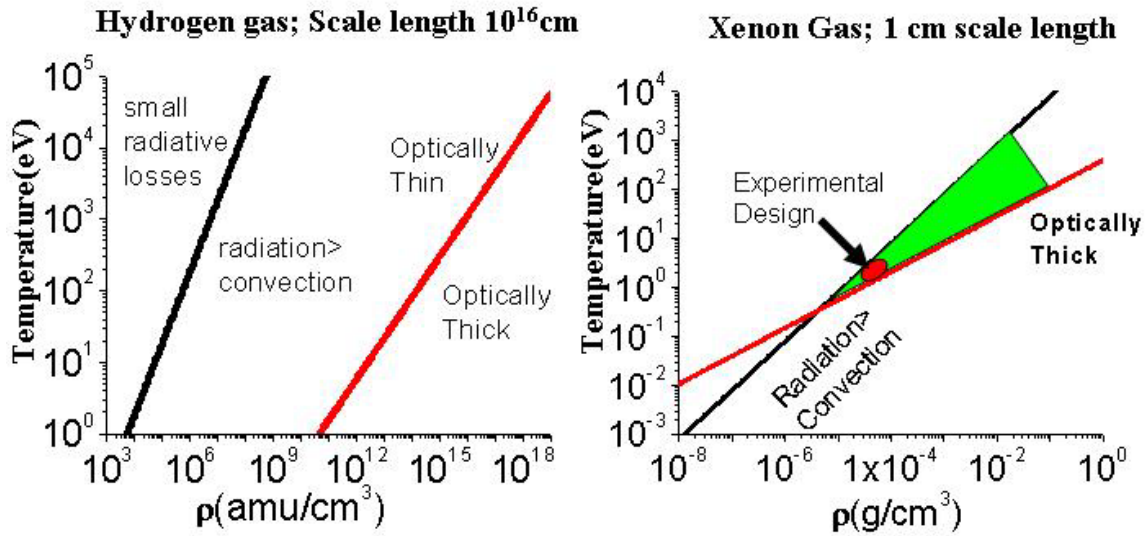


Figure 5. Conditions determined by Ryutov et al. for a supernova remnant (SNR) to be radiative. There are two main conditions for a radiative SNR. Radiative cooling must exceed hydrodynamic cool (right of black line) and the SNR must be optically thin to the radiation (left of the red curve). The graph on the left is for an astrophysical environment. The graph on the right shows the results for laboratory conditions. The green triangle in the left graph highlights the desired parameter space and the red blob indicates where experiments were designed to exist.

Several effects accompany the onset of a radiative phase in a supernova remnant. One is that some of the radiation produced by the shocked gas is absorbed in the background material outside the blast front. This creates a region of warm ionized gas preceding the shock front of the SNR. This region of ionized gas is known as a radiative precursor. The idea of a radiative precursor is illustrated in Figure 6. A second important effect accompanying the onset of the radiative phase is the thinning of the blast front. As

discussed previously, radiation provides an effective degree of freedom for the energy in the blast wave, lowering its polytropic index. The radiation lowers the temperature of the gas in the blast front making it cooler and more compressible. This makes the blast front thinner for the same pressure drive and more susceptible to instabilities.

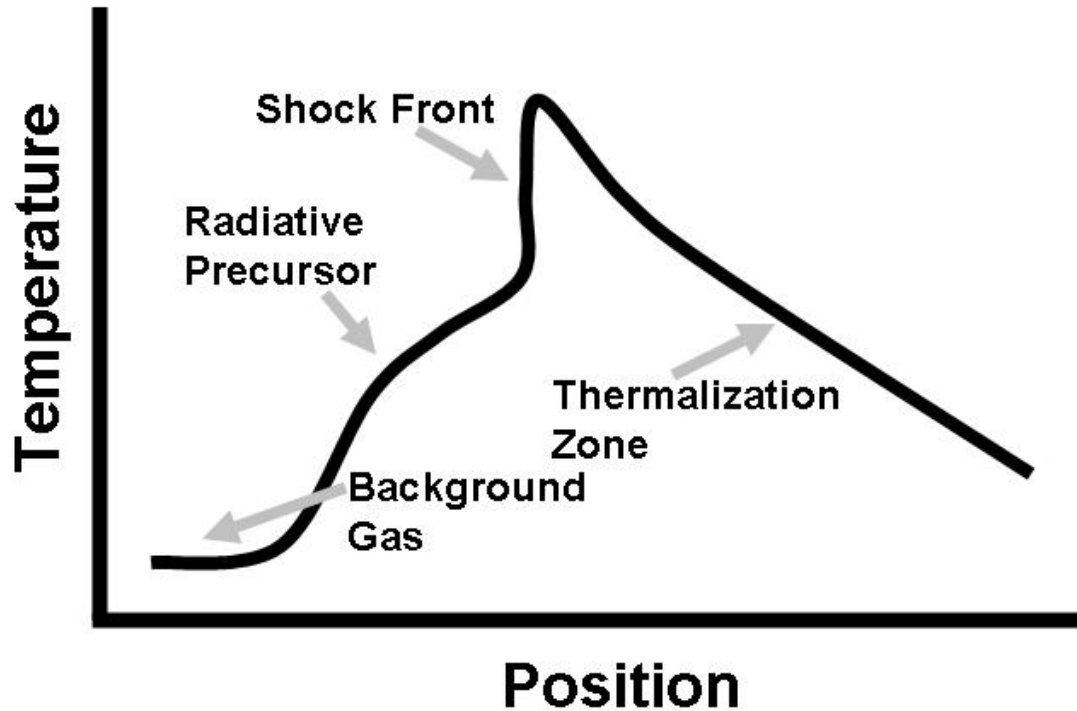


Figure 6. Illustration of the temperature versus position in a radiative supernova remnant. Some of the radiation from the shock front is absorbed in the background gas, creating a warm region known as the radiative precursor. Behind the shock front, the gas thermalizes to its final state.

Large scale structure is seen in supernova remnants known to be in the radiative phase, such as the Cygnus Loop and the Vela SNR. An image of these SNRs is shown in Figure 7. It is believed that when these structured SNRs encounter clouds of gas, they create density clumps that can seed the process of star formation^{20, 21}. Vishniac et al. theorized that the structure was due to an overstability that arises in the radiative SNRs

due to the thinning of the shock front. Therefore they formulated the theory¹⁷⁻¹⁹ of the pressure driven thin shell overstability, now known as the Vishniac overstability.



Figure 7. Images of the Cygnus Loop (left) and Vela Supernova Remnant. These are the canonical examples of radiative supernova remnants. Each is the remains of a supernova from over 10,000 years ago. The large scale structure seen in the edge profile is believed to be caused by the Vishniac overstability.

3.2 Vishniac Overstability

Vishniac and Ryu used perturbation analysis to develop a comprehensive theory¹⁷⁻¹⁹ for the hydrodynamic evolution of perturbations on the surface of a blast wave. The general idea behind the Vishniac overstability is illustrated in Figure 8. The blast wave is bounded on one side by ram pressure arising from expansion into an external medium and on the other by the thermal pressure of hot gas inside the blast wave. If there is any ripple of perturbation on the blast wave surface these two pressures can become misaligned. This causes mass to flow from the peaks of the perturbation to the troughs, increasing the relative momentum of the troughs. As the blast wave expands it sweeps up

additional matter and slows. This additional matter will comprise a smaller percentage of the mass of the troughs than the peaks, thus causing the troughs to slow less. Eventually the troughs of the perturbation pass the peaks and the process reverses, creating an oscillation in the blast wave surface. If the blast wave front is thin enough the oscillation can grow with time.

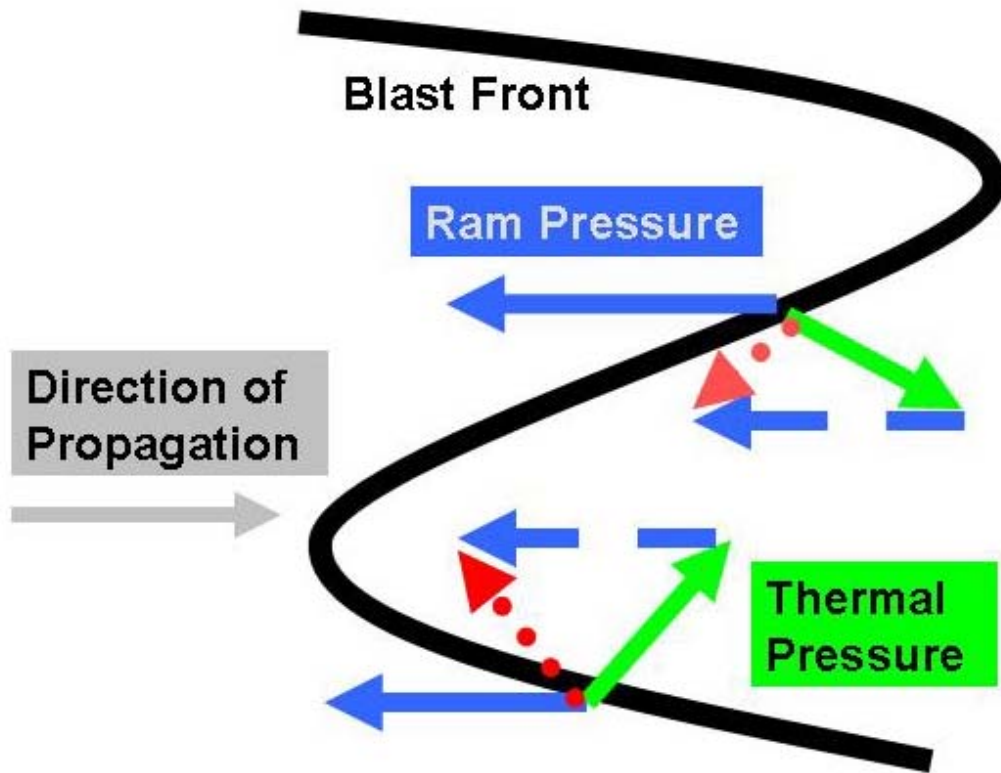


Figure 8. Illustration of the forces acting on a blast wave subject to the Vishniac Overstability. The black curve represents the blast front. The green and blue arrows represent the thermal and ram pressures respectively. The solid blue arrows show where the ram pressure acts and the dashed blue arrows are copies to aid in determining the net effect of the added pressures. The red curve represents the sum of the ram and thermal pressures and the net force on the gas in the blast wave. Note gas is pushed from the peaks of the ripple to its troughs.

To study the evolution of perturbations on the surface of a blast wave, Vishniac and Ryu assumed an adiabatic shock that followed the Taylor-Sedov solution for the

unperturbed blast wave. They then started with the conservation laws for such a blast wave. These are:

The continuity equation:

$$\frac{\partial \rho}{\partial t} + \vec{\nabla} \bullet (\rho \vec{v}) = 0 \quad (3.2.1)$$

Conservation of momentum:

$$\rho \frac{\partial \vec{v}}{\partial t} + \rho (\vec{v} \bullet \vec{\nabla}) \vec{v} + \vec{\nabla} p = 0 \quad (3.2.2)$$

and conservation of energy:

$$\frac{\partial p}{\partial t} + \vec{v} \bullet \vec{\nabla} p + \gamma p \vec{\nabla} \bullet \vec{v} = 0 \quad (3.2.3)$$

In these equations p is the pressure of the gas, v is the gas velocity, t is time, ρ is the density of the gas and γ is its adiabatic index. In place of the energy equation, conservation of entropy can be used:

$$\left(\frac{\partial}{\partial t} + \vec{v} \bullet \vec{\nabla} \right) \log \frac{p}{\rho^\gamma} = 0 \quad (3.2.4)$$

Next, Ryu and Vishniac defined the perturbation variables as the difference between the total value of a variable and the value associated with the unperturbed blast wave:

$$\delta \vec{v}(r, \theta, \phi, t) \equiv \vec{v}(r, \theta, \phi, t) - v_0(r, t) \hat{r} \quad (3.2.5)$$

$$\delta \rho(r, \theta, \phi, t) \equiv \rho(r, \theta, \phi, t) - \rho_0(r, t) \quad (3.2.6)$$

$$\delta p(r, \theta, \phi, t) \equiv p(r, \theta, \phi, t) - p_0(r, t) \quad (3.2.7)$$

where quantities with a 0 subscript refer to the unperturbed blast wave and r , θ , and ϕ are the normal spherical coordinates. The above equations are then inserted into the conservation equations, (3.2.1), (3.2.2), and (3.2.4), which are then linearized to 1st order in the perturbations variables to give

$$\frac{\partial \delta \rho}{\partial t} + \frac{1}{r^2} \frac{\partial (r^2 v_0 \delta \rho)}{\partial r} + \nabla \bullet (\rho_0 \delta v) = 0 \quad (3.2.8)$$

$$\frac{\partial \delta \vec{v}}{\partial t} + v_0 \frac{\partial \delta \vec{v}}{\partial r} + \frac{\partial v_0}{\partial r} \delta v_r \hat{r} + \frac{v_0}{r} \delta \vec{v}_t = \frac{-1}{\rho_0} \vec{\nabla} \delta p + \frac{\delta \rho}{\rho_0^2} \frac{\partial p_0}{\partial r} \hat{r} \quad (3.2.9)$$

and

$$\left(\frac{\partial}{\partial t} + v_0 \frac{\partial}{\partial r} \right) \left(\frac{\delta p}{p_0} - \gamma \frac{\delta \rho}{\rho_0} \right) + \delta v_r \frac{\partial}{\partial r} \log \frac{p_0}{\rho_0^\gamma} = 0 \quad (3.2.10)$$

In the above equation the radial and transverse components of the fluid velocity, v_r and v_t respectively, have been separated. Next the perturbation variables are normalized to the value of the unperturbed variables at the shock front according to:

$$\delta \vec{v} \equiv \frac{\delta \vec{v}}{v_2} \quad (3.2.11)$$

$$\delta \tilde{\rho} \equiv \frac{\delta \rho}{\rho_2} \quad (3.2.12)$$

$$\delta \tilde{p} \equiv \frac{\delta p}{p_2} \quad (3.2.13)$$

and the radial coordinate according to

$$\tilde{r} = \frac{r}{r_2} \quad (3.2.14)$$

For these equations the subscript 2 denotes the value of the quantity for the unperturbed blast wave at the shock front. The unperturbed variables can be similarly normalized to their values at the shock front. Ryu and Vishniac then expand the perturbations into spherical harmonics (Y_{lm}). This allows the time component of the evolution of a perturbation to be separated from its spatial behavior. The various wavelength components (specific l and m values) of the normalized perturbation variables become:

$$\delta \vec{v} = \delta \vec{v}_r(\tilde{r}) Y_{lm}(\theta, \phi) t^s \hat{r} + \delta \vec{v}_t(\tilde{r}) \tilde{\nabla}_t Y_{lm}(\theta, \phi) t^s \quad (3.2.15)$$

$$\delta \tilde{\rho} = \delta \tilde{\rho}(\tilde{r}) Y_{lm}(\theta, \phi) t^s \quad (3.2.16)$$

$$\delta \tilde{p} = \delta \tilde{p}(\tilde{r}) Y_{lm}(\theta, \phi) t^s \quad (3.2.17)$$

There is an assumed l and m subscript on the perturbation variables in the above equations that is not written as we choose to look at a specific component as representative of the whole. The operator ∇_t is the transverse gradient and is defined as:

$$\tilde{\nabla}_t \equiv \frac{1}{\tilde{r}} \frac{\partial}{\partial \theta} \hat{\theta} + \frac{1}{\tilde{r} \sin \theta} \frac{\partial}{\partial \phi} \hat{\phi}$$

Using the Taylor-Sedov solution discussed in chapter 2 for blast wave evolution the time derivatives of the normalized unperturbed variables can be written as:

$$\frac{\partial \tilde{v}}{\partial t} = -\frac{2}{5} \frac{\tilde{r}}{t} \frac{\partial \tilde{v}}{\partial \tilde{r}} \quad (3.2.18)$$

$$\frac{\partial \tilde{\rho}}{\partial t} = -\frac{2}{5} \frac{\tilde{r}}{t} \frac{\partial \tilde{\rho}}{\partial \tilde{r}} \quad (3.2.19)$$

$$\frac{\partial \tilde{p}}{\partial t} = -\frac{2}{5} \frac{\tilde{r}}{t} \frac{\partial \tilde{p}}{\partial \tilde{r}} \quad (3.2.20)$$

Noting that the radial component of the perturbation variables will behave like the unperturbed variables, we can take the time derivatives of (3.2.15)-(3.2.17):

$$\frac{\partial \delta \tilde{\vec{v}}}{\partial t} = -\frac{2}{5} \frac{\tilde{r}}{t} \frac{\partial \delta \tilde{\vec{v}}}{\partial \tilde{r}} + \frac{s}{t} \delta \tilde{\vec{v}} \quad (3.2.21)$$

$$\frac{\partial \delta \tilde{\rho}}{\partial t} = -\frac{2}{5} \frac{\tilde{r}}{t} \frac{\partial \delta \tilde{\rho}}{\partial \tilde{r}} + \frac{s}{t} \delta \tilde{\rho} \quad (3.2.22)$$

$$\frac{\partial \delta \tilde{p}}{\partial t} = -\frac{2}{5} \frac{\tilde{r}}{t} \frac{\partial \delta \tilde{p}}{\partial \tilde{r}} + \frac{s}{t} \delta \tilde{p} \quad (3.2.23)$$

Here s is the temporal exponent from equations (3.2.15)-(3.2.17). Using these equations, (3.2.8)-(3.2.10) become:

$$\begin{aligned} & \frac{-2}{5} \frac{r}{t} \frac{\partial \delta \rho}{\partial r} + \frac{s}{t} \delta \rho + \frac{1}{r^2} \left[2rv_0 \delta \rho + v_0 r^2 \frac{\partial \delta \rho}{\partial r} + r^2 \delta \rho \frac{\partial v_0}{\partial r} \right] \\ & + \rho_0 (\nabla \cdot \delta v) + \delta v (\nabla \cdot \rho_0) = 0 \end{aligned} \quad (3.2.24)$$

$$\frac{-2r}{5t} \frac{\partial \delta v_r}{\partial r} + \frac{s}{t} \delta v_r + v_0 \frac{\partial \delta v_r}{\partial r} + \frac{\partial v_0}{\partial r} \delta v_r + \frac{1}{\rho_0} \frac{\partial \delta p}{\partial r} - \frac{\delta \rho}{\rho_0^2} \frac{\partial p_0}{\partial r} = 0 \quad (3.2.25)$$

$$\frac{-2r}{5t} \frac{\partial \delta v_t}{\partial r} + \frac{s}{t} \delta v_t + v \frac{\partial \delta v_t}{\partial r} + \frac{v_0}{r} \delta v_t + \frac{1}{\rho_0} \nabla_t \delta p = 0 \quad (3.2.26)$$

$$\begin{aligned} & \frac{1}{\rho_0} \frac{\partial \delta p}{\partial t} - \frac{\delta p}{\rho_0^2} \frac{\partial \rho_0}{\partial t} + \frac{v_0}{p_0} \frac{\partial \delta p}{\partial r} - \frac{v_0 \delta p}{p_0^2} \frac{\partial p_0}{\partial r} + \frac{\gamma}{\rho_0} \frac{\partial \delta \rho}{\partial t} - \frac{\gamma \delta \rho}{\rho_0^2} \frac{\partial \rho_0}{\partial t} \\ & + \frac{\gamma v_0}{\rho_0} \frac{\partial \delta \rho}{\partial r} - \frac{v_0 \gamma \delta \rho}{\rho_0^2} \frac{\partial \rho_0}{\partial r} + \delta v_r \frac{\rho_0^\gamma}{p_0} \left[\frac{1}{\rho_0^\gamma} \frac{\partial p_0}{\partial r} - \frac{\gamma p_0}{\rho_0^{\gamma+1}} \frac{\partial \rho_0}{\partial r} \right] \end{aligned} \quad (3.2.27)$$

Here (3.2.25) and (3.2.26) are the result of separately solving (3.2.9) in the radial and transverse directions. Combining like terms and using (3.2.18)-(3.2.20) we can further modify these equations to:

$$\frac{\partial \delta \rho}{\partial r} \left[\frac{-2r}{5t} + v_0 \right] + \delta \rho \left[\frac{s}{t} + \frac{\partial v_0}{\partial r} + \frac{2v_0}{r} \right] + \rho_0 (\nabla \cdot \delta v) + \delta v (\nabla \cdot \rho_0) = 0 \quad (3.2.28)$$

$$\frac{\partial \delta v_r}{\partial r} \left[v_0 - \frac{2r}{5t} \right] + \delta v_r \left[\frac{s}{t} + \frac{\partial v_0}{\partial r} \right] + \frac{1}{\rho_0} \frac{\partial \delta p}{\partial r} - \frac{\delta \rho}{\rho_0^2} \frac{\partial p_0}{\partial r} \quad (3.2.29)$$

$$\frac{\partial \delta v_t}{\partial r} \left[v_0 - \frac{2r}{5t} \right] + \delta v_t \left[\frac{v_0}{r} + \frac{s}{t} \right] + \frac{1}{\rho_0} \nabla_t \delta p \quad (3.2.30)$$

$$\begin{aligned} & \frac{\partial \delta p}{\partial r} \left[\frac{v_0}{p_0} - \frac{2r}{5p_0 t} \right] + \delta p \left[\frac{s}{p_0 t} + \frac{2r}{5p_0^2 t} \frac{\partial p_0}{\partial r} - \frac{v_0}{p_0^2} \frac{\partial p_0}{\partial r} \right] + \frac{\partial \delta \rho}{\partial r} \left[\frac{\gamma v_0}{\rho_0} - \frac{2r\gamma}{5t\rho_0} \right] \\ & + \delta \rho \left[\frac{\gamma s}{\rho_0 t} + \frac{\gamma}{\rho_0^2} \frac{\partial \rho_0}{\partial r} \left\{ \frac{2r}{5t} - v_0 \right\} \right] + \delta v_r \left[\frac{1}{p_0} \frac{\partial p_0}{\partial r} - \frac{\gamma}{\rho_0} \frac{\partial \rho_0}{\partial r} \right] \end{aligned} \quad (3.2.31)$$

Finally, we can change to the normalized variables and make some final manipulations to get to the form of the equations desired:

$$\tilde{\rho} \frac{d\delta\tilde{v}_r}{d\tilde{r}} + \left(-\frac{\gamma+1}{2}\tilde{r}+\tilde{v}\right) \frac{d\delta\tilde{\rho}}{d\tilde{r}} + \left(2\frac{\tilde{\rho}}{\tilde{r}} + \frac{d\tilde{\rho}}{d\tilde{r}}\right) \delta\tilde{v}_r + \left[\frac{5(\gamma+1)}{4}s + 2\frac{\tilde{v}}{\tilde{r}} + \frac{d\tilde{v}}{d\tilde{r}}\right] \delta\tilde{\rho} - l(l+1) \frac{\tilde{\rho}}{\tilde{r}} \delta\tilde{v}_t = 0 \quad (3.2.32)$$

$$\left(-\frac{\gamma+1}{2}\tilde{r}+\tilde{v}\right) \tilde{\rho} \frac{d\delta\tilde{v}_r}{d\tilde{r}} + \frac{\gamma-1}{2} \frac{d\delta\tilde{p}}{d\tilde{r}} + \left[\frac{\gamma+1}{4}(5s-3) + \frac{d\tilde{v}}{d\tilde{r}}\right] \tilde{\rho} \delta\tilde{v}_r - \frac{\gamma-1}{2} \frac{1}{\tilde{\rho}} \frac{d\tilde{p}}{d\tilde{r}} \delta\tilde{\rho} = 0 \quad (3.2.33)$$

$$\left(-\frac{\gamma+1}{2}\tilde{r}+\tilde{v}\right) \tilde{\rho} \frac{d\delta\tilde{v}_t}{d\tilde{r}} + \frac{\gamma-1}{2} \frac{1}{\tilde{r}} \delta\tilde{p} + \left[\frac{\gamma+1}{4}(5s-3) + \frac{\tilde{v}}{\tilde{r}}\right] \tilde{\rho} \delta\tilde{v}_t = 0 \quad (3.2.34)$$

$$\begin{aligned} & \left(-\frac{\gamma+1}{2}\tilde{r}+\tilde{v}\right) \frac{d\delta\tilde{\rho}}{d\tilde{r}} + \frac{\tilde{\rho}}{\tilde{p}} \left(-\frac{\gamma+1}{2}\tilde{r}+\tilde{v}\right) \frac{d\delta\tilde{p}}{d\tilde{r}} + \left(-\gamma \frac{1}{\tilde{\rho}} \frac{d\tilde{\rho}}{d\tilde{r}} + \frac{1}{\tilde{p}} \frac{d\tilde{p}}{d\tilde{r}}\right) \tilde{\rho} \delta\tilde{v}_r \\ & -\gamma \left[\frac{5(\gamma+1)}{4}s - \left(-\frac{\gamma+1}{2}\tilde{r}+\tilde{v}\right) \frac{1}{\tilde{\rho}} \frac{d\tilde{\rho}}{d\tilde{r}}\right] \delta\tilde{\rho} + \frac{\tilde{\rho}}{\tilde{p}} \left[\frac{5(\gamma+1)}{4}s - \left(-\frac{\gamma+1}{2}\tilde{r}+\tilde{v}\right) \frac{1}{\tilde{p}} \frac{d\tilde{p}}{d\tilde{r}}\right] \delta\tilde{p} = 0 \end{aligned} \quad (3.2.35)$$

These equations, when combined with proper boundary conditions can be solved numerically to give values for s , the growth rate of the perturbations. The growth rate will vary as a function of γ and ℓ , the polytropic index of the shocked gas and the mode number of the perturbations respectively. A sample of some of the curves for the real part of s as a function of ℓ for different polytropic indices is shown in Figure 9. The imaginary part of s determines the rate at which the perturbations oscillate. This portion tends to increase rapidly with increasing mode number, meaning higher mode number perturbations will oscillate more rapidly. Ryu and Vishniac also developed an

approximate analytical solution for the evolution of perturbations on blast waves¹⁸, but we have used the exact numerical solutions for comparison to experiment.

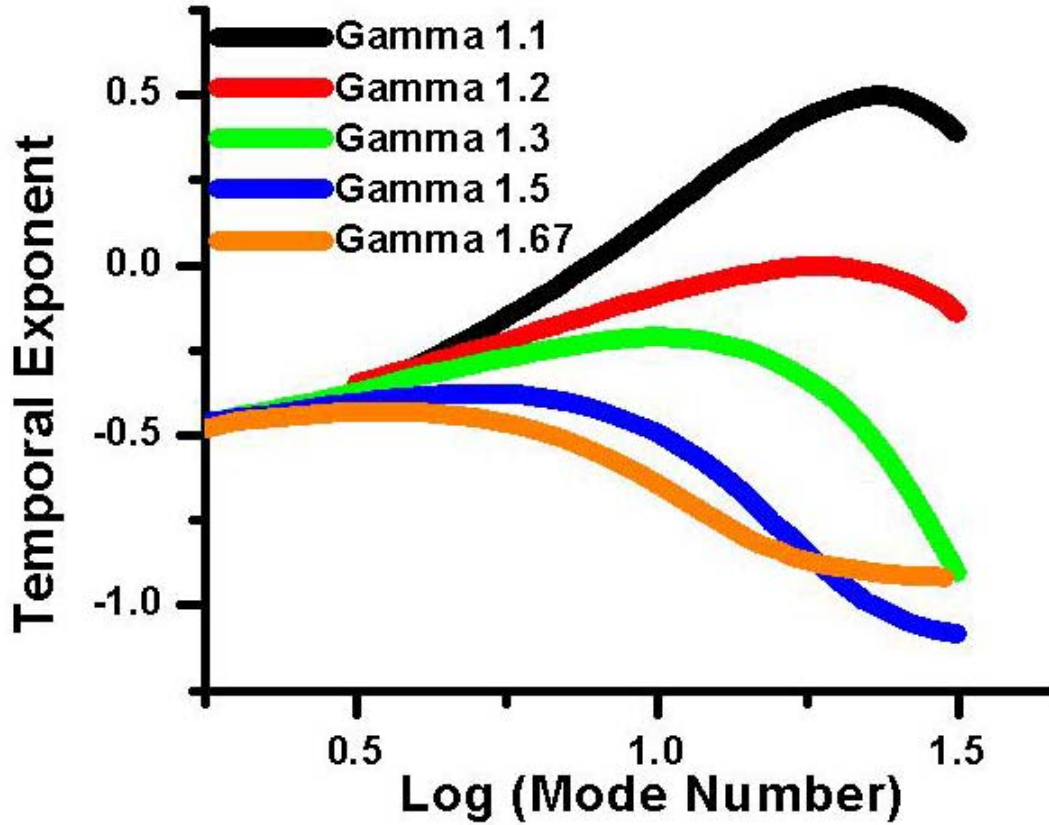


Figure 9. Theoretical predictions of Ryu and Vishniac for the evolution of perturbations on high Mach number blast waves. Shows the temporal exponent versus the log of the mode number of the perturbation for a number of different polytropic indices (gammas).

For any given value of the wave number a perturbation grows as a power law in time, $\delta \propto t^s$. They find that for a gas with an effective adiabatic index > 1.2 , perturbations will decay for all wave numbers. For a gas with an effective adiabatic index ≈ 1.2 , there will marginal stability of the blast wave at an approximate wave number of 20. For gasses with an adiabatic index < 1.2 there will be a range of wavelengths for which perturbations will grow. For all adiabatic indices, the growth rate increases slowly

as a function of wave number until the wavelength approaches the thickness of the blast front. At this point, the growth rate rapidly falls off with increasing wave number. Because the blast wave front becomes thinner as the adiabatic index approaches 1, the fall off point and thus the maximal growth rate location moves to higher wave number as the adiabatic index becomes smaller.

3.3 Hydrodynamic Scaling for Blast Waves

Ryutov et al.¹¹, in addition to providing an estimate for when a SNR enters a radiative phase as was discussed earlier in this chapter, examined the conditions for hydrodynamic similarity between two systems. There are several assumptions that need to be made to derive such a scaling. The first is that the system behaves as an ideal compressible hydrodynamic fluid. This means that there is zero viscosity and heat conductivity. In addition, for the specific case of scaling supernova remnants, Ryutov et al.¹¹ assumed a polytropic gas, which provided them with the type of equation of state discussed in chapter 2 (specifically equation (2.2.9)). They then examine the “Euler equations”: conservation of mass (2.1.1) and momentum (2.1.2) equations for the gas described earlier and a conservation of energy equation using the polytropic gas equation of state. These three equations are given by:

$$\frac{\partial \rho}{\partial t} + \vec{\nabla} \bullet (\rho \vec{v}) = 0 \quad (3.3.1)$$

$$\frac{\partial \vec{v}}{\partial t} + (\vec{v} \bullet \vec{\nabla}) \vec{v} = -\frac{1}{\rho} \vec{\nabla} p \quad (3.3.2)$$

$$\frac{\partial p}{\partial t} - \gamma \frac{p}{\rho} \frac{\partial \rho}{\partial t} + \vec{v} \bullet \vec{\nabla} p - \gamma \frac{p}{\rho} \vec{v} \bullet \vec{\nabla} \rho = 0 \quad (3.3.3)$$

Ryutov et al. then noted that these equations are invariant under the following transformation:

$$\begin{aligned} r &= ar_1; \quad \rho = b\rho_1; \quad p = cp_1; \\ t &= a\sqrt{\frac{b}{c}}t_1; \quad v = \sqrt{\frac{c}{b}}v_1; \end{aligned} \quad (3.3.4)$$

Using these relations one can say that two systems will behave similarly if their “Euler numbers” are the same, where the Euler numbers are defined according to:

$$v_1 \sqrt{\frac{\rho_1}{p_1}} = v_2 \sqrt{\frac{\rho_2}{p_2}} \quad (3.3.5)$$

The subscripts 1 and 2 denote mean properties of the two different systems. One can similarly use the relations (3.3.4) along with the scale heights of the two systems h_1 and h_2 to compare the timescales at which the two systems evolve:

$$\tau_1 = \tau_2 \frac{h_1}{h_2} \sqrt{\frac{p_2 / \rho_2}{p_1 / \rho_1}} \quad (3.3.6)$$

Because of the assumption of no heat conduction, this scaling system does not strictly apply to radiating blast waves, but they still provide a useful tool in comparing our laboratory experiments to SNRs. We can take the astrophysical parameters from the work of Ryutov et al. and the laboratory conditions from our experiments and compare the two systems. The laboratory values will be taken from a combination of measured and simulated values for blast waves in nitrogen gas produced by a 1000 J laser pulse.

Quantity	SNR Value	Lab Value
h (cm)	$3.0 \cdot 10^{16}$	1
v (cm/s)	$9.5 \cdot 10^8$	$4 \cdot 10^6$
p (dyn/cm ²)	$1 \cdot 10^{-5}$	$2 \cdot 10^7$
ρ (g/cc)	$1 \cdot 10^{-22}$	$1.5 \cdot 10^{-4}$

Plugging these numbers into (3.3.5) yields Euler numbers of 3 for the SNR and 10 for the lab condition. Therefore, the Euler number is similar for the two systems. We get from (3.3.6) that there is a conversion factor of $3 \cdot 10^{-14}$ for transforming time scales between the SNR and the lab frame. This means 1,000 years ($3 \cdot 10^{10}$ s) corresponds roughly to 1 ms in the lab frame, which is longer than most of the experiments. It should be noted that the astrophysical parameters were taken for a young SNR (at the 13 yr mark) and for the radiative SNRs (usually 10,000 years to 15,000 years old) the parameters will vary somewhat with in general larger scales and smaller pressures both of which will tend to lower the conversion factor and bring the relevant time scales more in line with the laboratory experiments.

4. Blast Wave Simulations

4.1 Astrophysical Simulations

Over the years a number of simulations have been performed to look at various aspects of the theory of Vishniac et al. Simulations of both super nova remnants (SNRs) and laboratory experiments have been done. Mac Low and Norman²³ performed simulations using the two dimensional numerical hydrodynamics code ZEUS-2D to confirm the growth rates predicted by Vishniac and Ryu¹⁹ for low polytropic index gasses. They modeled self-similar, adiabatic, blast waves with an adiabatic index of 1.1 and perturbed them with a theoretical eigenmode of the overstability. The resulting perturbation evolution followed the theoretical growth rates predicted by Vishniac et al. while the perturbation was in the low amplitude limit. However, perturbation growth saturated at higher amplitude due to the formation of transverse shocks created by gas colliding supersonically in the valleys of the perturbation.

Blondin et al.²² performed a series of one dimensional and two dimensional simulations of expanding supernova remnants using the piecewise parabolic numerical hydrodynamics code VH-1. Results from the one dimensional simulations show the SNR trajectory undergoing a massive unstable change as the SNR enters the radiative regime and the blast shell collapses. After this period the blast wave trajectory slows down and approaches $t^{0.33}$. This is higher than either the pressure driven snowplow or momentum conserving snowplow regimes expected when a SNR goes fully radiative. The authors

suggest that the reason for the difference with theory is the presence of a reverse shock traveling through the interior of the SNR increasing the thermal pressure pushing the shock front. However, they caution this value may be affected by the assumption of an infinitely thin shock transition in the simulations. The two dimensional simulations performed provided several results. The first result was a confirmation that the density of the interstellar medium (ISM) into which a SNR travels has a determining impact on whether or not an overstability can arise and the period over which it grows. Blondin et al. found that the impact of overstabilities was proportional to the density of the ISM in the simulations, and that there was no evidence of the overstability if the ISM was too disperse. In addition, they found it necessary to provide a seed for the perturbation in the background gas in order to see any effect from the Vishniac overstability. Seeding with a high growth eigenmode of the approximate solution of Vishniac and Ryu¹⁸ a density perturbation as small as 0.1% began to show effects on the blast wave's radial evolution. For a 1% density perturbation the oscillations on the order of 10% of the radius of the SNR were observed, suggesting the Vishniac overstability could indeed have a significant impact on the morphology of a SNR.

4.2 Simulations of Laboratory Experiments

In addition to simulations of astrophysical situations, laser-driven blast wave experiments have also been simulated. Laming and Grun have written two papers^{33, 34} simulating previous experiments of Grun et al¹⁶. In these experiments blast waves were created by illuminating foils immersed in five Torr of background gas with 100 J-200 J

laser pulses. Blast waves traveling through both nitrogen and xenon gasses were simulated. Using detailed atomic models to account for ionization in the blast wave, Laming and Grun provide predictions for many properties of the simulated blast waves at a number of time steps up to 400 ns after the creation of the blast wave. At each time, they give predictions for the velocity of the shock front, the relative abundances of various ionization states of the gas, the temperature of the radiative precursor preceding the shock front, the Mach number of the shock front, the polytropic index of the gas in the front, the maximum growth rate of the Vishniac overstability, the mode number at which this maximum growth occurs, and the fractional energy loss due to radiation at the shock front (ϵ). The polytropic index is calculated from the density jump across the shock in the simulations and the jump conditions listed in section 2.2, and the growth rate and mode number of the overstability are calculated from the approximate analytical formulas of Ryu and Vishniac¹⁸. The results for the polytropic index and growth rates from the two papers differ somewhat while other parameters mostly remain the same. In the earlier paper, blast waves in nitrogen are stable at all but the earliest simulated time (40 ns) and the authors speculate that at this time the blast wave is still in the ejecta dominated phase. In the later paper blast waves in nitrogen have the potential to be overstable for 150 ns before entering a stable regime. In general the polytropic index and maximum growth rates differ fairly significantly for nitrogen between the two papers. Blast waves traveling through xenon show a much smaller discrepancy. In both papers, these blast waves are overstable for approximately 200 ns, or until they drop below 25 km/s. In the earlier paper the polytropic index then quickly increases to a more stable value. In the later paper the behavior is the same for the first 200 ns but the late time

behavior in the later paper maintains a lower polytropic index for a longer period of time. Generalizing the xenon results, Laming and Grun suggest there is an approximate cutoff velocity of 25 km/s for the overstability to occur in blast waves traveling through 5 Torr of xenon gas. They also suggest that at higher gas densities there will be depopulation of excited energy levels by electron collisions that will reduce the radiative cooling rate for blast waves of similar velocity. This means that the cutoff velocity for the overstability will likely rise with the gas pressure. They also attribute the depopulation of excited energy levels by electron collisions as part of the reason for the reduced chance for overstability in nitrogen as opposed to xenon.

The experiments simulated by Laming and Grun differ from our experiments where the blast waves are produced by ~ 1 kJ on pin targets. However, the spatial scales and velocities observed in their experiments were very comparable to those we observe (using the different target geometry) making their theoretical predictions particularly relevant. Since the temporal evolution of their simulated blast waves differ significantly from the ones seen in our experiments, we chose to compare blast waves traveling with similar velocities. For our experimental blast waves at 100 ns (approximately the time the blast wave encounters the wire array in our experiments), our blast wave is traveling at ~ 35 km/s. Laming and Grun³³ predicted an effective polytropic index of 1.23 for blast waves with this velocity which they later revised to 1.1³⁴ in the second paper.

In support of our specific experiments we have performed simulations using the one dimensional Lagrangian radiation hydrodynamics code HYADES³⁵. This code employs a tabular equation of state (EOS) and diffusive radiation transport with user defined photon groups. To simulate our problem we simulated a 500J or 1 kJ, 1 ns, 527

nm wavelength laser pulse incident on a 0.25 micron radius plastic target immersed in 10 Torr of nitrogen gas (1.6×10^{-5} grams per cubic centimeter). We employed the SESAME EOS number 5000 from Los Alamos National Laboratory as the EOS for nitrogen gas. All simulations were run in spherical geometry. Simulations were run for approximately 1 microsecond in order to capture the dynamics of the blast wave during the period that perturbations evolved (~ 150 ns - 700 ns). Simulations took between 1-20 hours to run depending on a number of factors including the energy of the laser pulse and the number of zones used.

The first attempt at simulations included all default parameters and no radiation as well as an aluminum target material. This resulted in a blast wave that was too strong and traveled too quickly. In addition, in an attempt to reduce numerical errors, the sizes of zones adjoining one another were kept to approximately the same size. Due to the large density difference between the solid aluminum and the low density nitrogen gas there was a mass mismatch between the last zone of the aluminum pin and the first zone of the nitrogen gas. This mismatch caused density oscillations in the gas. Matching the masses caused the same problem due to size mismatch. It was found that an intermediate zone size for the nitrogen that did not match either the size or mass well minimized the oscillations. Eventually, an equation of state was found for Teflon, which allowed us to change the target to this material and more closely match the experiment. This further reduced the mass mismatch and fully eliminated the oscillations. Other improvements discovered during these early simulations include parameters that can be changed to reduce the time for a simulation to run. Output from a simulation includes a .tmf file that lists how long each time step takes to run and the process that limits the size of the time

step. It was found that the courant time was the predominant limiting time factor. This is the time that it takes for the shock front to cross one material zone. This time step could be increased by changing the dtcurm parameter. This parameter is the multiplier for the courant time step and can be increased from the default value of 1 to 2 without causing problems. An additional error that was discovered during this period was associated with the energy of the laser pulse. Entries for the laser in Hyades are input in terms of laser intensity in units of Watts per square centimeter. Originally, we used the solid target as the point at which the intensity was to be calculated. In fact, the code assumes a one square centimeter area for the beam and intensities should be entered in terms of this value. Because of this the laser energy in some early simulations was one megaJoule instead of one kilaJoule.

The main parameters that were adjusted were the electron flux multiplier (flxlem) and electron conduction multiplier (condem). We changed these in order to match the simulated trajectory to that observed during experiments. These were modified extensively in early experiments but it was later discovered that they need to be kept to within a factor of a few of their default values in order to maintain a physically viable simulation. Within these boundaries, changing these parameters did not have much of an effect on the blast wave trajectory. The change that created the greatest change on the trajectory was inclusion of radiation. This provided a means for the blast wave to cool and slowed the blast wave down. However, the trajectory could not be matched well with a 1000 J laser pulse. Using a 500 J laser pulse resulted in a trajectory that much more closely matched the experiment.

The primary output examined was the density ratio across the shock front, in order to gain an estimate of the polytropic index using the jump conditions. The density profile of the shock during the period of measured perturbation evolution is seen in Figure 10 for a 1000J laser drive and in Figure 11 for a 500J laser drive. For the 1000J drive, prior to 300 ns, the blast wave decayed from a very large density ratio across the shock front, consistent with a polytropic index less than 1.2 and growth of the overstability. After 300 ns, the density ratio experienced quasi-stability and decayed slowly from a density ratio consistent with a polytropic index of 1.25 for approximately 500 ns. After approximately 800 ns total time, the density ratio began falling as the blast wave expanded and cooled. From these results, we took the approximate polytropic index of the nitrogen gas in our experiment to be 1.25 during the period from ~150 ns – 700 ns for purposes of comparison to experimental results. However, the value of 1.25 is in good agreement with the Laming and Grun result from their 1st paper. For the 500 J laser drive the blast wave seems to smoothly decay over the entire time range. Over the time period shown in Figure 11, the density ratio implies a polytropic index ranging from 1.1-1.55. The higher polytropic indices seen here corresponds more closely to the values implied by experiment that will be discussed later. There were some features in the simulation that indicated that these values may be somewhat in error. The most important of these is the lack of a significant radiative precursor in the simulation data, which is significantly different from the results of experiments. This precursor shows up clearly in the experimental data, and its absence in the simulation may artificially increase the density ratio and thus lower the polytropic index.

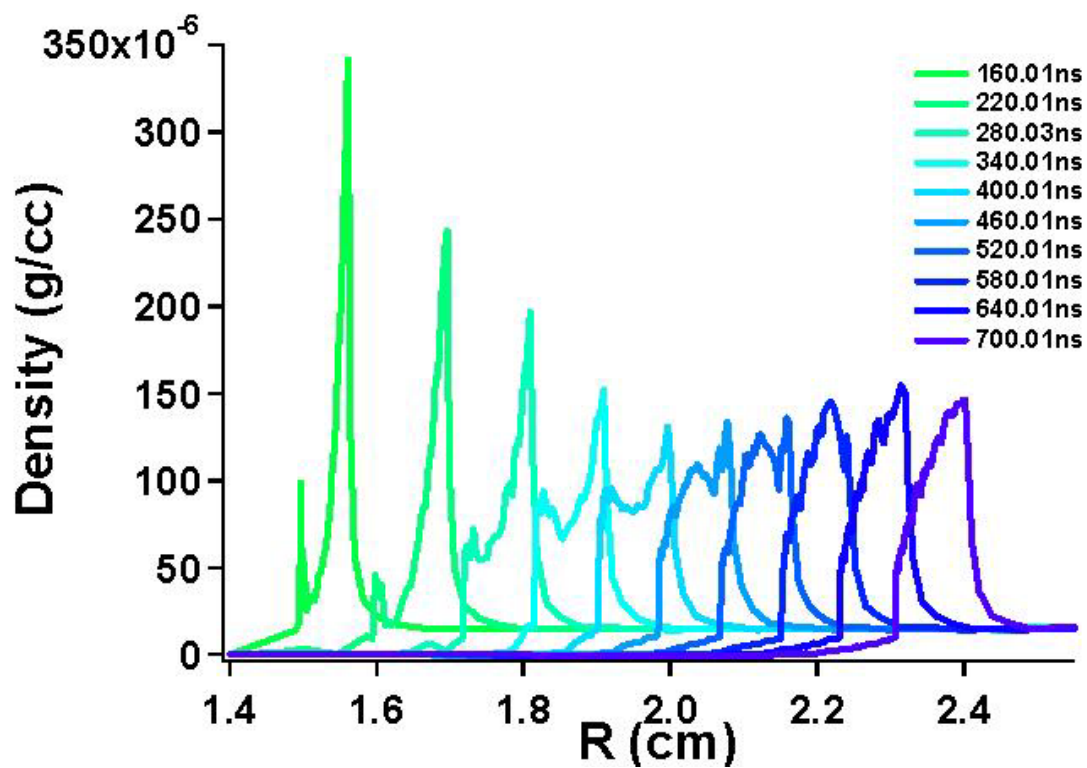


Figure 10. Simulation results from Hyades for spherical blast waves produced in 10 Torr (1.6×10^{-5} g/cc) of nitrogen gas. Density profiles versus position are seen for a number of different times. Times are relative to a 1000J laser pulse incident on a 0.25mm radius spherical plastic target.

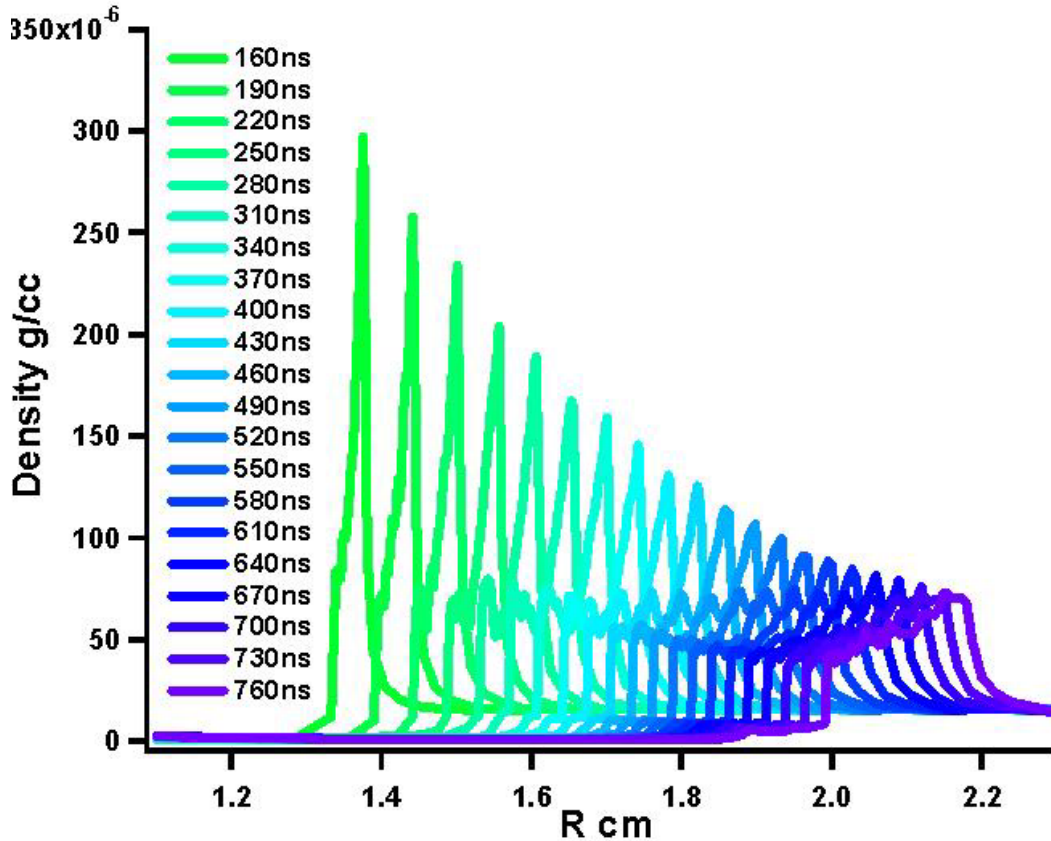


Figure 11. Results of Hyades simulation of blast wave traveling in 10 Torr (1.6×10^{-5} g/cc) of nitrogen gas. The blast wave was created by a 500J laser pulse incident on a 0.25mm radius plastic sphere. There is a strong decrease in the strength of the blast wave with time.

The reason the radiative precursor does not show up properly in the simulations is most likely related to how radiation is handled in the codes. If all possible radiative transitions in the hot gas were properly modeled and the action of each radiated photon tracked the computing time necessary to simulate any experiment would be prohibitively long even for the fastest computers. To circumvent this problem, radiation hydrodynamics codes average the properties of the gas at different photon energies and use a diffusion approximation to determine the action of the radiation. The size of the “photon groups” the radiation is broken into can be set by the user, allowing high precision around known strong transitions, but there is always some averaging. In

addition, instead of tracking the behavior of each individual photon, the mean action of photons is determined by the diffusion approximation that is based on an assumption of local radiative thermal equilibrium, which will not be the case for an optically thin blast wave that has non-local radiation transport. These approximations to radiation transport used in the hydrocodes to make computation times reasonable may be responsible for the discrepancy in the radiative precursor between experiment and theory.

5. Experimental Setup

A schematic of the primary experimental test bed used for the experiments described in chapter 7 is shown in Figure 12. For all of our experiments, a solid target was placed in a target chamber filled with less than an atmosphere of background gas. A drive laser illuminated one side of the solid target and created our blast waves. A second independent probe laser was fired at a controllable time later and was the basis of our diagnostics.

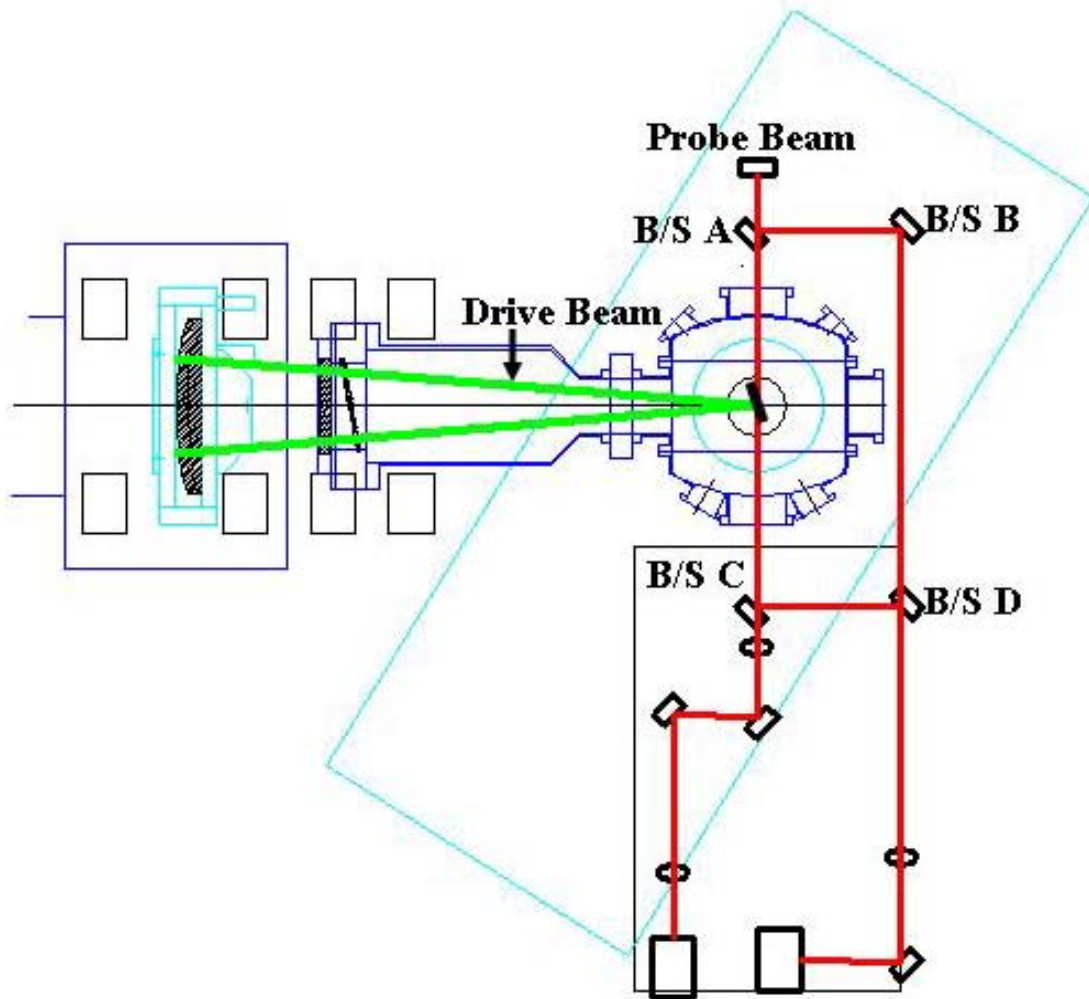


Figure 12. Layout of experimental setup for use with Z-Beamlet laser. Up to 1000 J level drive beam entered the experimental chamber from the left and illuminated a solid target. A probe beam used in both an interferometer and schlieren diagnostic starts at the top of the drawing. The four beamsplitters used in the diagnostics are labeled B/S.

5.1 Laser Systems

Our experiments were conducted at two different laser facilities. Early experiments at 10 J and 100 J drive energy were conducted on the Janus laser at Lawrence Livermore National Laboratory³⁶. This laser fired 1 ns pulses at 1054 nm wavelength every ten minutes at the 10 J level or every 30 minutes at the 100 J level.

The amplifiers in the Janus laser are made of doped glass which has poor thermal conductance. It is the cool down time for the glass that sets the shot repetition rate for this laser. The 10 J level was known as rod shots due to the fact only the rod amplifiers were used during these shots. The large glass slab amplifiers that provided the final amplification to the 100 J level have large volumes and so take over 20 minutes to cool after a shot, leading to the 30 minutes between system shots, as the 100 J shots are known. The drive laser was focused by a 1.5 m focal length lens to target chamber center. A separate few mJ, 532 nm wavelength laser provided the probe beam in these experiments. The probe pulse was 10 ns long, but the camera used in the diagnostics was electronically gated to 2 ns. A photodiode at the center of the target chamber was used to initially measure the relative timing between the two laser pulses to approximately 1 ns. The timing of the probe pulse relative to the drive laser could then be adjusted using a digital delay generator. In addition to the drive and probe lasers there was an alignment laser available. This was a low energy pulsed laser that emitted multi-ns pulses at 1054 nm wavelength with a 10 Hz repetition rate.

Experiments at the 500 J and 1000J levels were conducted on the Z-Beamlet laser at Sandia National Laboratories³⁷. Pulses from this laser can be adjusted from 600 ps to 2 ns in length. For our experiments 1 ns long pulses were employed. The final focusing lens for this laser had a focal length of 90 cm. On target, the laser light is at a 527 nm wavelength but during the amplification stages this laser operates at 1054 nm wavelength. A KDP crystal is used to convert the laser light to 527 nm after all the amplification has been done. A dichroic mirror prior to the target chamber is coated to reflect 527nm light and pass 1054 nm light. However, a small amount of 1054 nm light

is reflected and enters the experimental chamber. This light has a different focal spot than the 527 nm light and passes by the solid targets set up at the target chamber center. However, it can affect the gas in the chamber in the region of its laser cone, and this effect must be kept in mind when looking at these regions. The glass amplifiers on this laser are significantly larger than those on the Janus laser. Therefore, a three hour cool down period was required between shots on this laser in order to maintain a small focal spot, limiting experiments to three shots per day.

The probe laser used in conjunction with these experiments, known as the NLS laser, was capable of firing up to 10J, approximately 150 ps pulses at 1064 nm wavelength but was operated at a level that produced 80 mJ pulses that ranged from ~ 130 ps- 250 ps in duration. This was achieved by firing only two of the five NLS amplifiers and firing the second of these at less than full power. All of the amplifiers on the NLS laser are rod amplifiers and the two used for probing our experiment have the smallest radii of the five. Because of this, the limiting factor for the shot rate on NLS was charging of the capacitor banks that powered the flash lamps exciting the rod amplifiers. Charging took approximately three minutes. The output of the regenerative amplifier (regen) of this system was employed for alignment purposes. The regen operated at a 5 Hz repetition rate and put out laser pulses with a few mJ of energy, but otherwise identical to the other pulses from the system.

There was some variation in the pulse length of the NLS laser, from ~125 ps-300 ps. These pulse lengths were all considerably shorter than the 2 ns probe duration in the Janus experiments. In addition, blast waves were examined between 25 ns and 10 μ s after the drive laser hit the target, and the pulse durations measured were all short

compared to these times. Thus a small variation in the probe pulse time has no effect on the measurements. The relative timing between the drive and probe lasers was again measured using a photodiode and adjusted to ensure a less than 1 ns uncertainty in the relative timing.

The NLS laser is not relay imaged and so the beam quality can suffer, especially at higher energies. By keeping the probe laser energy at a minimum, the effects of propagating the beam were minimized. However, a significant amount of scattered light from the drive laser reaches the diagnostic cameras. Therefore the probe beam needs to be intense enough to be distinguished from the background noise. It was found that with a 70 mJ – 90 mJ level of energy the probe beam could be discerned from the background noise and adequate beam quality was maintained and so this level was used. The NLS laser is housed directly below the platform where the experimental area is located. Therefore the beam entered the area through a hole directly beneath the chamber, where it was deflected onto the table and periscoped up to the correct height. The point labeled “probe beam” in is the location of the periscope.

5.2 Gasses and Target Materials

The vacuum target vessels used in the experiments were evacuated to less than 100 milliTorr pressure and then filled with gas via a leak valve to the desired pressure. Due to the fact that a thermocouple pressure gauge is inaccurate when measuring the pressure of gasses like xenon and helium, a Baratron gauge was used to measure the pressure of gas in the chamber. The thermocouple pressure gauge is unsuitable for a

noble gas because the low dipole moment of these gasses causes the gauge to read low. In addition, for a heavy gas like xenon, the gas tends to stay inside the gauge head, causing the gauge to be inaccurate for a while even when measuring other gasses. The pressure of gas in the chamber varied with the experiment and for most shots was set by theoretical considerations.

The work of Ryutov et al. on supernova remnant discussed in chapter 3 describes the conditions under which a blast wave will become radiative. Experiments were designed to meet these criteria and the gas pressure in the chamber was set to match the expected temperature of the blast wave. For early 10 J and 100 J experiments, the gas pressure was 5 Torr the majority of the time. To ensure we were not missing the proper region of parameter space, an experiment was performed to examine the effect of varying the pressure on the blast wave evolution, specifically looking for enhanced growth of perturbations. There was no noticeable change in the perturbation evolution found. For the 500J and 1000J experiments the total gas pressure was maintained at 10 Torr. A variety of gases was used in the experiments including xenon, nitrogen, helium and mixtures of nitrogen and xenon in order to examine the effects of a change in the polytropic index of the background material. The polytropic index of a gas will vary with the amount of radiation emitted, which varies with the atomic number of the gas.

In order to launch a blast wave into a background gas, it is necessary to concentrate the laser energy in the midst of the gas. Since a low pressure gas absorbs laser light poorly a solid target is necessary to absorb the laser energy and launch the blast wave. However, a low mass target is desired in order to allow the majority of the energy to be coupled into the blast wave instead of being used to vaporize the target. The

downside of the solid target is that it can cause a deviation from sphericity in the resulting blast wave. If the target is not immediately vaporized by the laser pulse the resulting explosion will be partially slowed by the remainder of the target, this means that the energy of the part of the explosion will be greater in the direction towards the drive laser than away. In our experiments, we have found that this causes the length of the blast wave to be greater along the laser propagation direction than perpendicular to it.

At both laser facilities the solid targets could be manipulated in three dimensions by use of translation stages. This allowed the target to be placed precisely at the target chamber center. For Janus targets a CW laser coincident with the drive beam was employed to position the target. By moving the target so that all the laser light was blocked, it could accurately be placed at the focus of the drive laser. For Z-Beamlet targets a pair of cameras with a highly magnified view of the center of the target chamber were placed to aid in target alignment. The two cameras were placed at the outside of the target chamber approximately 60° offset from one another relative to target chamber center, on ports 30° above and below the port where the drive laser entered the chamber as is illustrated in Figure 13. The two fields of view intersected at target chamber center. A CW alignment beam coincident with the drive beam was also employed to aid in target alignment. The position of the target transverse to the drive laser could be adjusted on either camera, and the focal position was set when the vertical position of the alignment beam on the target was identical on both cameras. As is illustrated in Figure 13, if the target is in the wrong focal position the alignment beam will appear above the center of the image for one camera and below for the other. The camera systems were set up so

that the field of view of the camera images was only a few millimeters and the target could be positioned with a high degree of accuracy.

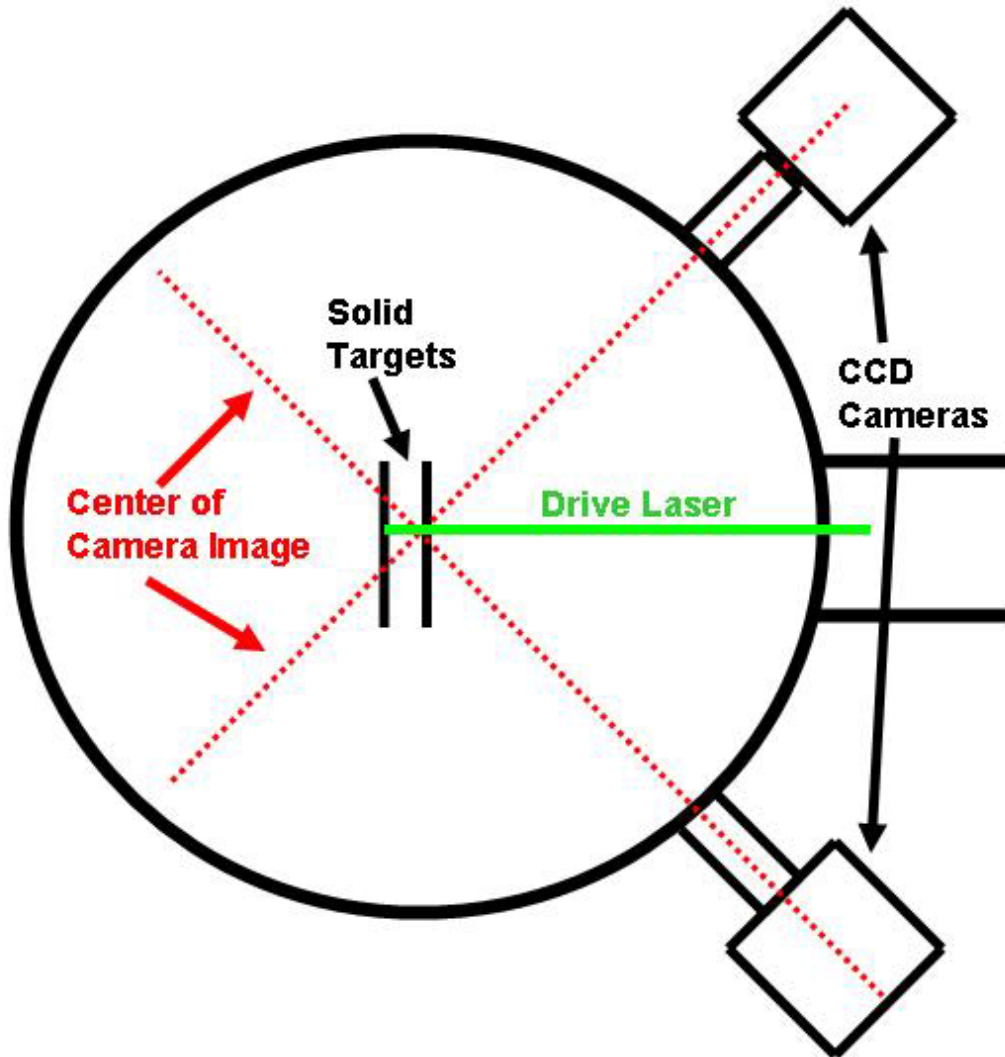


Figure 13. Illustration of the side view of the target chamber used for experiments on the Z-Beamlet laser. A CCD camera was placed on either side of the drive laser entry port. The fields of view of the two cameras intersected at target chamber center. Any misalignment of the solid target along the focal axis of the drive laser would cause images of an alignment laser coincident with the drive laser to appear at different positions on the two cameras.

Since the Janus laser could fire every 10 min – 30 min depending on the energy level, it was desirable to be able to fire multiple times without venting the target chamber in order to change targets. This made it necessary to have a target that could withstand

multiple laser pulses. Therefore, a stainless steel sewing needle that tapered from a 1 mm radius tip to a point was used as the target. This allowed multiple shots to be fired on the tip portion of the needle before reaching a portion of the target that was too thick to be entirely ablated, necessitating a change of targets. For later experiments on the Z-Beamlet laser, the laser could only be fired every 3 hours, eliminating the need for a multi-shot target. Therefore smaller lower mass wire targets were employed that were completely destroyed on every shot. The targets for the Z-Beamlet experiments were held in place by slip fitting them into a piece of coaxial cable that has had its center wire removed and an appropriate sized hole bored into the tip. The type of target was changed several times during the course of early experiments on this laser. Initially, a 0.25 mm radius copper wire was chosen. The radius was quickly increased to 0.5mm as images showed a significant amount of laser light passing by the target. While this was likely mostly unconverted light since this light has a different focal spot than the main drive energy and only a small fraction of the energy in the beam, it was significant enough to disturb the background gas and interfere with the experimental measurements. Eventually, the target material was changed to nylon. A plastic target offered two advantages over the copper target. The first was less radiation from the target. Some separate experiments carried out by collaborators on the Janus laser confirmed that radiation from the target material can affect the evolution of the blast wave somewhat and this is also suggested in our data. Using a plastic target made it easier to isolate and diagnose the effects of radiation from the shocked gas. In addition, explosion of copper targets created debris that impacted the windows of our chamber. When the probe beam

passed through these windows, the debris affected the beam and showed up in the diagnostics interfering with measurements.

5.3 Wire Arrays

For a number of experiments, we induced regular perturbations on the surface of blast waves. Initially, for a few shots on the Janus laser, a pin was placed in the path of blast waves in xenon for 100J level drive energies. However radiation from the blast wave created a blast wave off the pin that interfered with the main blast wave. In addition the evolution would be difficult to compare to theory because with only one pin in the blast wave path the modal content would be very large. This is due to the fact that the Fourier transform of a single pulse has a large number of frequency components. To minimize the modal content it was desirable to induce as many wavelengths of the perturbation as possible around the spherical blast wave. Therefore we fielded improved wire arrays for later experiments.

For experiments on the Z-Beamlet laser wire arrays with several wires were created. The arrays were designed so that the spacing of the wires on the arrays could be adjusted between shots to increase the available parameter space for experiments. During preliminary experiments the wire array employed was made of 1/16" thick aluminum and strung with tantalum wires. We tried to attach the wires by soldering them, but soldering does not work on aluminum. Eventually, we arc-welded the wires into place and this worked, but was time consuming and difficult. This array was placed at a 45° vertical angle above the target plane on the side of the target away from the drive laser. This

array met with limited success. The angle made it difficult to place the array precisely and since the wires were arc-welded they could not be modified or repaired between shots. In addition, the fundamental laser light that entered the chamber visibly affected the gas on the back side of the target in its focal cone, adding complication to the experiment. For later runs new arrays were constructed that worked much better.

Two different wire arrays were employed during our experiments. These arrays were placed above the target to avoid the effects of the fundamental light entering the chamber. The first array was constructed of 1/8" thick brass and had a square clear aperture approximately 3 cm on a side. Quarter-millimeter scale grooves were machined into the array at two millimeter intervals. Through these grooves were strung 30 gauge tin-copper wires. To string the wires, one long wire was wrapped around a screw in the array and then wrapped around the array through the appropriately spaced grooves. The wire was then held in place at each end with an aluminum bar and paper padding. The wire was clipped on the backside of the array so that only the portions of the wire necessary for the experiment remained. This array was much easier to restring than the preliminary model and could be modified between shots. An illustration of this array is shown in Figure 14. Figure 15 shows an image of this array in the target chamber. The wires were spaced 2, 4, or 6 mm apart in order to vary the mode number of the induced perturbation. A schematic for a second, cylindrical, array is shown in Figure 16. This array was designed to be half of a 1 cm diameter cylinder with flat extended sides for holding the array and was constructed of stainless steel so that it would maintain its shape. Grooves on this array were spaced every one millimeter and wires were spaced every 2, 3 or 4 mm. The wires used in this array and the process for stringing this array

was identical to that for the flat array except that the flat aluminum bar was replaced by a stainless steel insert that matched the shape of the array.

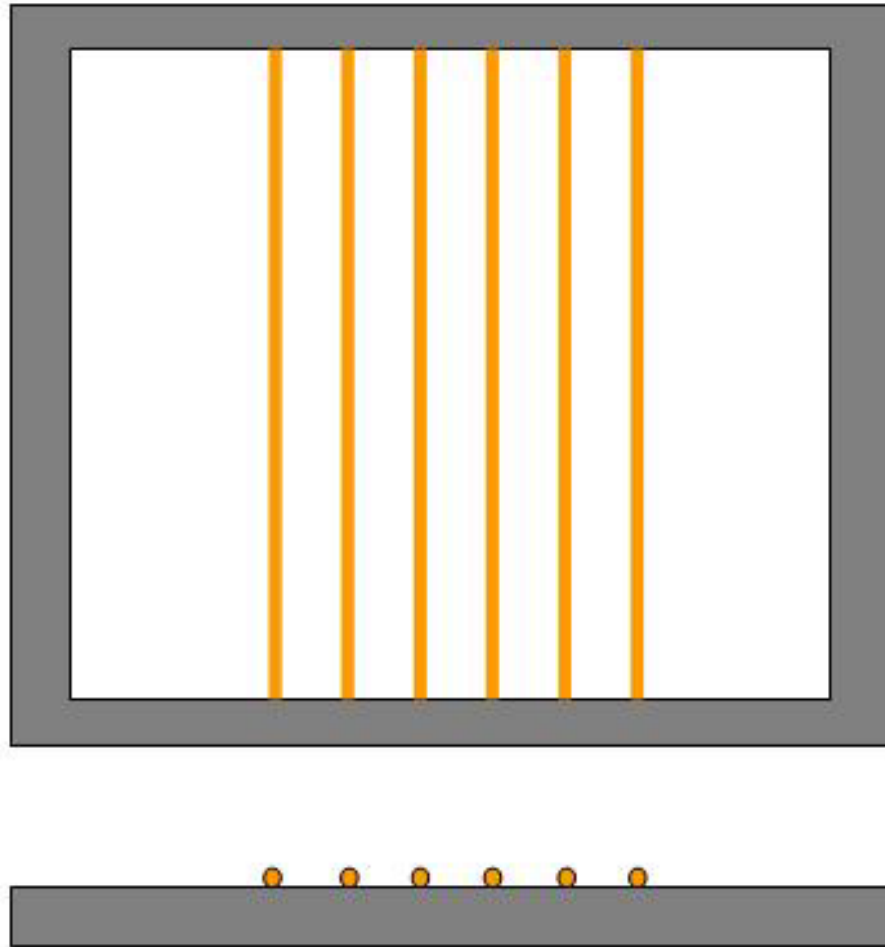


Figure 14. Illustration of planar wire array. The inner square where the wires are strung is 3 cm on a side. The wires were 30 gauge copper or tin-copper and there are grooves every 2 mm for wires.

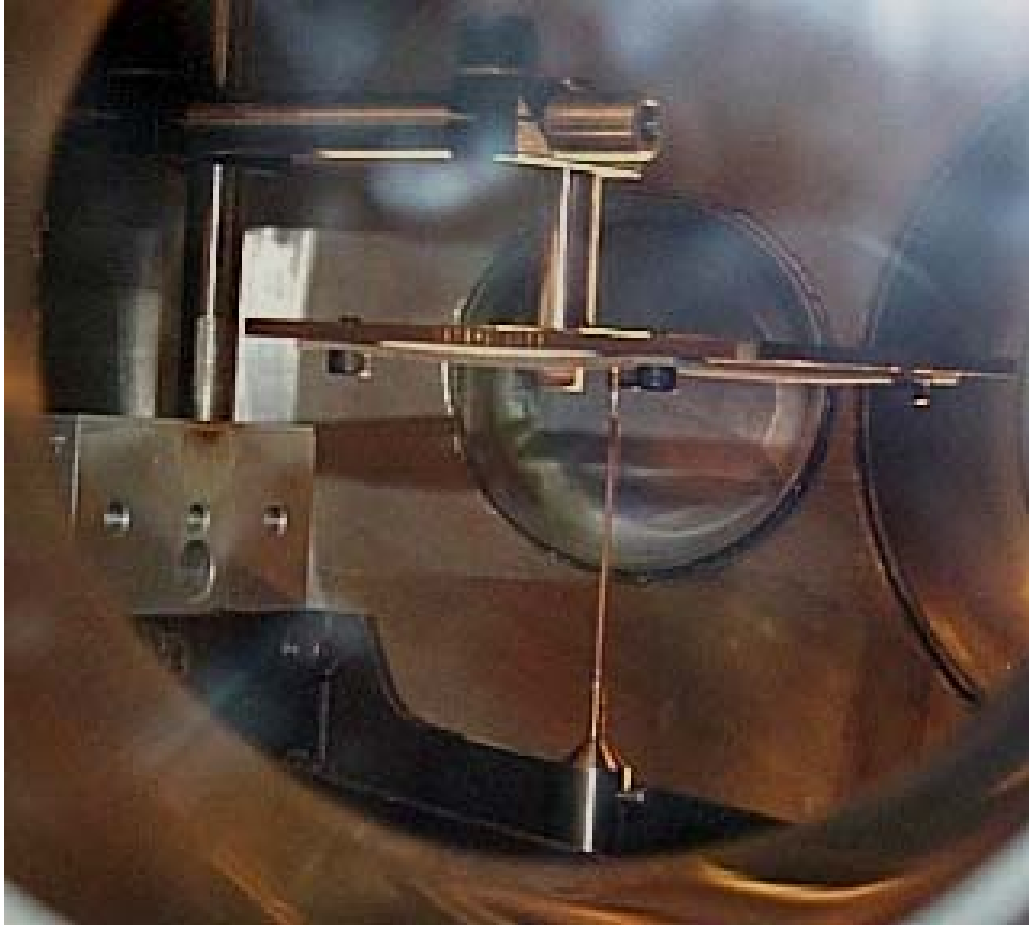


Figure 15. Picture of the planar wire array inside the Z-Beamlet target chamber along with a target wire. The drive laser enters from the right of the picture and the probe beam enters the chamber through a port just to the left of the port through which the picture was taken and exits through the opposite side.

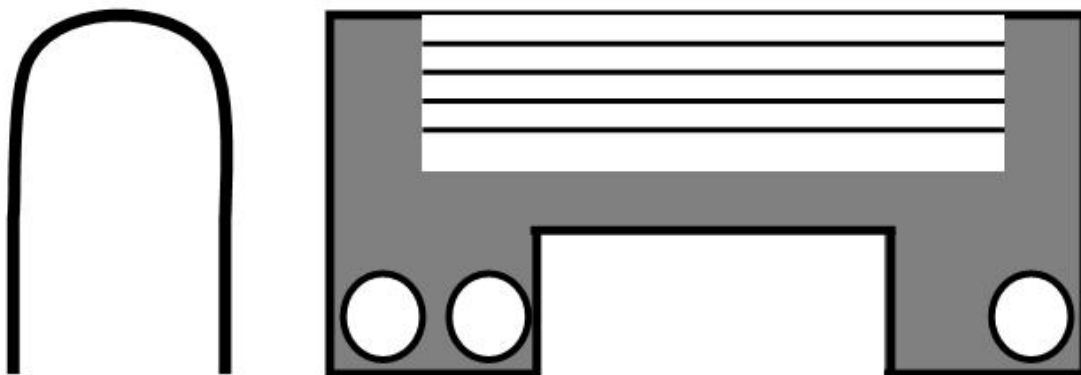


Figure 16. Illustration of cylindrical wire array. The array was designed to be one half of a 1 cm diameter wire array with extended sides so the array could be mounted. Grooves were cut every 1 mm on opposite sides of the array to allow 30 gauge copper or tin-copper wire to be strung.

5.4 Diagnostic Systems

Two main types of diagnostic were employed during the experiments, schlieren diagnostics and various interferometers. For experiments on the Janus there was only one camera to record images for these experiments and so only a single diagnostic could be fielded at a time. For most shots a schlieren telescope was employed, but both a Nomarski and a Michelson interferometer were employed for some shots. For the experiments on Z-Beamlet two cameras were available and a Mach-Zehnder interferometer was fielded on most shots in addition to a schlieren telescope. For these experiments four 50/50 beamsplitters were used at the four corners of the interferometer prior to the imaging lens. The beamsplitter the probe beam hits just prior to entering the chamber (B/S A from Figure 17) and the beam splitter preceding the imaging lens of the interferometer (B/S D) separate and recombine the two legs of the interferometer respectively. The beamsplitter that separates the probe beam after the chamber (B/S C) passes some probe light for use in the schlieren diagnostic. In order to maximize the contrast between light and dark fringes in an interferometer it is necessary to equalize the intensity between the two beams of the interferometer. Therefore a fourth beamsplitter (B/S B) was employed to compensate for the light lost at beamsplitter C to the schlieren diagnostic. The original beamsplitters in this setup proved to be unsuitable possibly because only one side of the optics was coated and thus they were replaced.

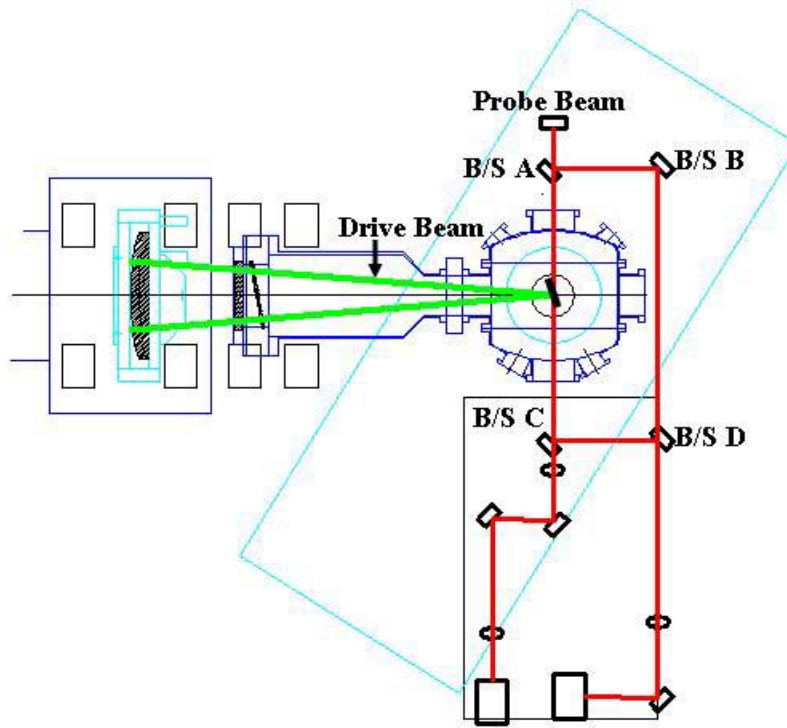


Figure 17. Layout of experimental setup for use with Z-Beamlet laser. Up to 1000 J level drive beam entered the experimental chamber from the left and illuminated a solid target. A probe beam used in both an interferometer and schlieren diagnostic starts at the top of the drawing. The four beamsplitters used in he diagnostics are labeled B/S.

The probe beam entered and exited the experimental chamber through 0.5” thick windows of 4” diameter coated to minimize reflection at both the fundamental (1064 nm) and second harmonic (532 nm) frequency of the probe beam. After early experiments when debris from metal targets damaged some of the windows, similarly coated 0.25” thick windows were used as debris shields and placed between each window and the target.

For all experiments CCD cameras were used to record images from the diagnostics. For the Livermore experiments, a Peltier cooled CCD camera from Roper Scientific was used. This camera had 16 bit dynamic range and a chip approximately 1.3

cm on a side. For the Z-Beamlet experiments three different types of CCD camera were used. The first cameras used were similar to the cameras used at Livermore and had Peltier cooled chips approximately 1.3 cm on a side and 16-bit dynamic range. These became unavailable and for one run Pulnix brand cameras with 8-bit dynamic range and un-cooled chips 13 mm on a side were employed. After this new cameras were obtained from Roper Scientific that had 16-bit dynamic range and Peltier cooled chips over 2 cm on a side. Interference and neutral density filters were placed in front of the cameras in order to isolate the probe light from any other sources and control the intensity of probe light incident on the cameras. Because some of the unconverted 1054 nm light from the Z-Beamlet laser was scattered in the chamber two 4 nm line width interference filters were necessary in each diagnostic leg to properly isolate the 1064 nm wavelength probe laser light from this 1054 nm wavelength light. One interference filter was taped to the front of each camera in order to prevent it from seeing the room lights. The probe light would occasionally ablate material from the schlieren diagnostic pin creating a small plasma. The emission from this plasma created a bright area on the schlieren image. To combat this we put one or two neutral density filters with total optical density (OD) between 1.5 and 2.5 prior to the beam block wire. This eliminated the plasma on the beam block wire and improved the diagnostic. The remaining neutral density filters for the schlieren diagnostic of total OD 3 along with an interference filter were placed in a mount just preceding the camera. The filters in the interferometer beam path were setup in a similar method, with the pre-focus neutral density filters being employed to avoid burning the filters just after the focus, when there was little space before the camera and the intensity of the beam was high. On the Janus shots only one broadband interference

filter centered at 532 nm was necessary in addition to the neutral density filters placed just before the camera. The probe beam on these experiments was weaker and therefore there was no additional plasma created on the beam block wire.

Telescopes were used to image the targets onto the cameras. Because the scale length of the blast waves reached several centimeters and the CCD chips were only 1 cm - 2 cm on a side in size, the telescopes were set up so that they demagnified the image of the target. The Z-Beamlet experiments were set up with approximately a factor of 4-8 of demagnification. During the Livermore experiments there was a lower demagnification factor and in order to follow the evolution of the created blast waves the target was moved relative to the probe beam. Using the target manipulation translation stages it was possible to move the target relative to the probe beam axis. The focus of the drive beam could then be adjusted using a translatable lens to match the new target position. In order to determine the spatial scale in our diagnostics, images of a clear plastic ruler were taken.

During experiments on the Janus laser, only one diagnostic was fielded at a time. A two lens telescope was employed as part of the schlieren diagnostic and to image the target when the interferometer was employed. For the experiments at Z-Beamlet the imaging systems for the interferometer and schlieren diagnostics were separated. The schlieren diagnostic initially utilized a single lens imaging telescope with an approximately 1 m focal length lens. However, significant spherical aberration was seen on images from this setup. Therefore a two-lens imaging telescope with an 80 cm focal length for the first lens in the pair was set up for later runs. The focal length of the second lens varied from 10 cm to 20 cm to vary the demagnification factor of the

telescope. For the interferometer a single lens telescope was utilized. This telescope had a reduced demagnification factor as compared to the two lens telescope for the schlieren telescope. The field of view is inadequate for examining the blast wave at late times, but provides a magnified view for early times. In order to allow the easiest set up of the interferometer, it was desirable that all imaging occur after the beams had been recombined. However, due to space considerations, this made it very difficult to employ a two lens telescope. If the single lens telescope were set up so that the demagnification factor was equivalent to that of the two lens telescope two problems arose. The first was that the focus of the lens became very tight and it was difficult to put any filters between the lens and camera without damaging them. Secondly, the f number of the system became exceedingly small and the image on the camera exhibited significant spherical aberration. Therefore the reduced demagnification factor single lens telescope was employed for most experimental runs.

6. Diagnostics

During the course of the experiments described in the next chapter a number of different diagnostics were employed. This included several different types of interferometers including a modified Michelson, a Nomarski, and a Mach Zehnder. In addition, the primary diagnostic for most experiments was a schlieren telescope.

6.1 Interferometers³⁸

In order to measure the electron density profile in front of our shock waves we employed a number of interferometers. These diagnostics rely on the dependence of the index of refraction of plasma on electron density. This index of refraction change can affect an electromagnetic wave traveling through the plasma, such as a laser beam. It is difficult to calculate the exact effects of a non-uniform plasma on a laser beam. However, when the wave vector changes very little over the distance of a wavelength, the WKBJ approximation³⁹ applies. In this case the phase accumulated by a laser beam when traveling through plasma ϕ is given by:

$$\phi = \int \vec{k} \cdot d\vec{l} = \int \frac{\omega}{c} N dl \quad (1.1)$$

where l is the distance along the ray path and k is the solution of the homogeneous plasma dispersion relation for the angular frequency ω of the laser. N is the refractive

index of the plasma, which in the case where there are negligible magnetic fields can be written as:

$$N = 1 - \frac{\omega_p^2}{\omega^2} = 1 - \frac{n_e}{n_c} \quad (1.2)$$

where

$$\omega_p^2 = \frac{n_e e^2}{\epsilon_0 m_e} \quad (1.3)$$

Here ω is the frequency of the incident laser, ω_p is the plasma frequency and e , m_e , and n_e are the charge, mass, and density of electrons in the plasma. The critical electron density, n_c , is defined as the density where the plasma frequency ω_p equals the frequency of the laser beam ω .

$$n_c \equiv \frac{\omega^2 m_e \epsilon_0}{e^2} \quad (1.4)$$

For a two-beam interferometer where the electric fields of the two beams are given by:

$$E_1 \exp(i\omega t) \text{ and } E_2 \exp(i\omega t + i\phi) \quad (1.5)$$

The combined field is given by:

$$E_t = (E_1 + E_2 \exp(i\phi)) \exp(i\omega t) \quad (1.6)$$

And the intensity of the combined beams is given by:

$$I = |E_t|^2 = [E_1^2 + E_2^2] \left[1 + \frac{2E_1 E_2}{E_1^2 + E_2^2} \cos \phi \right] \quad (1.7)$$

When there is perfect alignment of the beams, ϕ is a constant and the output of the interferometer is a constant intensity field. By creating a small misalignment of the interferometer beams, it is possible to set up a pattern of interference fringes spatially across the combined beam before the experiment. The phase lag in the experimental arm of a two-beam interferometer as compared to the reference arm is proportional to the difference in the index of refraction encountered by the probe beam. Assuming a negligible index of refraction ($N \cong 1$) in the reference arm of the interferometer this is just the difference of equation (1.1) applied to both arms:

$$\Delta\phi = \int (N-1) \frac{\omega}{c} dl = \int \left(\left(1 - \frac{n_e}{n_c} \right)^{\frac{1}{2}} - 1 \right) \frac{\omega}{c} dl \quad (1.8)$$

If the electron density in the plasma is much lower than the critical frequency (or equivalently the frequency of the incident laser beam is much higher than the plasma frequency) then equation (1.8) simplifies to:

$$\Delta\phi \approx \frac{\omega}{2cn_c} \int n_e dl \quad (1.9)$$

The phase change created by traveling through some amount of plasma, such as the plasma that makes up the blast waves in our experiments, can be measured spatially across the beams. Practically this means setting up the interferometer without anything in the experimental area. Then any change in the image is due to the experiment and the

phase change at any point can be measured. This phase change can then be inverted using equation (1.9) to give the integrated electron density through the experimental area.

Three different types of interferometer were fielded during our experiments at different times: modified Michelson³⁸, Nomarski, and Mach Zehnder³⁸. The Michelson and Nomarski interferometers split the probe beam after it had passed through the experimental area and relied on the fact that the probe beam was significantly larger than the interesting experimental space. Due to this fact, the portions of the beam that had gone through pristine gas could be interfered with those portions enclosed by the blast wave.

6.1.1 Michelson Interferometer

A diagram of the modified Michelson interferometer is shown in Figure 18. This setup is slightly modified from what is traditional. The use of a corner mirror in one arm of the interferometer inverts the image in that arm. In our setup the corner mirror inverted the image vertically. This allows an image in one half of the beam to be interfered with undisturbed probe light in the other half. Since the entire image is interfered with a vertically inverted version of itself, two images of the experimental area will appear. It should be noted that in a standard Michelson interferometer the object to be studied would be placed in one of the arms of the interferometer. In this setup the probe beam is interfered with a reference beam from the other arm instead of an inverted image. The corner mirror in the modified setup is replaced by a flat mirror in the

standard setup and only one image of the experiment appears. A sample image of data from our modified Michelson interferometer can be seen in Figure 19.

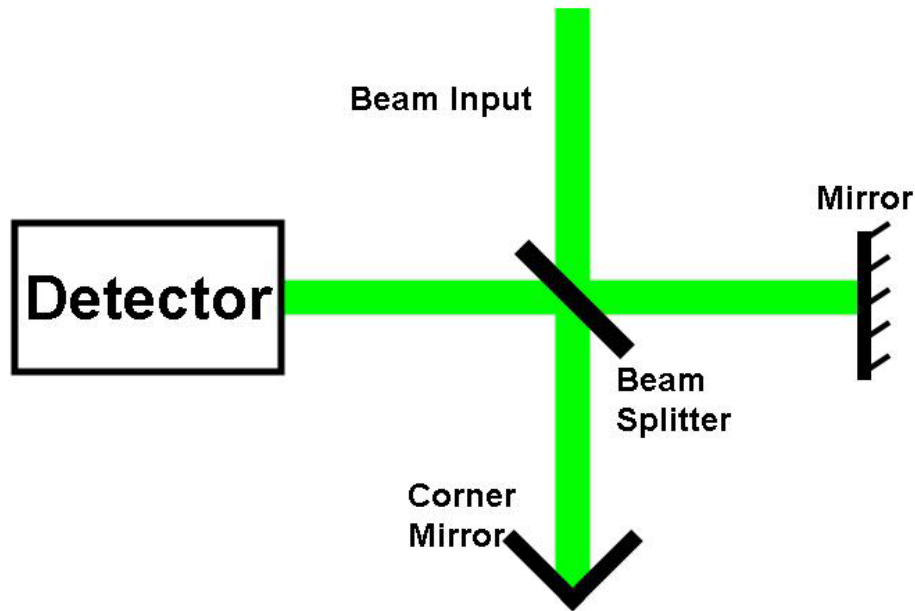


Figure 18. Diagram of a modified Michelson interferometer. The probe beam enters from the top, is split by the beamsplitter in the center, enters both arms, and is recombined before entering the detector. Use of a corner mirror in one arm causes the reflected image to invert allowing the interference of one half of the beam with the other half.

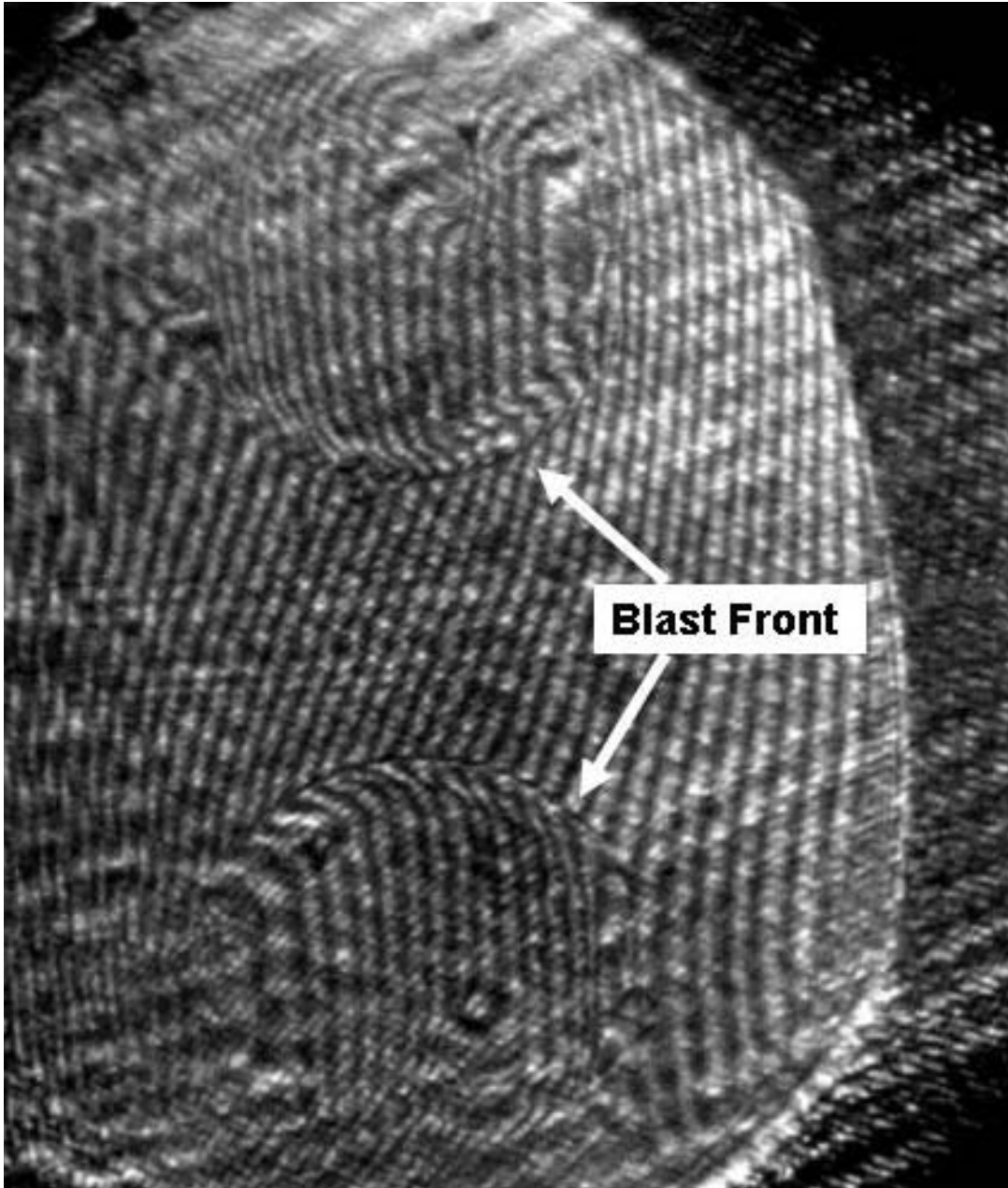


Figure 19. Sample image from Michelson interferometer. The probe beam has been interfered with a vertically mirrored image of itself. The image is of a blast wave traveling in 5 Torr of nitrogen gas produced by a 100 J laser pulse 100 ns earlier.

6.1.2 Nomarski Interferometer

The Nomarski interferometer makes use of a Wollaston prism to split the probe beam based on polarization. A diagram of this type of interferometer is shown in Figure 20. Probe light passes through the experimental region. It then goes through a polarizer to ensure it is linearly polarized with an angle of polarization 45° offset from the axis of the Wollaston prism. The next item in the optics chain is a lens that images the target onto the detector. Then the Wollaston prism splits the probe light into two orthogonal polarizations. The two polarizations are sent out at a slight angle relative to each other. A second polarizer set along the original polarization direction of the probe light recombines the two beams, creating an interference pattern which is observed. A sample image can be seen in Figure 21. Much like in the modified Michelson interferometer, the undisturbed part of the probe beam is interfered with that portion that passed through the experimental region and two images of the blast wave are created.

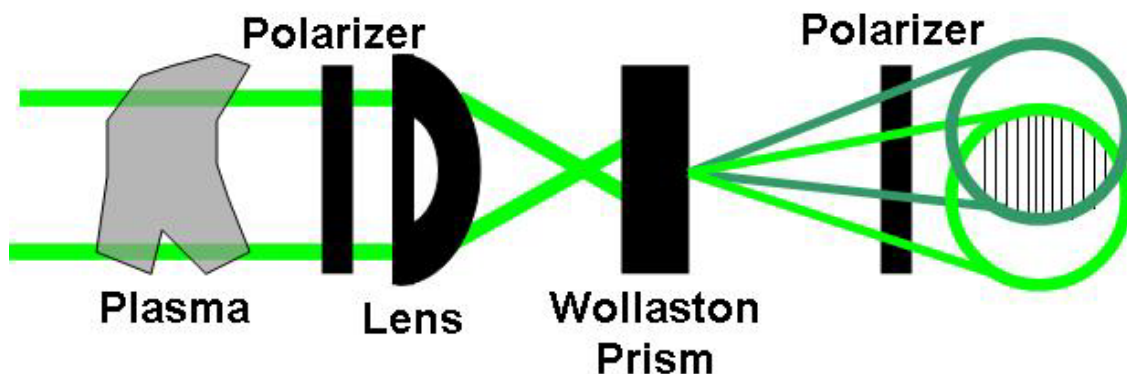


Figure 20. Diagram of Nomarski interferometer. The first polarizer ensures the probe light has one polarization. The Wollaston prism splits the probe light into two orthogonal polarizations, each 45 degrees off that of the original probe light. The final polarizer recombines the light back into the original polarization and creates the interference pattern.

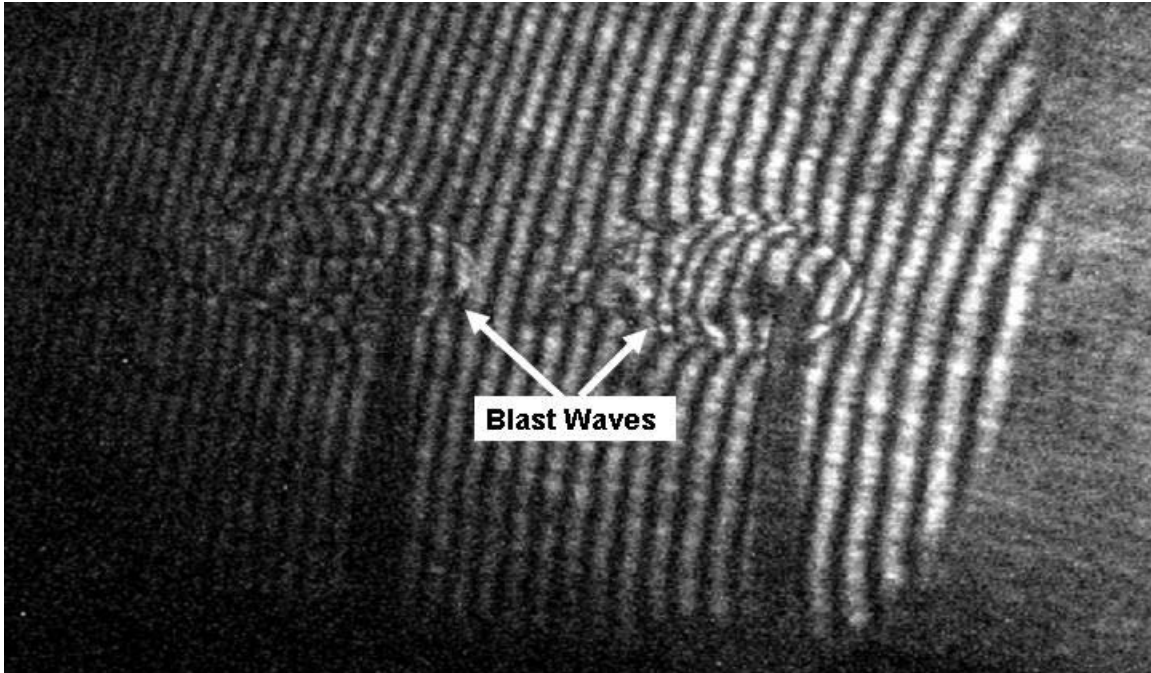


Figure 21. Image from Nomarski interferometer. Notice double image, one from each polarization of light. The image is of a blast wave traveling in 5 Torr of nitrogen gas produced by a 10 J laser pulse.

6.1.3 Mach-Zehnder Interferometer

The Mach Zehnder Interferometer is somewhat different from the modified Michelson and Nomarski interferometers described previously in that the experimental image is interfered with a separate reference beam and not a part of the same beam. This difference enabled imaging of larger areas as there is no need for $\frac{1}{2}$ the probe beam to go through undisturbed gas. A diagram of this type of interferometer is shown in Figure 22. In this interferometer the probe beam is split before entering the experimental area into imaging and reference arms. The imaging arm passes through the experimental area experiencing a phase shift. The reference arm passes through empty space. This allows the change in index of refraction due to the plasma in the experiment to be measured. A

sample image from the Mach-Zehnder interferometer used in our experiments is seen in Figure 23.

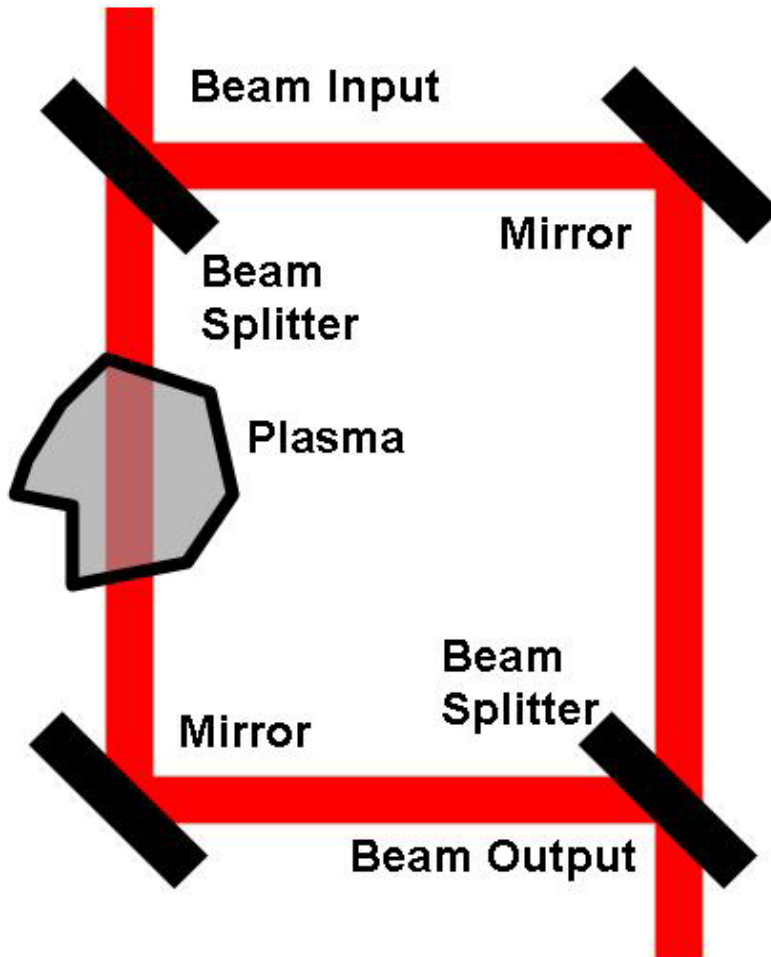


Figure 22. Diagram of Mach Zehnder interferometer. The probe beam is split into imaging and reference arms. The imaging arm passes through the area of the experiment and the reference beam through empty space. The two arms are recombined at the end of the interferometer.

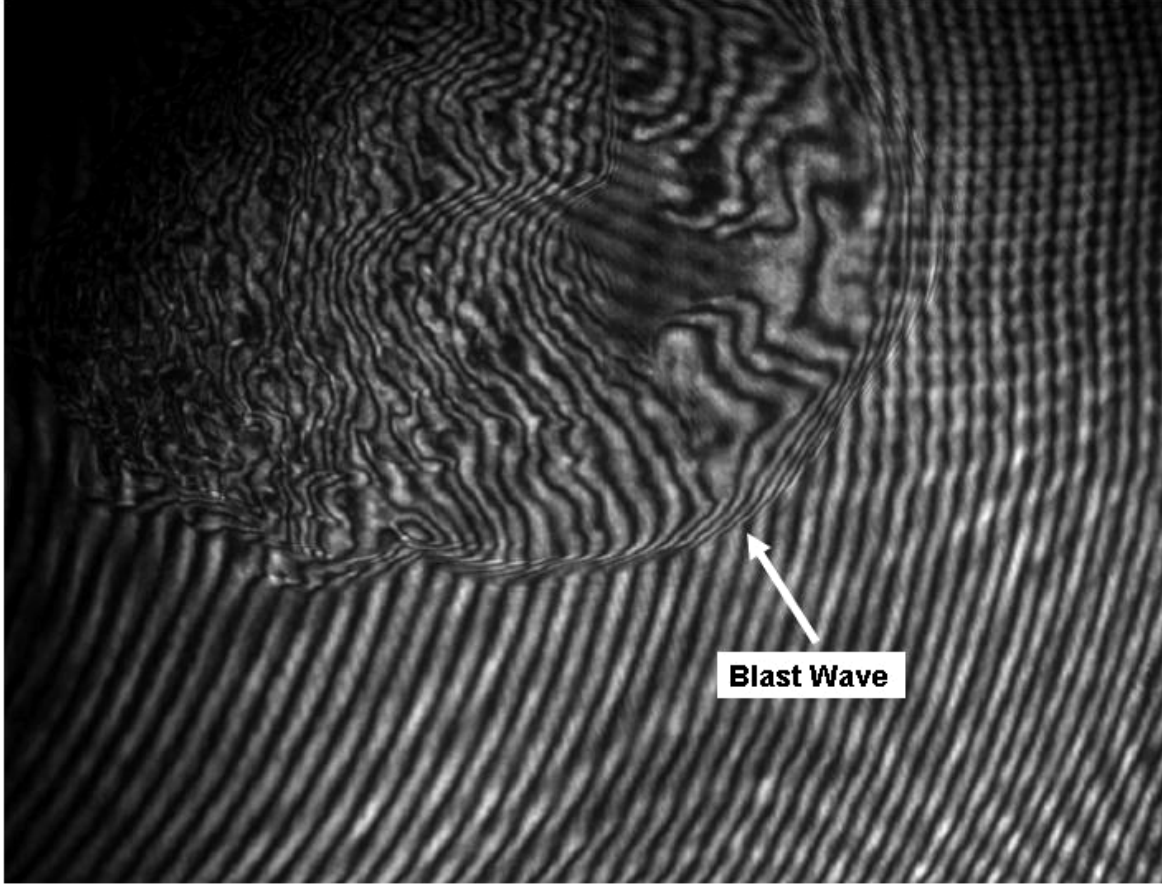


Figure 23. Sample Mach-Zehnder Interferometer image. The probe beam is interfered with a portion of the beam that had been split off prior to entering the experimental image, thus there is only one image. The image is of a blast traveling in xenon gas created by a 1000 J laser pulse.

6.1.4 Abel Inversion³⁸

The electron distribution for a cylindrically symmetric plasma can be inferred using a technique known as an Abel inversion. This technique allows any quantity for which the available measurement is a chord integral in a cylindrically symmetric media to be converted to a function of radius. In Cartesian coordinates, the chord integral takes the form:

$$F(y) = \int_{-\sqrt{a^2-y^2}}^{\sqrt{a^2-y^2}} f(r) \, dx \quad (2.1)$$

Where x is the dimension the laser travels, y is the perpendicular dimension along which measurements are made and $f(r)$ is the quantity to be measured as a function of radius, electron density in our experiments, and $F(y)$ is the measured quantity integrated along chords through the material. The coordinate system is illustrated in Figure 24. The integral over x in (2.1) can be converted to an integral over r :

$$F(y) = 2 \int_y^a f(r) \frac{r \, dr}{\sqrt{r^2 - y^2}} \quad (2.2)$$

This transform can then be inverted to yield an equation for the radial distribution of our quantity given the chord integrals:

$$f(r) = -\frac{1}{\pi} \int_r^a \frac{dF}{dy} \frac{dy}{\sqrt{y^2 - r^2}} \quad (2.3)$$

In order to get an absolute measurement from equation (2.3) it is necessary that $f(a) = 0$. In practice this means that a small amount of the probe beam must pass through undisturbed gas. Using (2.3), we can get the radial electron density distribution from the chord integrals derived from the interferometer.

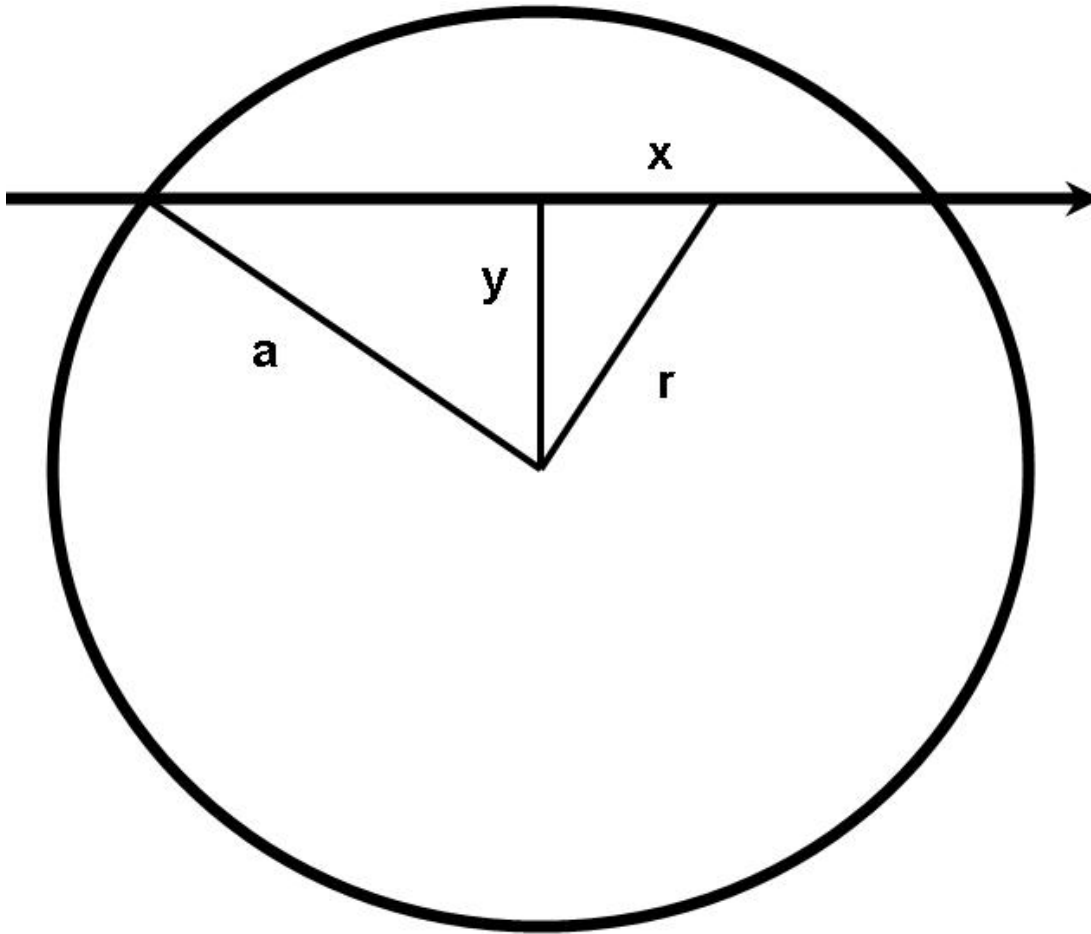


Figure 24. Illustration of coordinates used in Abel Inversion. The laser propagation direction is x and y is the perpendicular coordinate in the image along which a phase measurement is made. The full radius of the cylinder is a and the radial coordinate is r .

6.2 Dark-Field Imaging

Also known as a Schlieren diagnostic, dark-field imaging is sensitive to the index of refraction of a plasma much like an interferometer. However, in this case the laser beam used is not split. A diagram of a schlieren telescope is seen in Figure 8. The basis of dark-field imaging is a telescope set up to image the experimental area. An object such as a wire or razor blade is then used to block the focus of the telescope, creating a

dark field at the image plane if the telescope when the experimental area is undisturbed. Any plasma created will cause index of refraction changes along the beam path. These index of refraction changes deviate the beam by an angle θ given by:

$$\theta = \frac{d}{dy} \int N dl$$

Here dl is an integral along the beam path, and y is any spatial coordinate perpendicular to the beam propagation direction. The deviated light will pass around the beam block and emerge from the telescope. The size of the beam block and the focal properties of the laser determine the sensitivity of the diagnostic. This creates bright areas at the image plane of the telescope wherever there are large index of refraction gradients, i.e. large density gradients. This makes this diagnostic ideal for looking at systems where a large density gradient is expected, such as the edge of a blast wave. We have primarily used this diagnostic to look at small spatial scale features in the blast front. A sample image is seen in Figure 9.

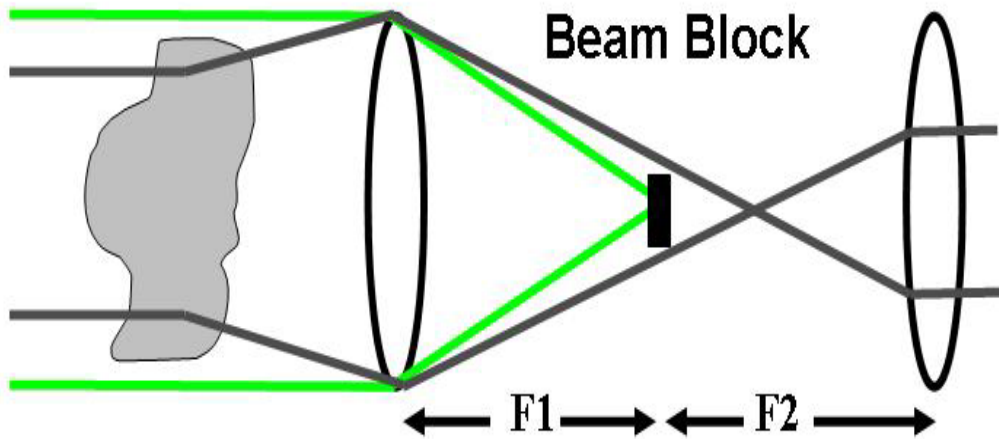


Figure 8. Diagram of a schlieren telescope. This diagnostic is essentially an imaging telescope with a beam block at the center. Index of refraction changes in the imaged material cause deviation of the laser light so it passes around the beam block.

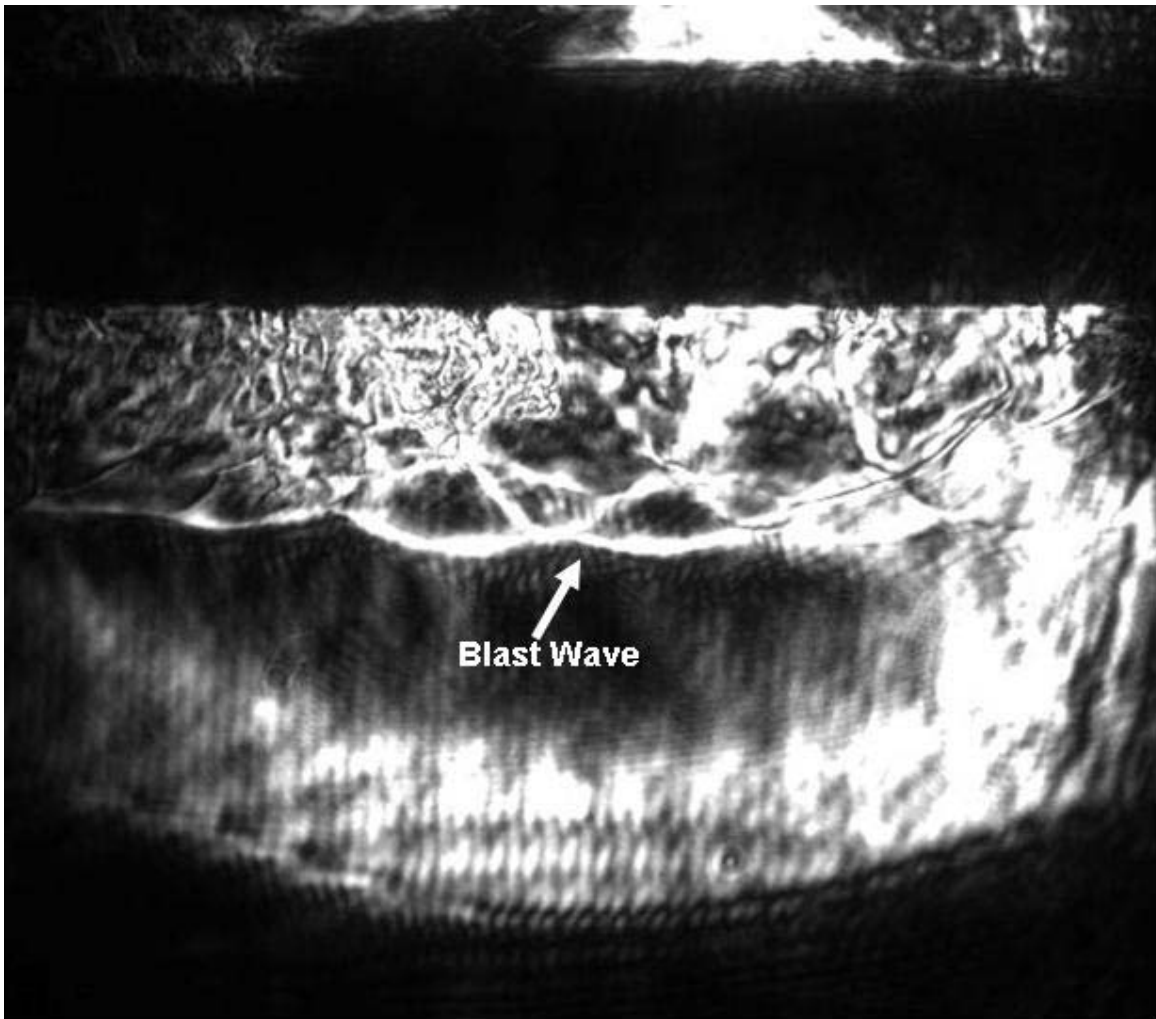


Figure 9. Sample image from schlieren telescope of a blast wave traveling past a wire array. Small scale features of the blast wave can be seen using this diagnostic. The image is of a blast wave traveling in 10 Torr of xenon past a 6 mm spaced wire array. The blast wave was created by a 1000 J laser pulse 2000 ns earlier.

7. Experimental Description

We performed experiments exploring the properties of high Mach number blast waves created in a number of different background gasses. The results of these experiments can be separated into three basic areas. The first set of results concern the amount of radiation produced by the blast front and its impact on the evolution of the blast wave. The next area is the effect of the drive laser on the evolution of blast waves. Finally, a number of experiments were performed examining the evolution of perturbations on the surface of the produced blast waves. This included examining the possibility of perturbations growing from noise, as well as measuring the evolution of perturbations induced on the blast wave surface.

7.1 Diagnosis of Radiation

A number of features observed during our experiments allowed us to diagnose the importance of radiation on blast wave evolution as a function of background gas. This included the trajectories of the blast waves, the presence and size of a radiative precursor and the ablation of wires in the blast wave path. In addition, in certain cases we can get an estimate of the amount of energy present in the radiative precursor.

7.1.1 Effect of Radiation on Blast Wave Trajectory

As has been previously discussed, the trajectory of a blast wave can provide insight into the importance of radiation on its evolution. For an energy conserving blast wave the trajectory will closely follow the Taylor-Sedov solution^{27, 40} and evolve as $R \propto t^{0.4}$. Radiation causes a blast wave to lose energy, decelerating more quickly than the energy conserving Taylor-Sedov solution predicts. To gain insight into the effect of radiation on our blast waves, we measured the trajectory of blast waves in multiple gasses produced by various drive energies.

The radial trajectories of blast waves produced by both 500 J and 1000 J laser pulses in 5 Torr -10 Torr of both xenon and nitrogen gas were measured. In addition, the trajectory of blast waves produced in a mixture of these gasses by 1000 J laser pulses was measured. The mixed gas used in these experiments was 7.5 Torr xenon gas and 2.5 Torr nitrogen gas by pressure and all further references to mixed gas will refer to this mixture. The reason behind this choice of gas mixture will be explained later in this chapter.

Images of blast waves in xenon at various times after a 1000 J level drive beam hit a plastic target are shown in Figure 25. As can be seen, the blast waves are somewhat elliptical. The smaller vertical axis was chosen to serve as the radius of the blast wave. The reason for this decision was that the larger axis was often difficult to measure for two reasons. The first reason is that the edge of the blast wave closest to the drive laser input was out of the field of view of the diagnostics at late times as seen in the 800 ns panel of Figure 25. In addition, effects from the drive laser that will be discussed later in this chapter cause this same edge of the blast wave to be unreliable. The smaller axis was

therefore more reliable and blast wave trajectories were measured in terms of this axis.

Similar images for blast waves in nitrogen gas and mixed gas are shown in Figure 26 and Figure 27 respectively.

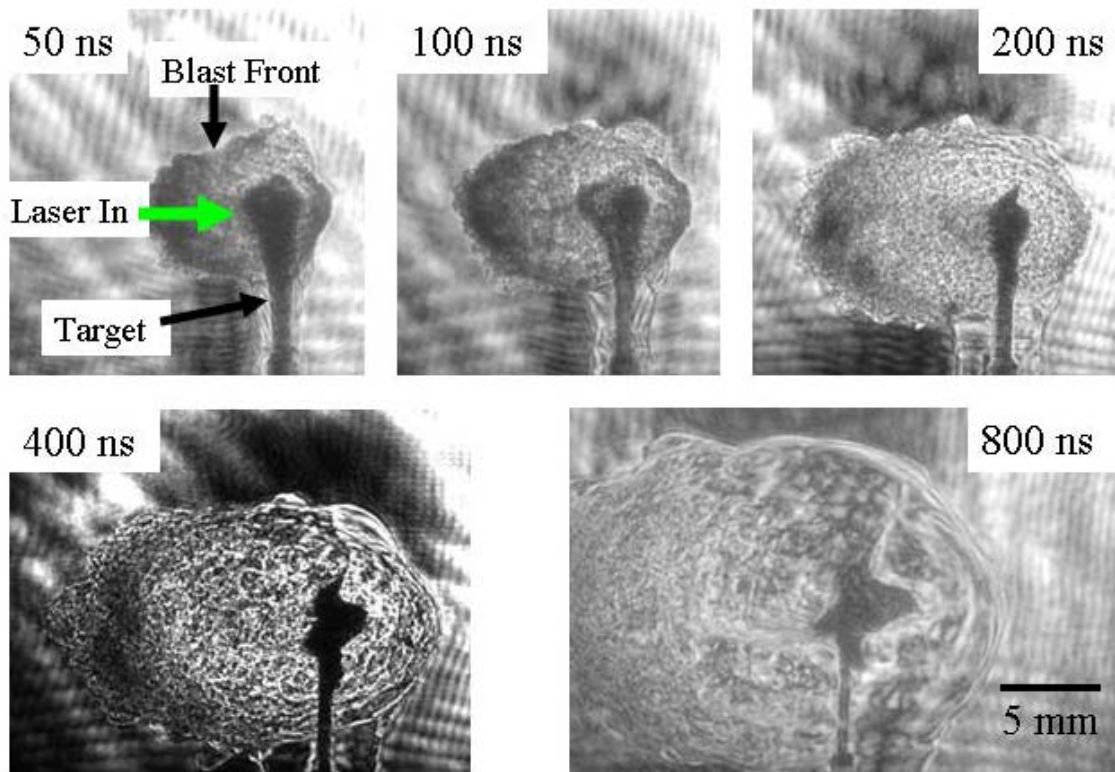


Figure 25. Images of Blast waves traveling through 10 Torr of xenon gas. The images were taken between 50 ns and 800 ns after a 1000 J level drive beam hit the target.

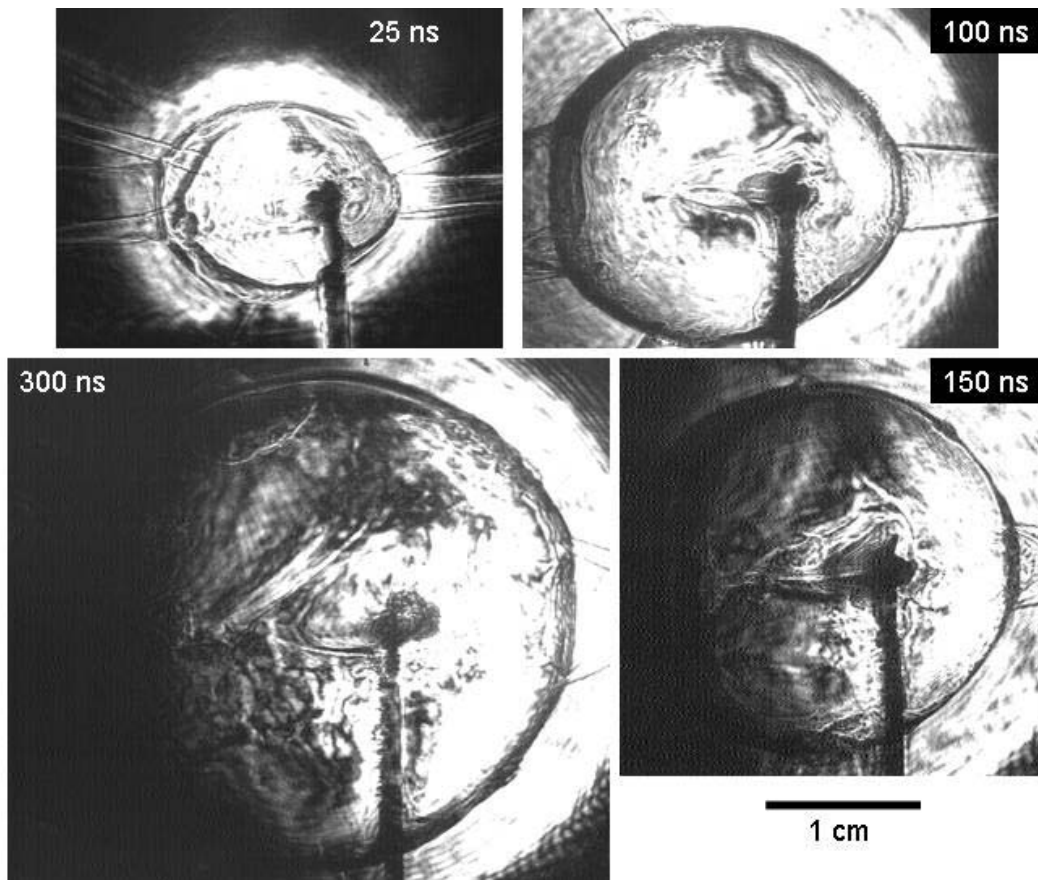


Figure 26. Images of blast waves traveling in 10 Torr of nitrogen gas. The blast waves were created by 1000 J level laser pulses. The images were taken between 75 ns and 300 ns after the drive beam hit the target.

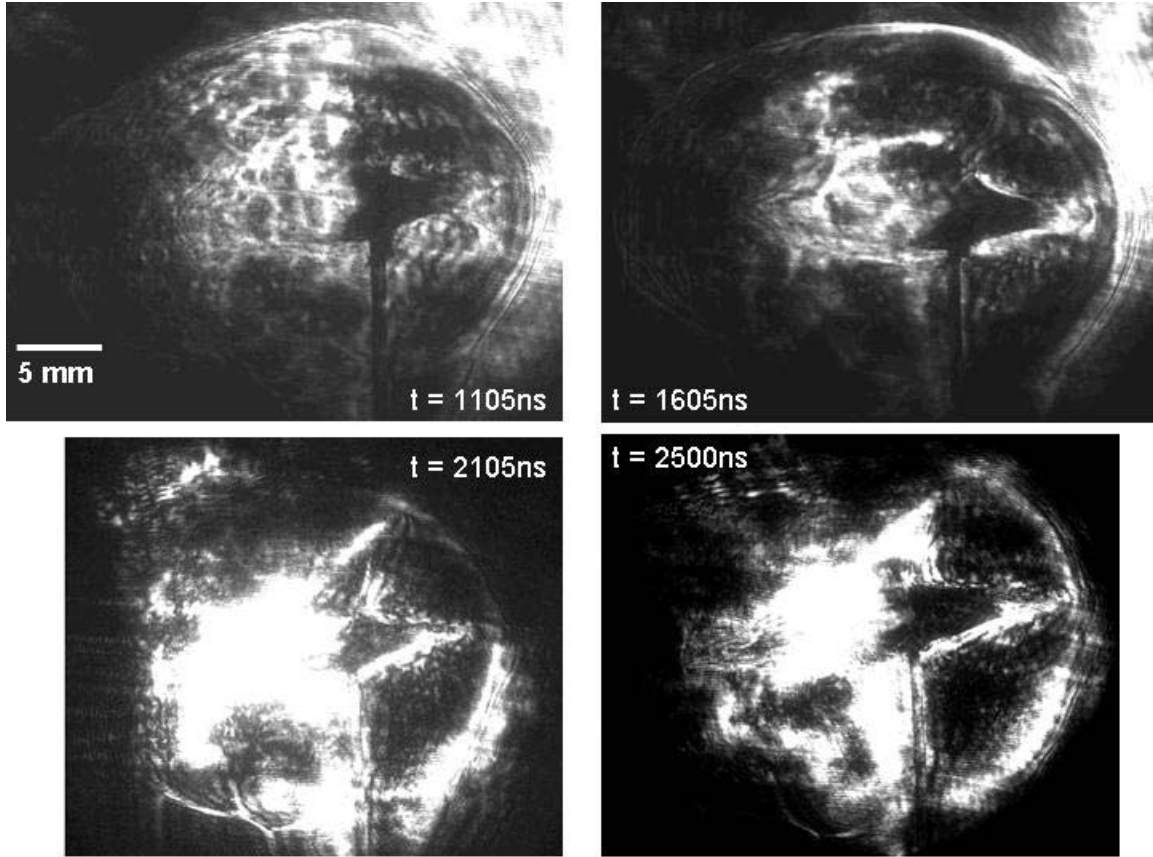


Figure 27. Images of blast waves traveling through a mixture of xenon and nitrogen gas. The imaging system was being aligned between shots causing some images to appear blurry. Blast waves were created by a 1000 J level laser pulse

For laser drive energies at or below the 500 J level the blast wave trajectories in both xenon and nitrogen gas follow the Taylor-Sedov solution. At the 1000 J level of drive energy deviations from this behavior begin to develop. The measured blast wave trajectories produced by a 1000 J laser drive in both xenon and nitrogen gas as well as our mixed gas are seen in Figure 28. The trajectory in nitrogen has a best fit for the temporal exponent of 0.38 ± 0.02 , consistent with the Taylor-Sedov solution. The limited mixed gas data has a best fit for the temporal exponent of 0.45 ± 0.03 , slightly above the Taylor-Sedov solution but reasonably close considering the relatively small data set. In contrast, the blast waves in xenon have a more complicated evolution. At

times less than 200 ns the blast waves in xenon clearly follow a non-Taylor Sedov trajectory, and in fact are consistent with the momentum conserving snowplow⁴¹ regime $t^{0.25}$. After 500ns, the blast wave settles into a Taylor-Sedov like regime. The data between these two times is roughly consistent with both exponent values and may represent a transition region. The early time behavior of blast waves in xenon implies that energy lost via radiation is having a significant effect on the hydrodynamics.

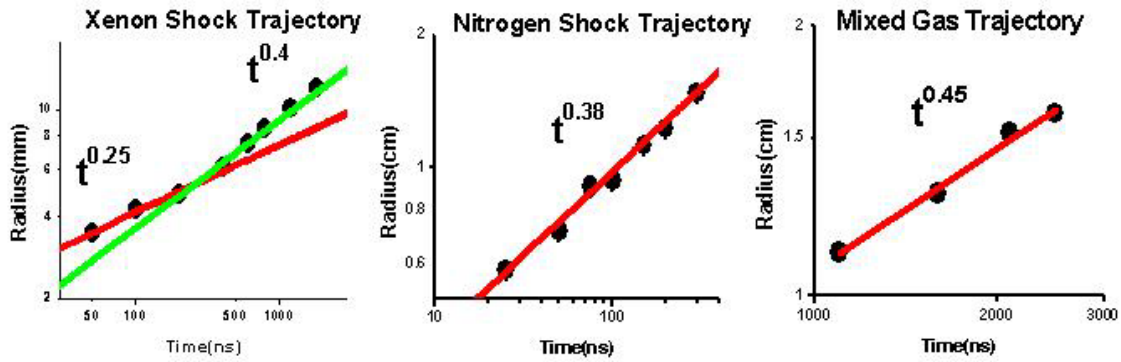


Figure 28. Trajectories of blast waves traveling through xenon and nitrogen gas as well as a mixture of the two gasses. The blast waves were created by a 1000 J level laser pulse. Error bars are smaller than the data points.

There is one other result that can be obtained from the trajectory information given: the Mach number of the blast waves compared to the sound speed of the background gas. The sound speed of nitrogen and xenon gasses are 334 m/s and 1.09 km/s respectively. Looking at the average velocity between trajectory points, we can estimate the range of velocities the blast waves in the various gasses go through during the time their trajectories were tracked. For blast waves in xenon the velocity ranges from 15 km/s to 1.5 km/s over the measured timed range leading to Mach numbers from 1.4 to 14. Since nitrogen is lighter the blast waves in that gas travel faster and the

velocity ranges from 52 km/s to 25 km/s corresponding to Mach numbers from 75 – 156. For the mixed gas data, the measured trajectory starts at a much later time and so the speeds measured are correspondingly slower and range from 3.7 km/s to 2 km/s. The Mach number in this gas is unknown as it is a mixture of the other two. Using the xenon sound speed as an upper value leads to Mach numbers from 1.8 to 3.4 as a lower bound.

7.1.2 The Radiative Precursor

Another indication of the presence and strength of radiation from a blast wave is the radiative precursor that proceeds it³². A radiative precursor is a region of heated, ionized gas preceding the shock front created when radiation from the shocked gas is absorbed by the surrounding background gas. Evidence for radiative precursors appears in both our schlieren and interferometry data. For both diagnostics, the effect of the ionized electrons in the precursor is seen. In the schlieren diagnostic the electron density gradient in the precursor causes an index of refraction gradient that deflects the probe light and allows it to past the beam block in the schlieren telescope. This shows up as a glow in front of the shock front. The Mach-Zender interferometer enables an estimate of the electron density in the precursor through use of an Abel inversion technique. The extent of the radiative precursor varied with the type of background gas. An example of schlieren and interferometer images in helium are seen in Figure 29. Here there only a slight deviation of the fringes outside the blast front in the interferometer and no glow surrounding the blast wave in the schlieren image. These are both indications of very little ionization of the background gas. This can be compared to the schlieren and

interferometry data for shocks in nitrogen 150ns after a 1000J level drive seen in Figure 30. The area of strongly deviated fringes preceding the shock front in the interferometer image and the distinct glow in the schlieren image are indicative of a strongly ionized precursor. With this image, it was possible to perform an Abel inversion³⁸ as described in chapter 6. This gives an estimate that the gas just in front of the shock is ionized 2.5 times on average. A similar level of radiative precursor is seen in the mixed gas as is shown in Figure 31. Here the interferometer imaging system provides less demagnification and so the fringes extend off the field of view and an Abel inversion is not possible. However, the glow region in the schlieren imaging is of similar extent to that in Figure 30. For the xenon data the precursor is more extensive and extends off the field of view as is seen in Figure 32, making a quantitative estimate of the ionization state impossible. The extent of the xenon precursor is further illustrated by the glow extending throughout the field of view in the images in Figure 25.

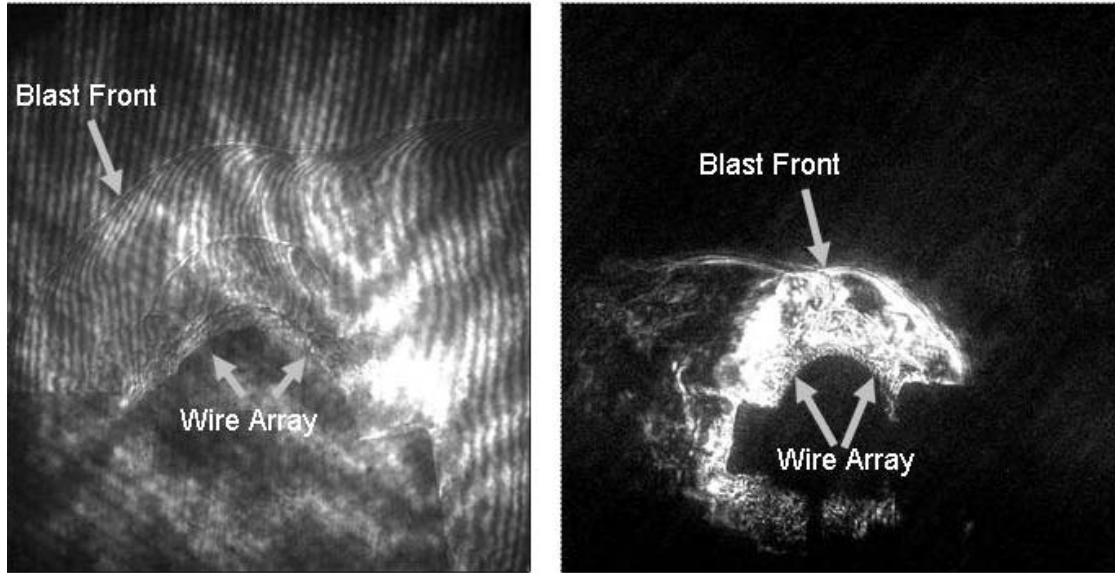


Figure 29. Interferometer and schlieren images of a blast wave traveling in helium gas 300 ns after being produced by a 1000 J laser pulse. The array has traveled past a 4 mm spaced wire array. There is little deviation of the fringes outside the blast front in the interferometer and no glow in the schlieren image, indicating no radiative precursor.

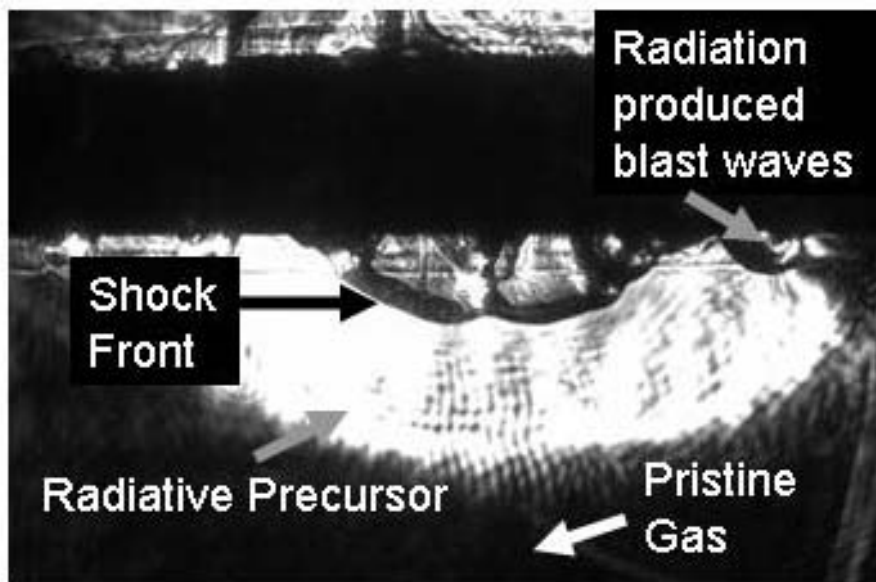
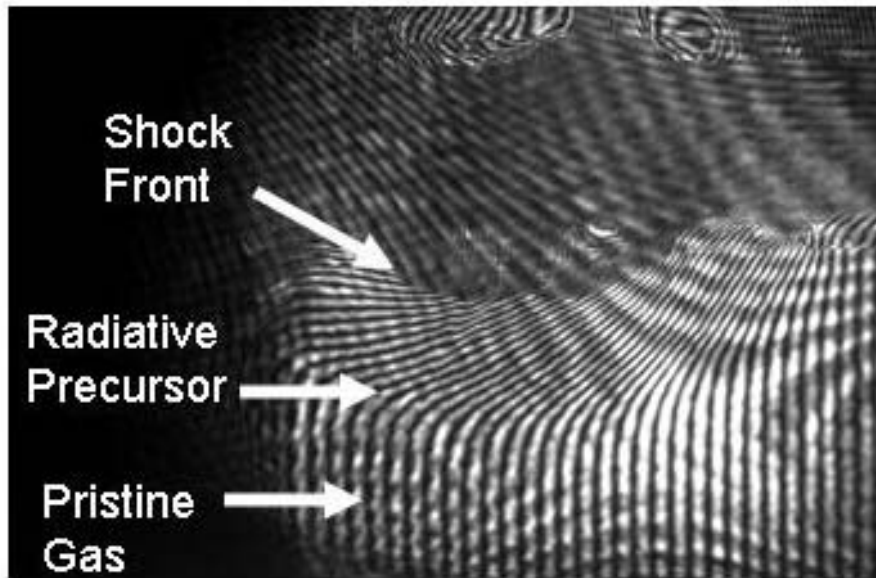


Figure 30. Images of a blast wave in nitrogen traveling past a 4mm spaced wire array 150 ns after a 1kJ drive laser beam struck a plastic target. The top image is from a Mach-Zehnder interferometer and the bottom from a schlieren telescope.

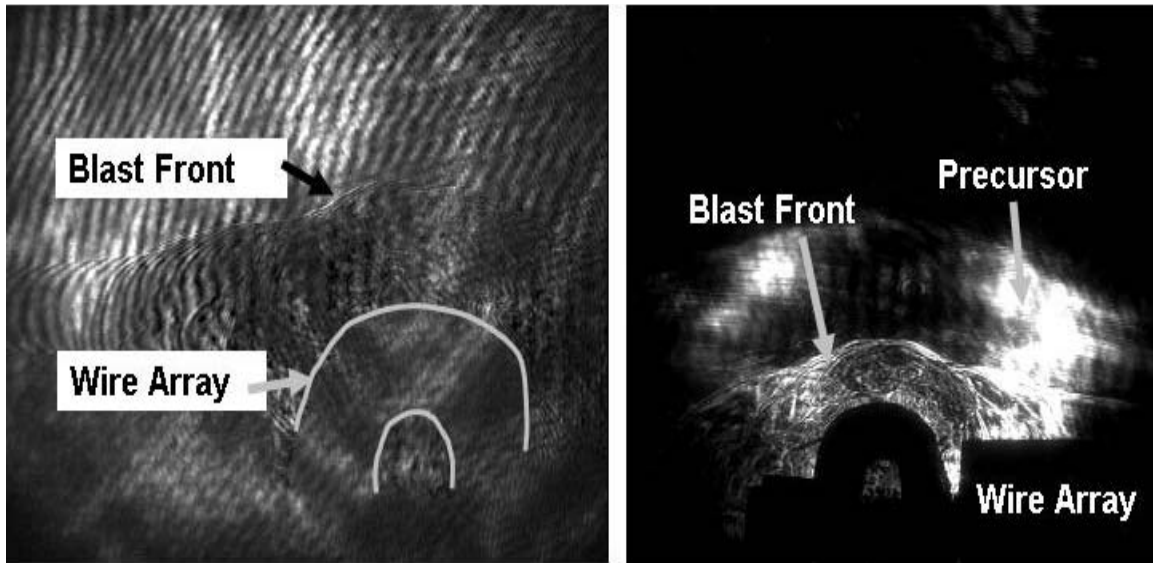


Figure 31. Interferometer and schlieren images of a blast wave traveling in a mixed gas 1400 ns after being produced by a 1000 J laser pulse. The gas is 7.5 Torr of Xenon and 2.5 Torr of N₂ by pressure. The wave has passed by a 3mm spaced wire array. There is moderate deviation of the fringes in the interferometer and a visible glow in the interferometer.

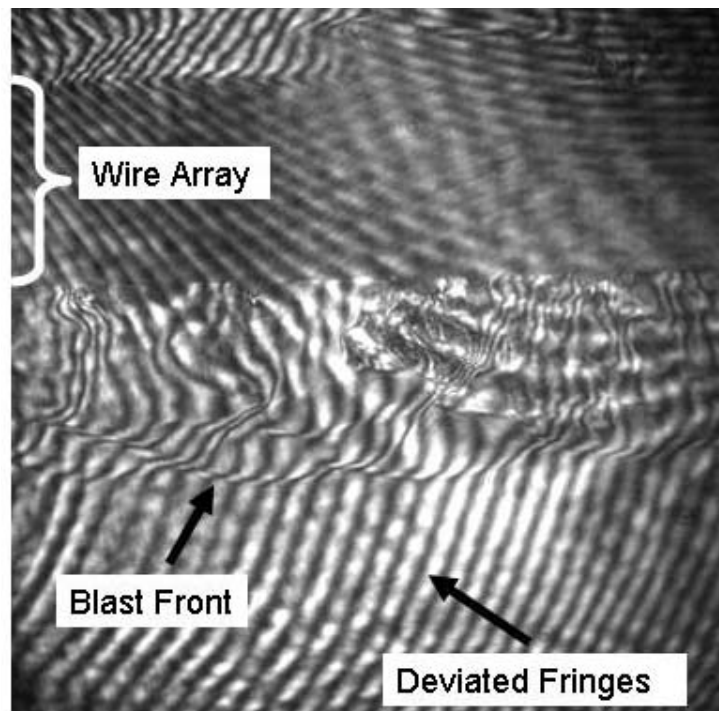


Figure 32. Image of blast wave traveling in xenon 2000 ns after being created by a 1000 J laser pulse. The blast wave is passing a 6 mm spaced wire array. Note the deviated fringes extend off the edge of the viewing area.

7.1.3 Ablation of Wires by Radiation

The final indication we have that our blast waves are radiating energy away is the effect of this radiation on wire arrays placed in the path of the blast wave. Radiation from our blast waves ablates material from the wires in the arrays, creating small blast waves that precede the main blast wave. Much like the radiative precursor, the strength of this effect varies with the background gas. This effect is fairly small for blast waves in nitrogen as seen in Figure 30. These small shocks do not affect observations of the main blast wave. For blast waves in pure xenon, the effect is much larger as shown in Figure 33. These additional waves interfere with our measurement, meaning pure xenon could not be used as a target gas. Our gas mixture was chosen to maximize the effect of radiation on the blast waves while not producing additional blast waves large enough to interfere with our measurements. We tested a 5 Torr xenon and 5 Torr nitrogen mixture and found the additional blast waves stayed at a manageable level. We then tested a mixture of 7.5 Torr xenon and 2.5 Torr nitrogen and discovered that this level was marginally manageable depending on the experimental setup. Figure 34 shows two images of blast waves traveling through a gas mixture of 7.5 Torr xenon and 2.5 Torr nitrogen by pressure. Each blast wave was created by a 1000 J laser pulse. The only difference in the two experimental setups is that the copper wires in the array in the left hand image are armored with plastic. The presence of this plastic enhances the size of the additional blast waves to the point that they interfere with the measurement of the main blast wave. If the image on the left is carefully examined a blast wave very similar to that present in the right hand image can be identified. However, the additional blast

waves make it difficult to discern. The significant effect of the plastic coating on the copper wire is indicative of the fact that the chosen gas mixture represents among the highest percentages of xenon possible before the radiation effects make data analysis impossible.

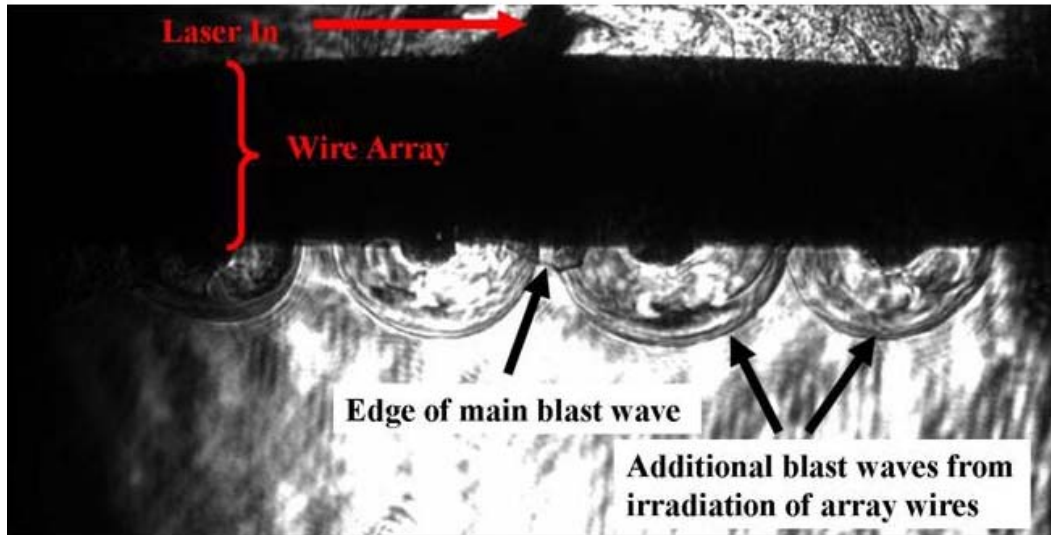


Figure 33. Image of a blast wave in xenon passing a 9mm spaced wire array. Radiation from the main blast wave has ablated the wires in the array, creating many additional blast waves the interfere with the measurement of the main wave.

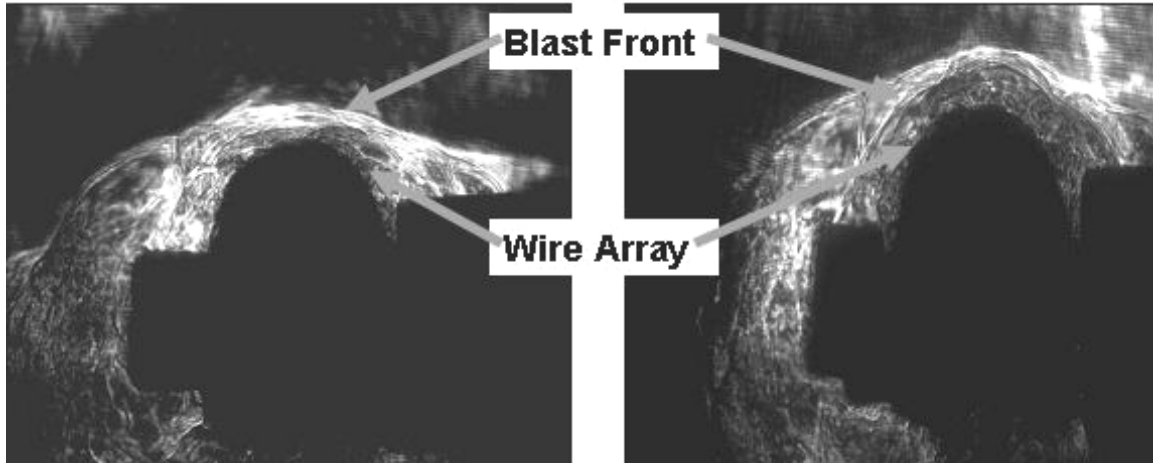


Figure 34. Two images of blast waves traveling past 4 mm spaced wire arrays immersed in a mixed gas. The gas is 7.5 Torr xenon and 2.5 Torr nitrogen by pressure. Each blast wave was produced by a 100 J laser pulse. The wires in both arrays are copper, but those in the left image are coated in plastic. The addition of the plastic increases the size of the blast waves ablated off the wires, interfering with the main blast wave.

The combination of effects on blast wave trajectory, the radiative precursor, and the additional blast waves strongly indicates that the blast waves we created were radiating energy away. Furthermore, the amount of radiated energy depended on the background gas used, scaling with the atomic number of the gas used. This scaling arises from the increased importance of line and bound-free radiation in higher atomic number elements due to lower ionization thresholds.

7.1.4 Estimate of Radiated Energy

The radiative precursor data discussed earlier in this chapter can be used to estimate the total energy in the radiative precursor. The energy in the precursor takes two forms, temperature of the gas and that energy used to ionize the gas. As was mentioned the Abel inversion technique described in chapter 6 can be used to determine the ionization state of the gas in the radiative precursor when the entire precursor is in the field of view of the

interferometer, which in our experiments was only for the blast waves in nitrogen. We can then estimate the temperature necessary to achieve this ionization state and combine these two estimates to get the total energy in the precursor. The energy due to ionization will be given by the product of the number of atoms in the gas and the ionization potential of the average charge state. The kinetic energy of each atom is given by $\frac{3}{2}kT$, where k is the Boltzmann constant and T is the temperature of the gas.

We have performed this analysis for the nitrogen data at 150 ns discussed earlier in the chapter. We estimate this gas to be ionized 2.5 times on average from an Abel inversion of the interferometry data. The second ionization potential of nitrogen is 29.6 eV and the third ionization potential is 47.5 eV. Averaging these two numbers give us 38.5 eV per atom in ionization energy. We can also estimate the temperature of the nitrogen gas necessary to ionize to this level is approximately 5 eV. This temperature implies around 7 eV of kinetic energy per atom, leading to a total energy of 45.5 eV per atom in the radiative precursor.

The number of atoms in the precursor can be estimated by looking at the inner and outer radius of the precursor relative to the center of the blast wave and multiplying the total contained volume by the density of the background gas. There should be little to no change in the density of the gas in the region of the precursor as compared to the background gas. The precursor seen in Figure 30 surrounding the blast wave in nitrogen after 150 ns has an inner radius of 1.25 cm and an outer radius of 1.8 cm leading to a total contained volume of 16.25 cubic centimeters (ccs). The density of nitrogen at 10 Torr pressure is 1.6×10^{-5} g/cc leading to a total mass of 2.6×10^{-4} g. Nitrogen has an atomic mass of 14 atomic mass units and an atomic mass unit is 1.66×10^{-24} g meaning there are

$1.12 * 10^{19}$ nitrogen atoms in the radiative precursor and $5.1 * 10^{20}$ eV or 85 J of energy in the precursor. This puts a lower bound on the total energy radiated by the blast wave during its evolution.

In order to get an idea of how large this number is, we can also look at the ionization energy in the plasma. From the simulation results described in chapter 4, we can estimate the mean ionization state in the blast wave shell at 3.5. The fourth ionization potential of nitrogen is approximately 75 eV and the average of the third and fourth ionization potentials is thus 61.25 eV. The blast wave radius at 150 ns is 1.25 cm meaning there is $1.3 * 10^{-4}$ g of material swept up by the blast wave or $5.8 * 10^{18}$ atoms and $3.55 * 10^{20}$ eV or 56.9 J of energy necessary to ionize this material to the a mean ionization state of 3.5. This is slightly less but comparable to the lower bound on the radiated energy.

7.2 Effect of Drive Laser on Blast Wave Evolution

We performed experiments designed to build on earlier published experiments at lower energies and to clarify discrepancies between theoretical predictions and experimental observations for the growth rate of the Vishniac overstability. These experiments had two major goals. The first was observing growth of the Vishniac overstability from noise. Based on the observed trajectories shown in Figure 28, we expected the possibility of growth of the overstability over at least the 1st 200 ns for blast waves in xenon. Our second goal was to determine the effect of the drive laser passage on the subsequent evolution of the blast wave it creates. We suspected this was a major cause in a discrepancy between published theory and previous experimental results.

Important early experimental work on the Vishniac overstability was published by Grun *et al.*¹⁶, using the Pharos III laser at the Naval Research Laboratory. They conducted experiments on the evolution of hemispherical blast waves produced in a background gas by single-sided irradiation of a plastic foil by 200J laser pulses. Because of this target geometry the blast waves produced traversed the region of gas affected by the drive laser. Grun *et al.*¹⁶ reported observing the Vishniac overstability grow from noise in blast waves traveling through xenon gas, while those blast waves traveling through nitrogen gas remained stable and the shock front remained smooth. Images from this work can be seen in Figure 35. Whereas theory¹⁸ predicted a maximum growth rate going as $t^{0.7}$ at an ℓ number of ~ 50 for the estimated polytropic index associated with the xenon blast wave, Grun *et al.*¹⁶ observed growth going as $t^{1.6}$ at an ℓ number of ~ 10 .

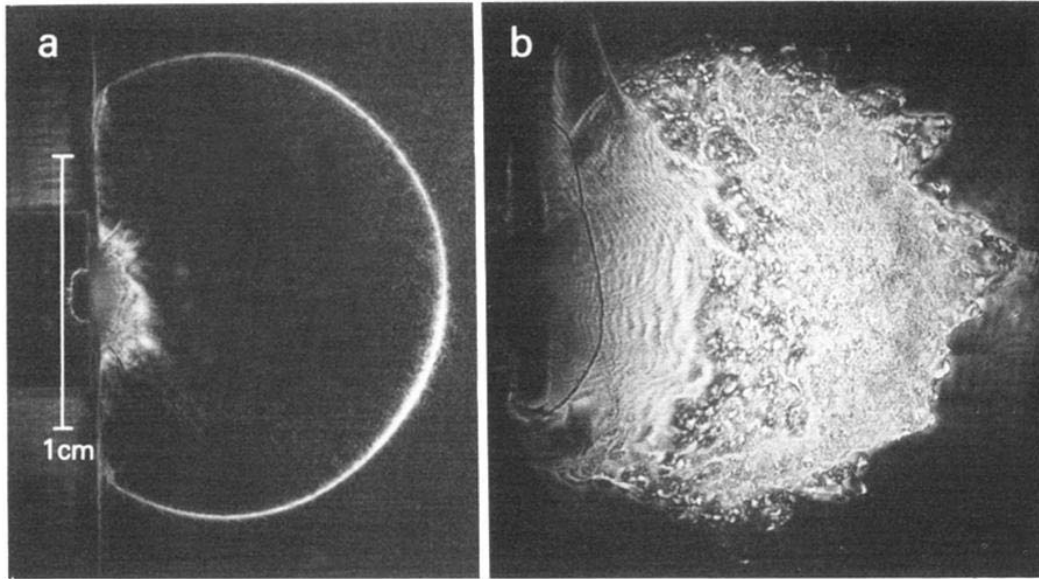


Figure 35. Figure from Grun *et al.* Blast waves produced by 200 J laser pulses incident on flat plastic foils from right of images. Image on the left is of a blast wave traveling through nitrogen, while the blast wave on the right is traveling through xenon. Note both the large feature in the laser focal cone and the small scale structure in the xenon image.

More recent work on blast waves in cylindrical geometry was published by Edwards *et al.*¹⁵. They illuminated a jet of xenon clusters with an ultra-fast laser. This created a cigar shaped filament of exploding clusters which drove a cylindrical blast wave into the surrounding xenon. They observed evidence of the formation of a radiative shock and a slight deviation from a Taylor-Sedov trajectory but did not observe any perturbation growth on the shock front. The authors postulated the primary reason they saw no growth was the Mach number of their blast wave was too low and in addition that the wave was heated by efficient electron conduction between the hot core and the blast wave shell, leading to a higher polytropic index and a thicker blast front.

The Lamming and Grun^{33, 34} simulation discussed in the simulation chapter have clarified the physics involved in the experiments. Their work seemed to confirm Edwards et al.'s theory that the reason for the discrepancy between the two sets of experiments was the low Mach number of the blast waves in that work by showing that there is a velocity cutoff for the overstability to affect blast waves traveling through xenon gas. This cutoff was shown to be around 25 km/s for blast waves traveling in 5 Torr of xenon gas, well above the velocity of the blast waves in Edwards et al¹⁵. However, the analysis performed by Lamming *et al.*^{33, 34} as to the mode number and growth rate predicted maximum growth at a lower rate and higher ℓ number than either what was seen in the Grun et al. experiments or the published theory of Vishniac et al.¹⁹ further emphasizing the need for additional experiments to clarify this discrepancy.

The velocity and temperature of a laser driven blast wave increase with increasing drive energy. For the range of temperatures seen in laboratory experiments (on the order of 1 eV – 10eV) an increase in temperature should lead to an increase in the ionization

state, especially for higher atomic number gasses. This increase in the ionization state should lead to increasing amounts of line and free-bound radiation, increasing the importance of radiation on the hydrodynamics of the blast wave. Therefore by changing the energy of the drive laser used to create our blast waves, we can vary the importance of radiation and isolate features caused by the experimental setup from those caused by radiation. We performed a series of experiments attempting to resolve the discrepancies between previous experiments and published theories. Three different drive laser energies ranging from 10 J to 1000 J were used to create blast waves in 5 Torr or 10 Torr of nitrogen or xenon gas. The use of a pin target (as opposed to the planar foil targets used in Grun's¹⁶ experiment) allowed us to examine the evolution of the blast wave both in the gas previously traversed by the laser on the front side of the pin and in the pristine gas on the back side of the pin. For these experiments the Schlieren diagnostic was used to examine the front morphology of the blast waves as a function of time and position.

Images of shockwaves traveling through 5-10 Torr of Xenon gas are shown on the left side of Figure 36. In all cases the laser pulse came in from the left of the picture. At all energies the blast waves exhibit similar behavior. There is a marked difference between the section of blast wave traveling over the gas region traversed by the laser and the rest of the blast wave. The difference is a turbulent region with a large perturbation that varies in wave number, but is of order 10, on the laser side of the wave that is not present on the back side of the wave. This feature is consistent in wave number with the Grun results¹⁶. It is further interesting to note that in all of our data and the published data of Grun et al. the large scale feature appears to be centered in the laser focal cone. If the feature were associated with the Vishniac overstability, one would expect rippled

features at all points on the spherical blast shell, depending on random noise in the background gas and the initial blast wave. The turbulent feature we see generally becomes increasingly pronounced with increasing energy, but the qualitative behavior is similar. There is also some dependence of the feature on the pin material. The pin material for the 10 J shots was stainless steel, while the 500 J shots employed a copper target and the 1000 J shots were done with nylon targets. The 500 J shot has a particularly wide feature and we suspect this may be due to the radiation from the copper target. A magnified image of the feature for 1000 J drive energy is shown in Figure 37. In contrast to this energy independent feature, there are smaller scale perturbations, closer in wave number to the theoretical maximal growth rate mode number of 50^{18} , that appear only at higher energies. Though it is difficult to measure a growth rate for these perturbations due to their small size, they seem more consistent with theoretical predictions for the Vishniac overstability and are seen both in our higher energy data as seen in Figure 25 and in the data from Grun *et al*¹⁶ as seen in Figure 35.

The xenon images can be contrasted with the images of blast waves traveling through 5-10 Torr nitrogen gas, shown on the right side of the same figure. Again we see blast waves produced by the same three laser drive energies. In this case the feature seen in xenon in the region traversed by the laser is greatly reduced and the small scale perturbations never arise. The fact that a qualitatively energy independent feature is seen only on blast waves traveling through xenon gas and only in the region of the laser cone suggests that there is some effect of the laser's passage on the evolution of blast waves in xenon. This feature is evident on blast waves traveling at velocities both above and

below the theoretical cutoff determined by Lamming et al.^{33,34} and with 1053 nm and 527 nm laser drive pulses.

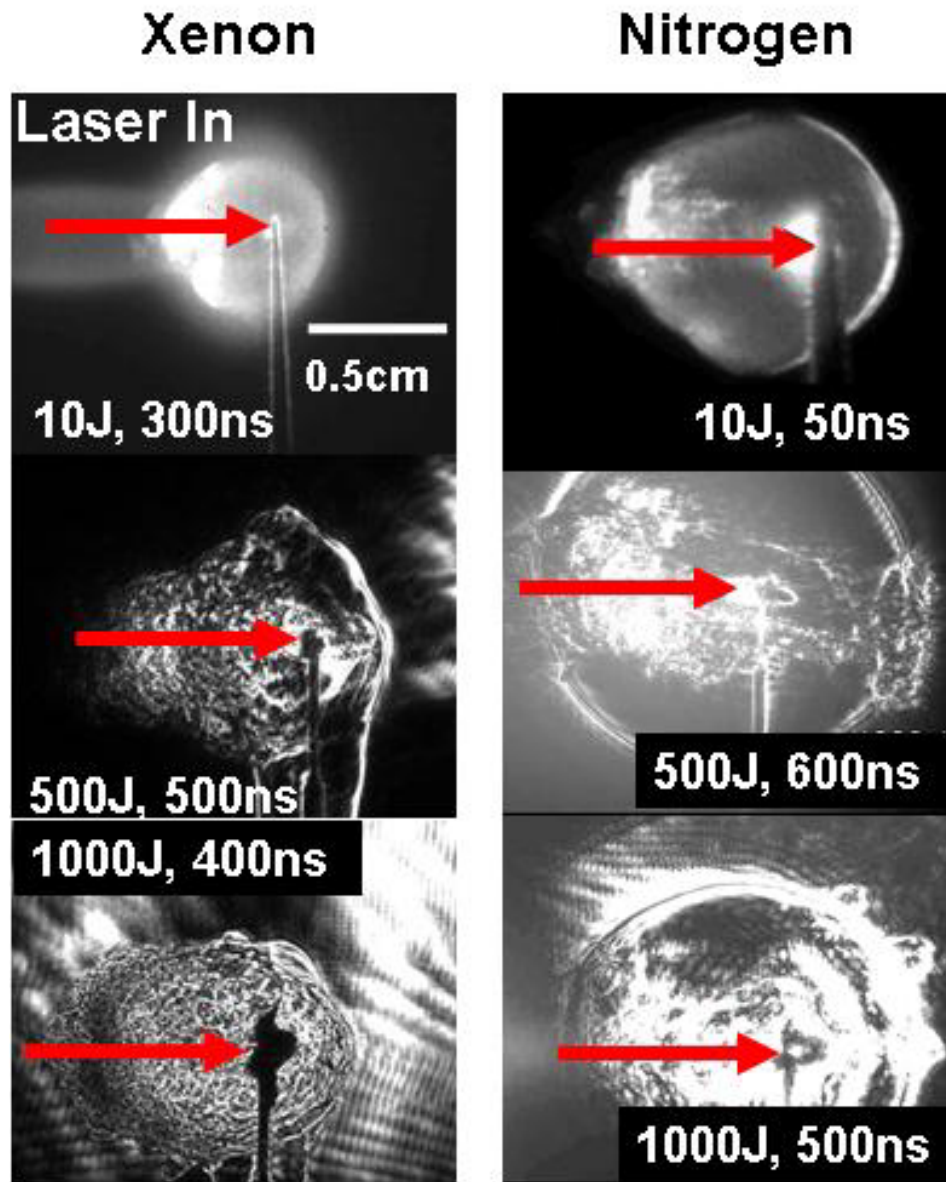


Figure 36. Images of blast waves traveling in xenon (left side) and nitrogen (right) gas at various times. The energy of the drive laser used to produce the blast waves is indicated in each panel.

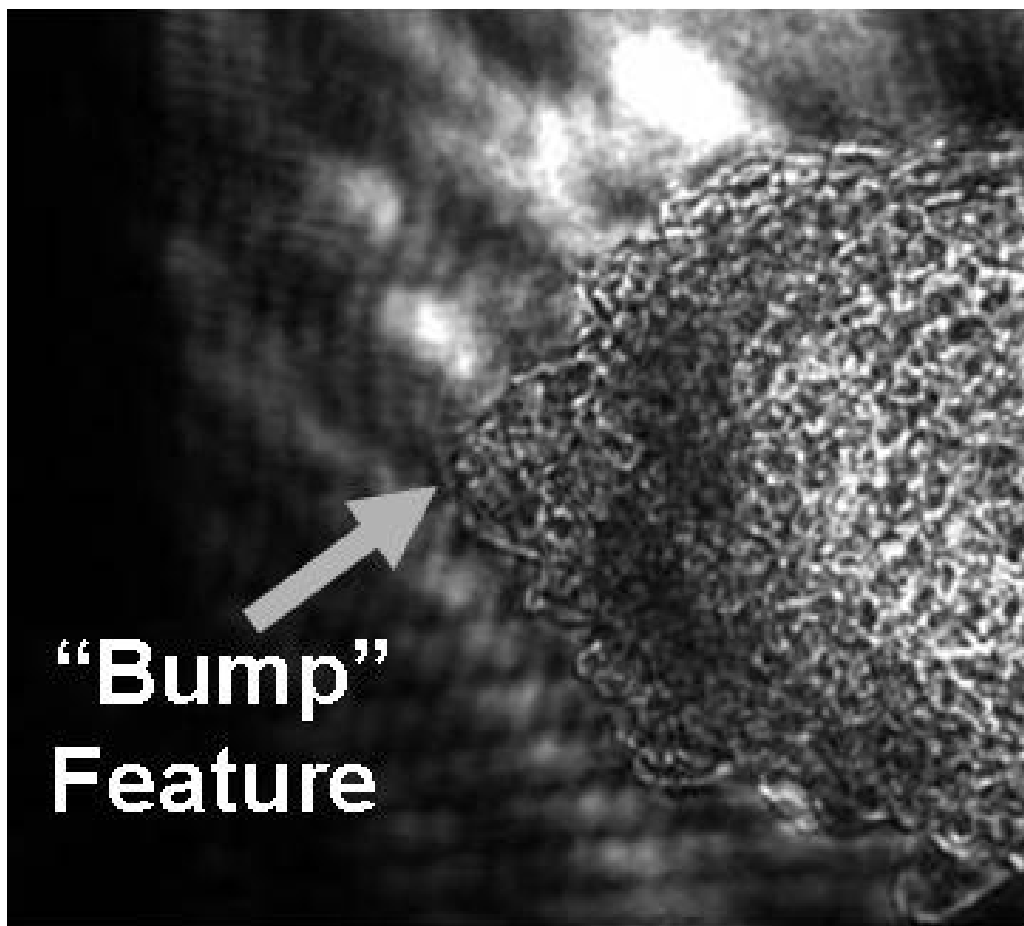


Figure 37. Expanded view of feature on the laser side of a blast wave traveling through xenon. The blast wave was created 400 ns earlier by a 1000 J laser pulse.

We attribute the turbulent feature in Xe to pre-ionization of the gas by the laser. The most likely reason that the feature is seen on blast waves traveling through xenon gas and not on those traveling through nitrogen gas has to do with the different multi-photon ionization thresholds of these gasses. The threshold for multi-photon ionization in xenon is lower than in nitrogen. At a laser wavelength of 527nm ionization is a 5 photon process in xenon, as compared to 7 in nitrogen, and the ratio increases for higher charge states. This means that there is likely more ionization and heating of the xenon gas

caused by the laser's passage, creating a low gas density region. Therefore, the blast wave traveling over this area will pick up gas that is lower density and hotter than in other regions, causing it to slow down less as it travels, creating the bump like feature seen. Several facts support the idea that the feature is caused by the laser's passage. As previously mentioned, in both our results and those of Grun *et al*¹⁶ the feature appears only in the laser cone path, as is illustrated in the 1st panel of Figure 36. The feature also appears independent of the blast wave velocity. In our shots the average velocity at early times (between 50 ns and 100 ns) ranges from ~12 km/s for 10J shots, below the 25 km/s threshold predicted for the onset of the overstability in xenon gas predicted by Lamming^{33, 34}, to ~140 km/s for the 1000J shots, above this threshold.

Simulations were performed that support and further clarify the conclusions suggested by the data. 2D simulations of blast wave evolution were performed using the Lawrence Livermore National Laboratory code CALE⁴². CALE is a 2-D arbitrary Lagrangian Eulerian (ALE) code with a tabular equation of state (EOS) and interface tracking. For our simulations ~7.5 Torr of xenon gas was assumed for the initial background. A 0.5mm Mo sphere was used as the target and the laser pulse was 100J in 5ns, with a 0.4mm focal spot size. Some results from the simulation are shown in Figure 38. The first panel of the figure shows a contour plot of the electron temperature 17ns after the initial laser pulse. One can clearly see the hot plasma in the region of the laser cone. The third panel of the figure shows simulated density gradients of a blast wave traveling through 7.5 Torr of Xenon gas about 400 ns after the 100J drive beam struck the target. The second panel shows experimental data taken at $t = 300\text{ns}$ and 10J drive. There is a strong similarity between the experimental result and the simulation. The large

perturbation on the blast wave's surface in the simulation is qualitatively similar to that seen in all our xenon experimental results and to that seen in previous experiments.

While the large perturbation on the blast wave surface does show up, the smaller scale structure seen on the blast waves in xenon produced by high energy shots is absent. This is most likely due to inadequate resolution of the experiments. The simulation uses 4 degree angular zoning which is adequate to start to see the affects of the laser channel on the evolving blast-wave, but is much too coarse to resolve the small scale "turbulent" features seen in the experiment. These small scale features, which are almost certainly three dimensional, evidently evolve differently in the case of Xe, and may be indicative of the higher compressibility of Xe through ionization and or radiative effects. The results from this section are summarized in a paper we have published⁴³.

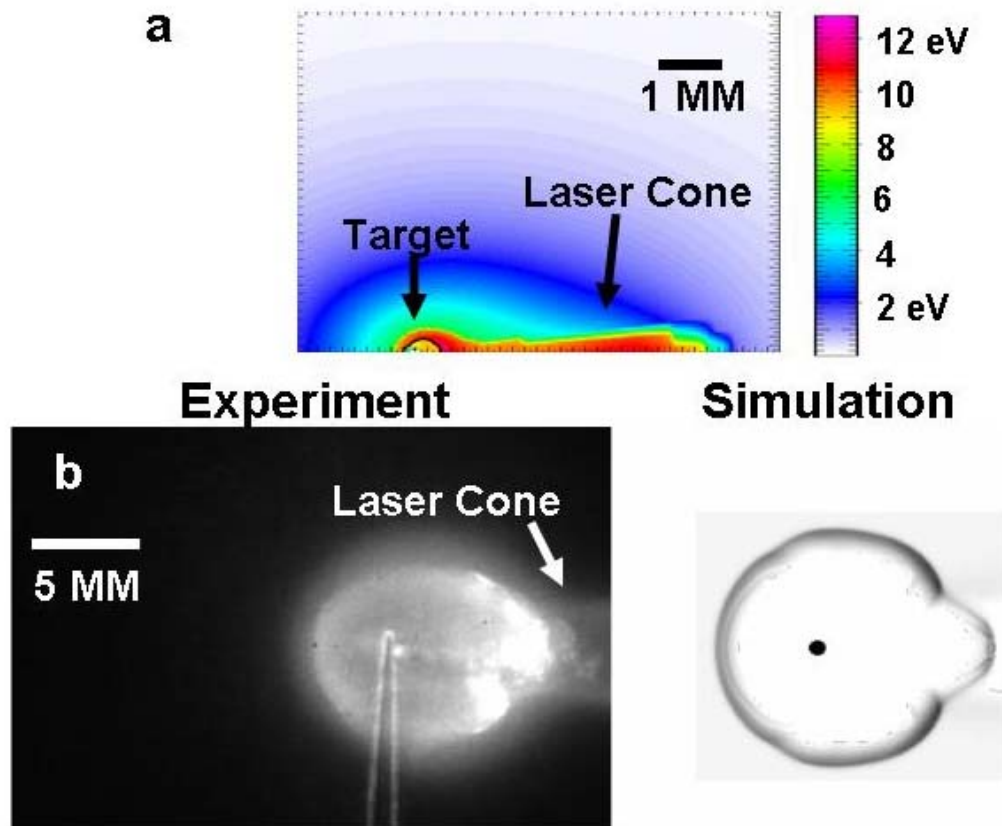


Figure 38. Results from simulations performed to ascertain the role of the passage of a drive laser beam on the subsequent evolution of the blast wave it creates. Panel a shows CALE simulations demonstrating the creation of a heated region of gas in the laser cone. Panel b shows experimental data taken 300 ns after a 10 J laser pulse created a blast wave. Panel c shows a simulated blast wave 400 ns after being created by a 100 J laser pulse.

7.3 Evolution of Induced Perturbations on Blast Waves

The small scale ripples seen in the experiments described in the previous section that may be caused by the Vishniac overstability do not grow to a large enough amplitude for a growth rate to be accurately measured. In order to sidestep this problem our next set of experiments attempted to shortcut the growth process by inducing perturbations on the surface of a blast wave. The published theory for perturbations on high Mach number blast waves¹⁷⁻¹⁹ shows that the evolution these perturbations depend primarily on two variables: the mode number of the perturbation and the polytropic index of the medium the blast wave is traveling through. Regularly spaced wire arrays were placed in the path of the blast waves in order to induce perturbations with a known primary mode number. The primary mode number of the perturbations could be varied by altering the spacing of the wire arrays. The polytropic index of a gas will vary with the importance of radiation, which is dependant on the choice of background gas. Several background gasses were employed to examine the effect of radiation on the evolution of the perturbations. By altering these two parameters and tracking induced perturbations as a function of time, we were able to make quantitative comparisons to the published theory¹⁹.

Experiments were performed on blast waves traveling in helium, nitrogen, and xenon gases as well as a mixture of xenon and nitrogen. For each gas several different wire spacings were used to induce differing primary frequency perturbations on the blast waves. Two different types of arrays described in chapter 5 were used during the course of the experiments, a planar array and a cylindrical one. For a given gas only one type of array was used. A series of shots were fired with different delays between the drive and

probe beams for each array and gas combination employed. This produced a series of images that could be examined to provide comparison to the theoretical predictions for the Vishniac overstability.

7.3.1 Planar Wire Array

For experiments in nitrogen and xenon gas, the planar wire array was used. Using spatial calibration of the imaging system it was determined that the array was placed just under 9mm from the focus of the drive laser beam. This lead to a circumference of ~55 mm for the blast wave at the point it intersected the array. The array was strung with the wires spaced 2 mm, 4 mm, and 6 mm apart to correspond to mode numbers of 28, 14, and 9 respectively. The mode content of the induced perturbations was complicated by several factors. The 1st was an ellipticity to the blast wave that added a low mode number perturbation to the blast wave. Another major source of modal content was the use of a planar array. The use of a planar array meant that the blast wave was at slightly different radii when each wire was encountered. This broadens the range of mode numbers in the induced perturbation. In addition, the use of a planar array limited the solid angle of the blast wave that the wire array intersected. This both added modal content to the induced perturbation and limited the modal resolution of Fourier transforms performed on the data.

A series of images for blast waves produced in nitrogen passing past the three differently spaced arrays were taken. Figure 39 shows the evolution of blast waves past the 2 mm spaced (mode number 28) array. Figure 40 shows the results for the 4 mm

(mode number 14) array and the results for the 6mm spaced (mode number 9) wire array are shown in Figure 41. As expected from the nitrogen trajectory information described in section 7.1, blast waves produced in nitrogen do not have the right conditions for growth of the Vishniac overstability. The perturbations induced by the wire array diminish with time.

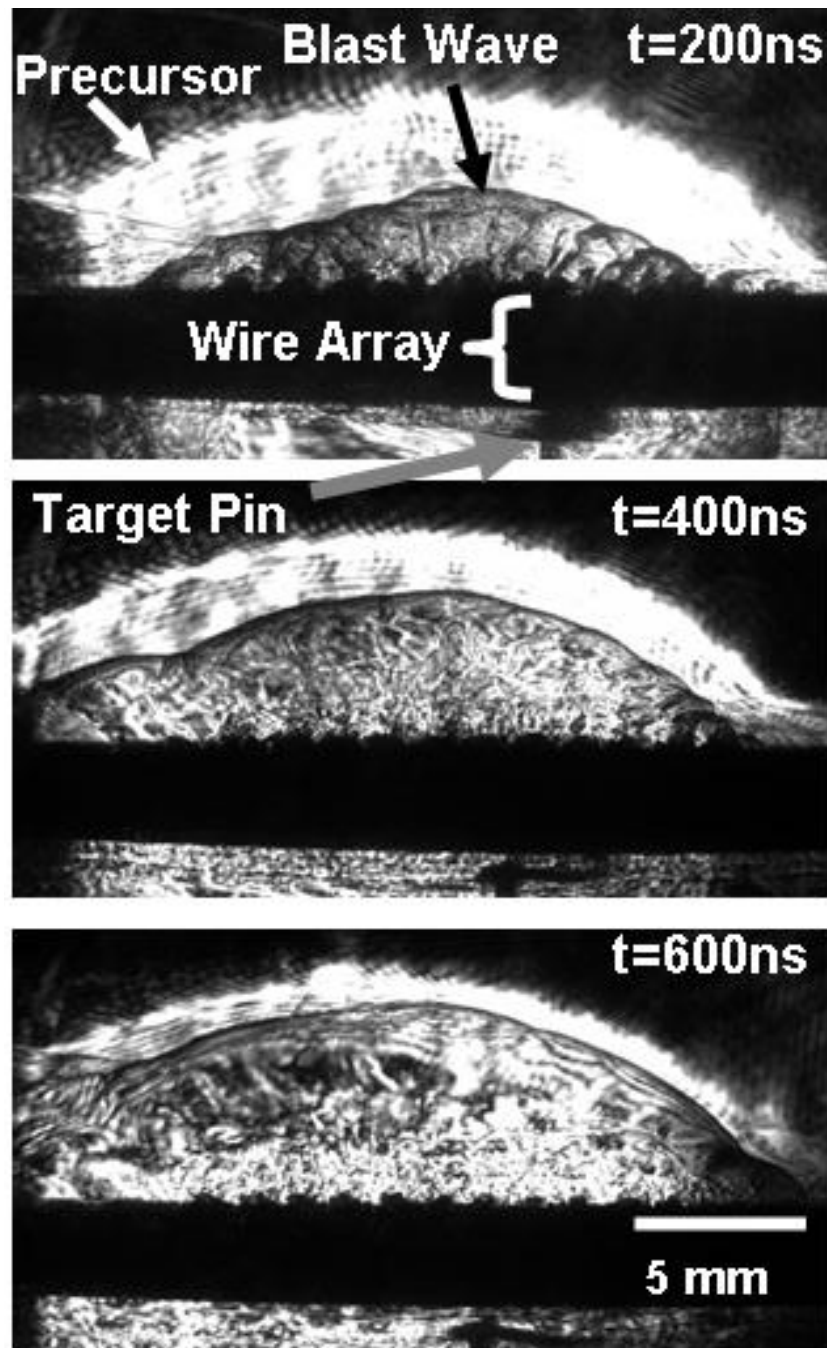


Figure 39. Time series of images of blast waves traveling in 10 Torr of nitrogen gas past a 2 mm spaced wire array. Blast waves were created by a 1000 J laser pulse. Induced perturbations decay with time as is expected in nitrogen.

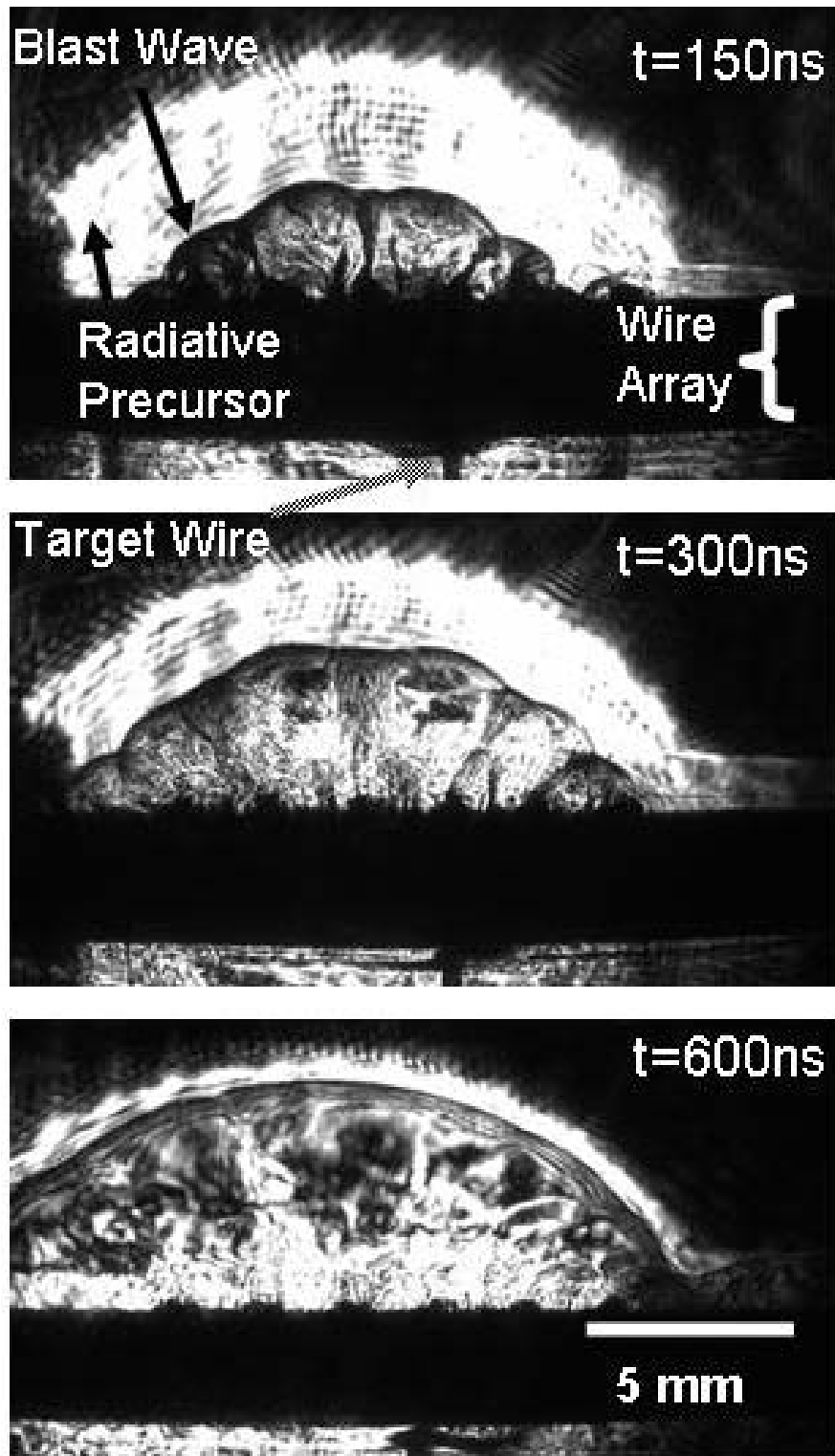


Figure 40. Time series of images of blast waves traveling in 10 Torr nitrogen gas past a 4 mm spaced wire array. Blast waves were created by a 1000 J laser pulse. Induced perturbations decay with time as is expected in nitrogen.

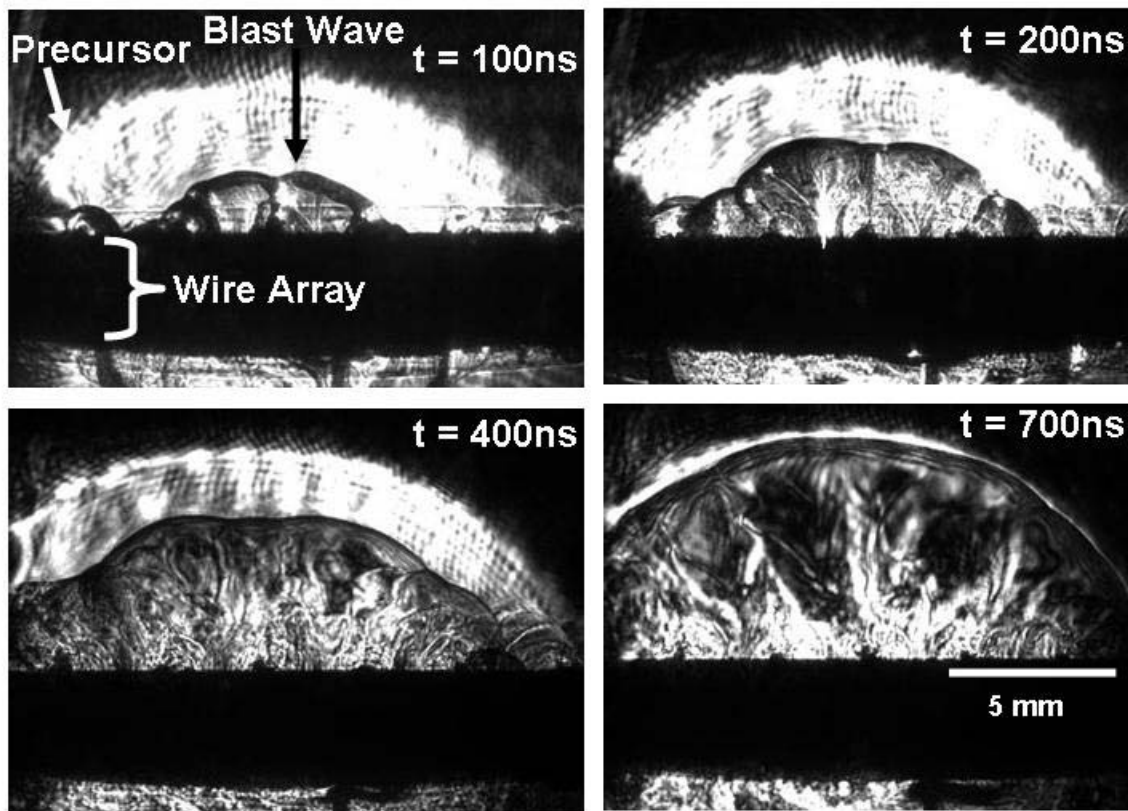


Figure 41. Images of blast waves traveling in nitrogen created by 1000 J laser pulse. The blast waves are traveling past a 6mm spaced wire array. Perturbations induced by the array decay with time, as expected for blast waves in nitrogen.

A similar series of images was taken for blast waves produced in xenon gas. Images for the 2 mm spaced (mode number 28) wire array are shown in Figure 42. Figure 43 shows images of the evolution past a 4 mm spaced (mode number 14) array and Figure 44 shows similar images for the 6mm spaced (mode number 9) array. However, the strong radiation from these blast waves produced effects that made analysis difficult. As mentioned previously, the radiation from the blast waves in xenon ablated material in the arrays, creating additional blast waves. These additional blast waves

made it difficult to measure the main blast wave until it was outside the field of view of the diagnostics and the perturbations had significantly died away.

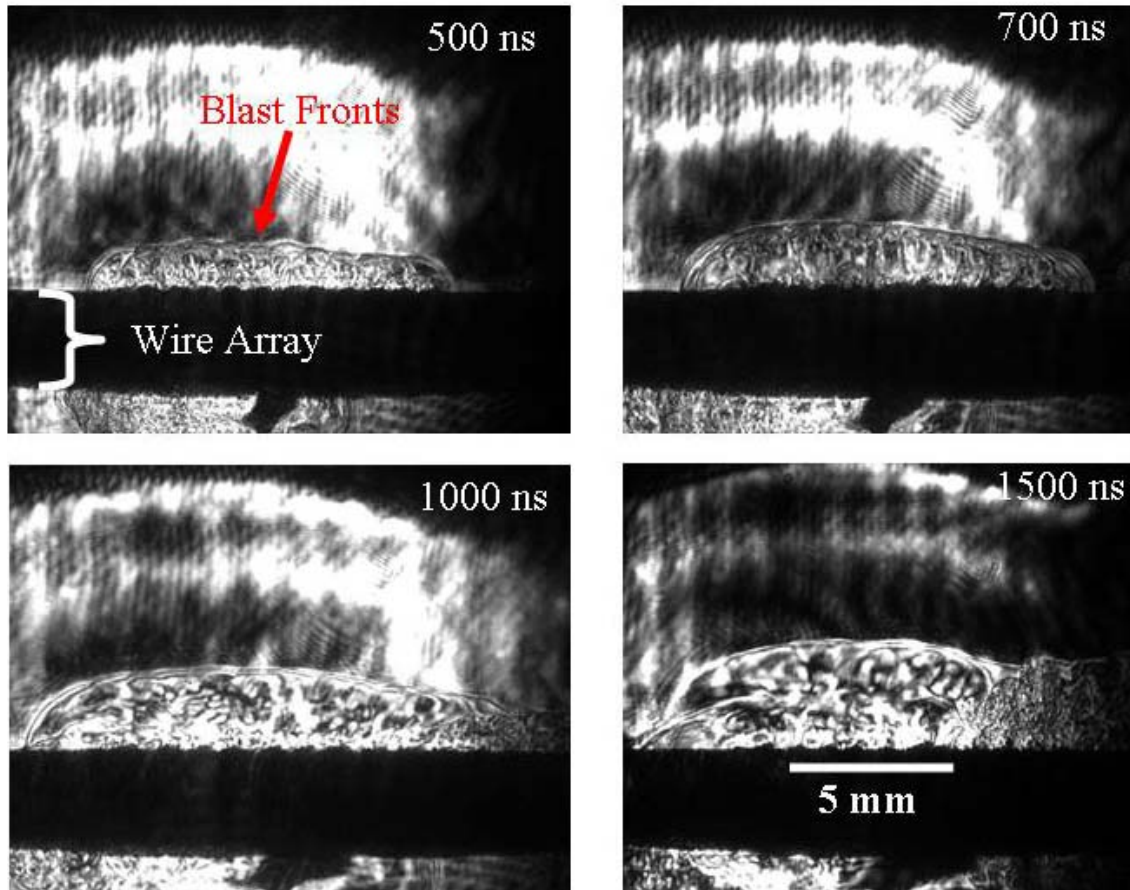


Figure 42. Time series of images of blast waves traveling in 10 Torr xenon gas past a 2 mm spaced wire array. Blast waves were produced by 1000 J laser pulses. The radiation from the main blast wave has ablated material from the wires in the array, creating additional blast waves that interfere with measurement of the main wave.

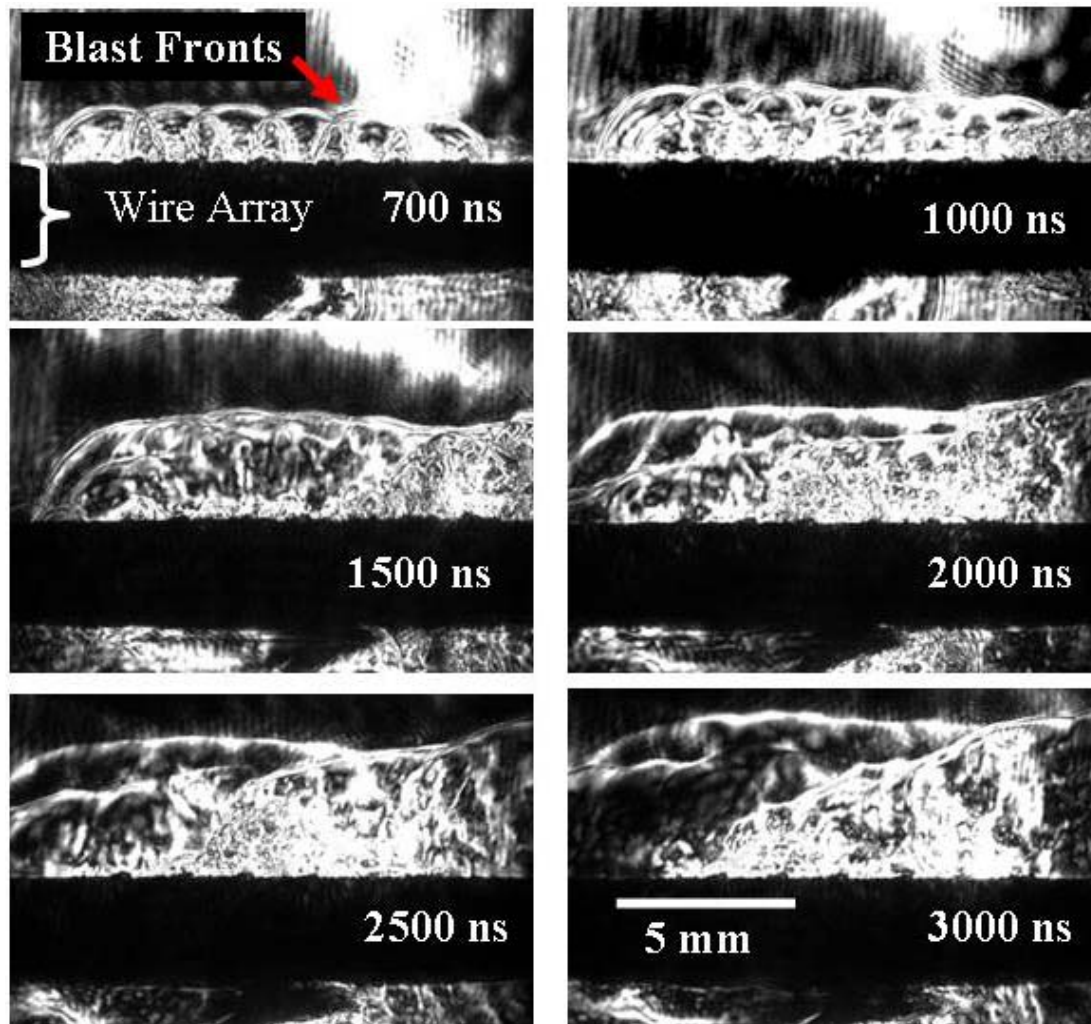


Figure 43. Time series of images of blast waves in 10 Torr of xenon traveling through a 4mm spaced wire array. The blast waves were created by a 1000 J laser pulse. Radiation from the main blast wave ablates the wires in the array creating additional blast waves that obscure the main blast wave.

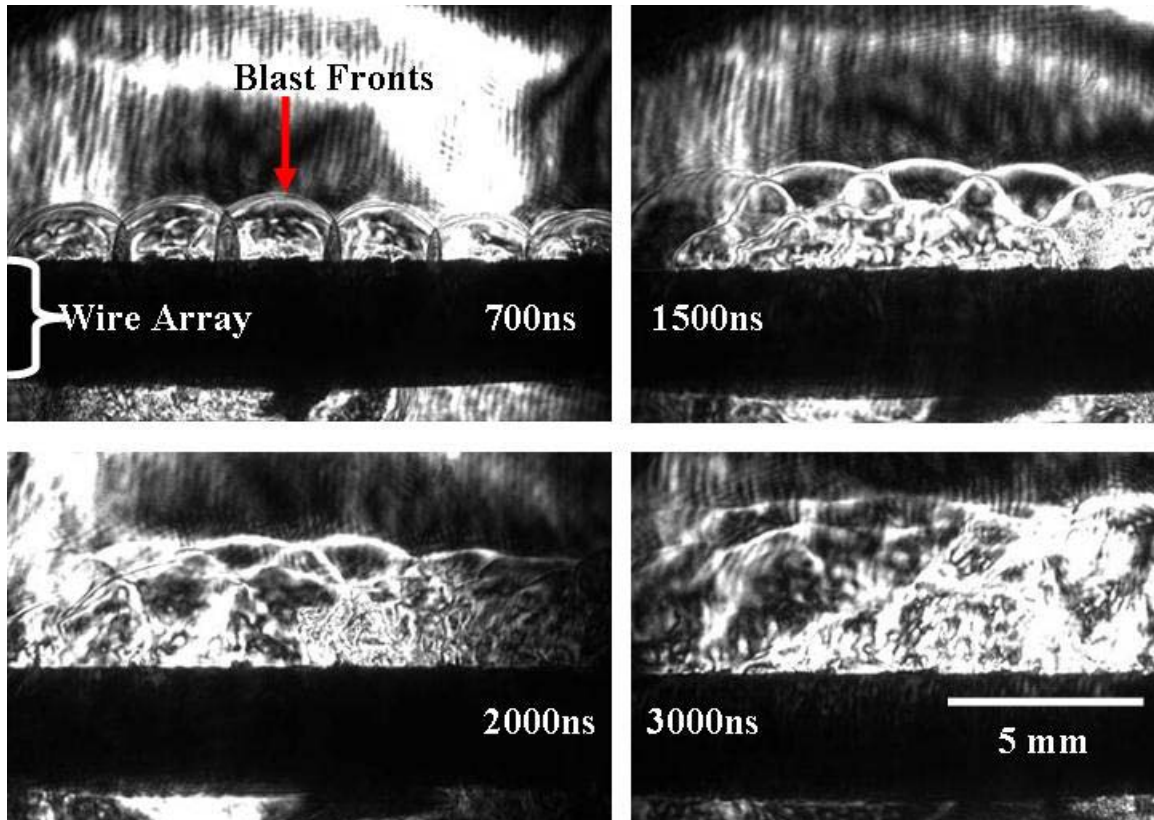


Figure 44. Images of blast waves in xenon traveling past a 6mm spaced wire array. Blast waves were created by 1000 J laser pulses. Radiation from the main blast wave irradiates the wires in the array, ablating material and creating additional blast waves that obscure the main blast wave.

7.3.2 Cylindrical Wire Array

In order to limit the modal content of the induced perturbations on the blast waves the half-cylindrical wire array was used for later experiments in helium and for a mixture of nitrogen and xenon. This array was placed approximately 8-9 mm from the drive laser focus with the placement varying slightly for the different gasses. The wires were spaced 2 mm, 3 mm, and 4 mm apart corresponding to mode numbers ranging from 12 to 30 depending on the gas and wire spacing. This array somewhat limited the added modal content from the shape of the array, however it was still of finite angular size and did not correct the ellipticity of the blast wave. In fact, this array may have created some

ellipticity with the vertical axis being the longer one. Figure 45 shows images of blast waves in helium traveling past a 4mm spaced (mode number 12.2) half-cylindrical wire array. A series of images of blast waves in helium traveling past a 3mm spaced (mode number 16.3) half-cylindrical wire array is shown in Figure 46 and Figure 47 shows similar images for the 2mm spaced (mode number 24.4) array. Because of its small atomic number and high ionization potential (24.6 eV for the 1st ionization potential of helium as opposed to 14.5 eV for nitrogen and 12.1 eV for xenon) radiation is expected to play little or no role for blast waves in helium.

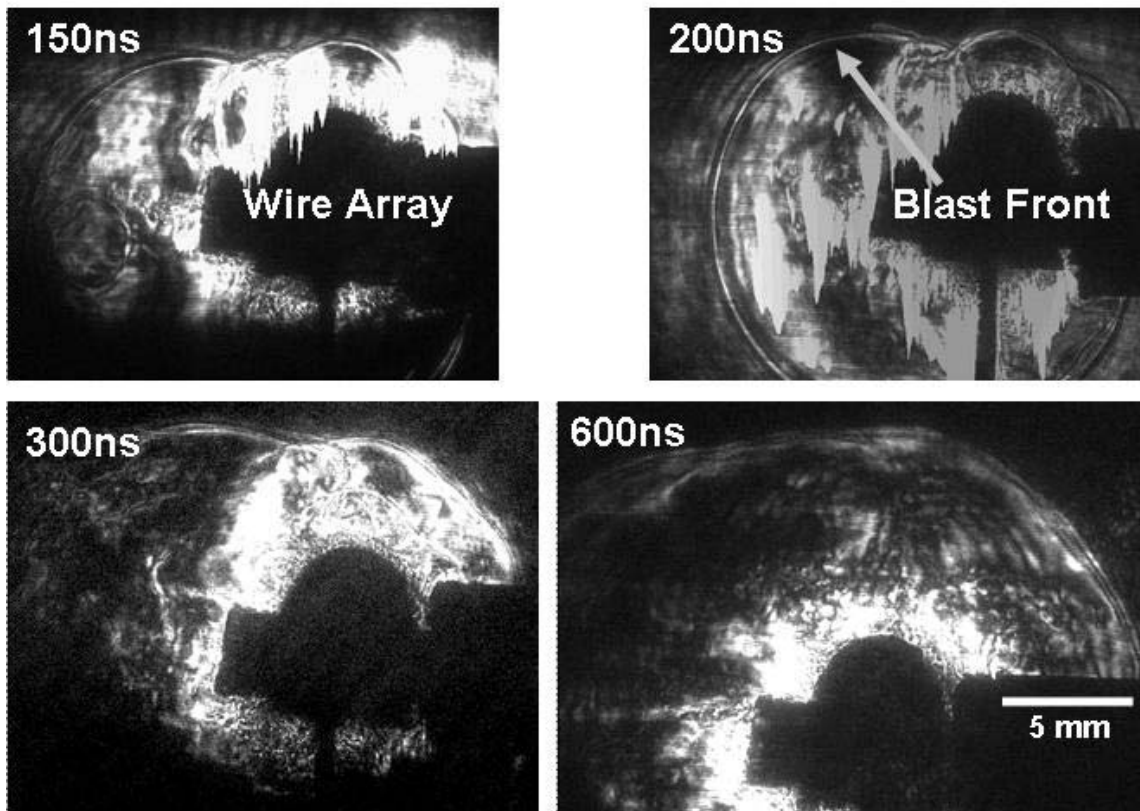


Figure 45. Images of blast waves in helium gas traveling past a 4mm spaced wire array. The blast waves were created by 1000 J laser pulses.

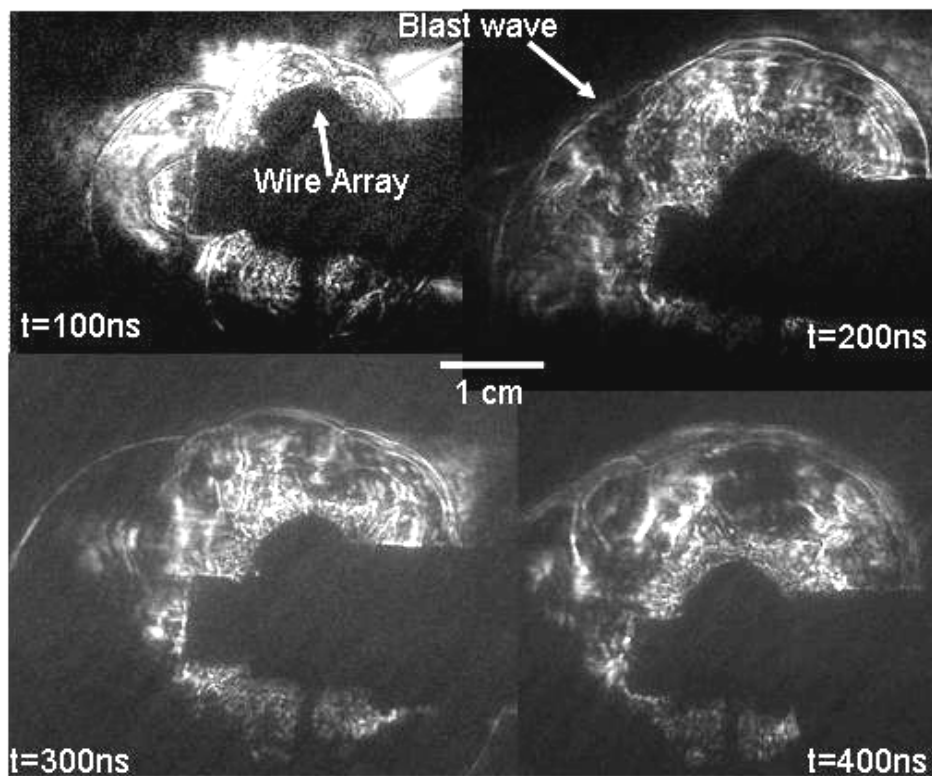


Figure 46. Images of blast waves in helium produced by 1000 J laser pulses. The images were captured with various delays to the drive laser beam as indicated. The blast waves are traveling past a 3 mm spaced wire array. The induced perturbations decay with time as expected.

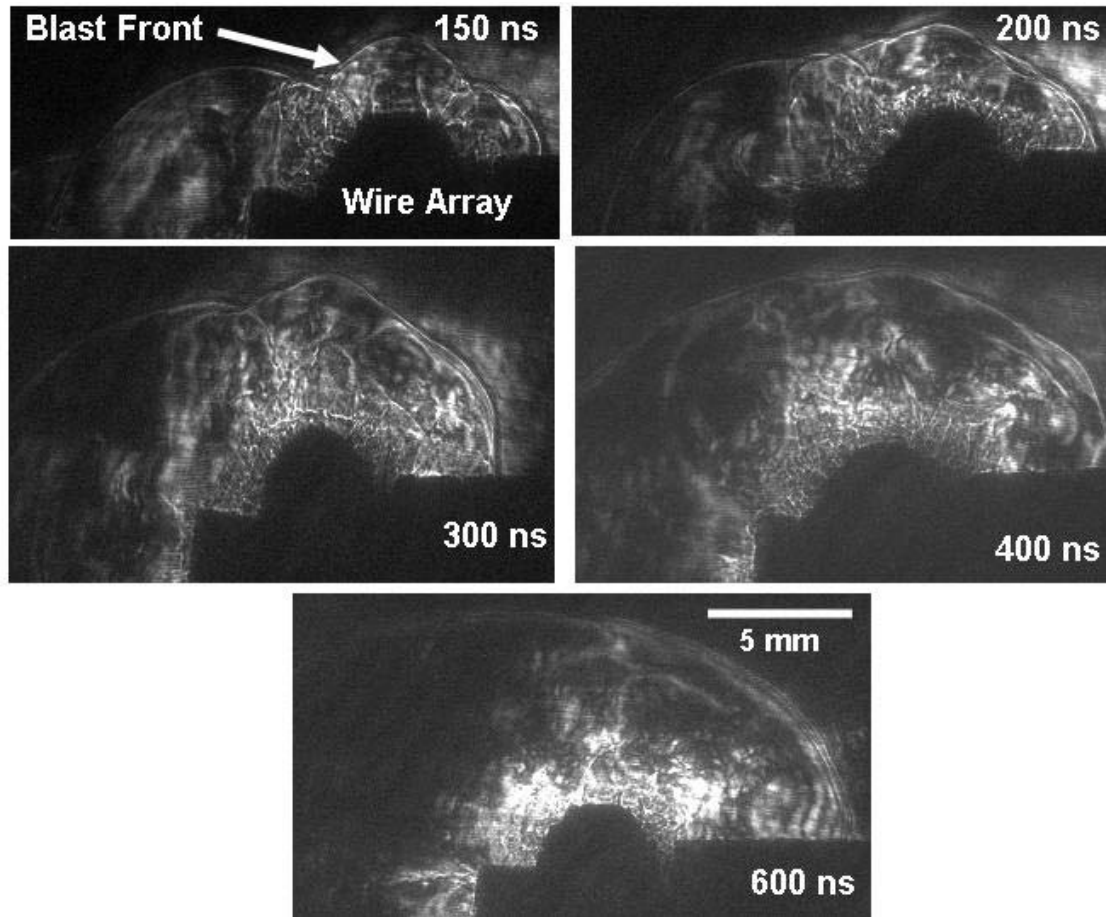


Figure 47. Images of blast waves in 10 Torr Helium gas traveling past a 2mm spaced wire array. Blast waves were created by 1000 J laser pulses

For shots in the mixed gas the evolution is more complicated. Images for blast waves in the mixed gas traveling past a 3mm spaced (mode number 20) cylindrical wire array are shown in Figure 48. The main blast wave is slightly obscured by additional blast waves, but can be discerned and analyzed. The same problems can be seen in the images for blast waves traveling past a 2 mm spaced (mode number 30) wire array seen in Figure 49 and the 4mm spaced (mode number 15) wire array seen in Figure 50.

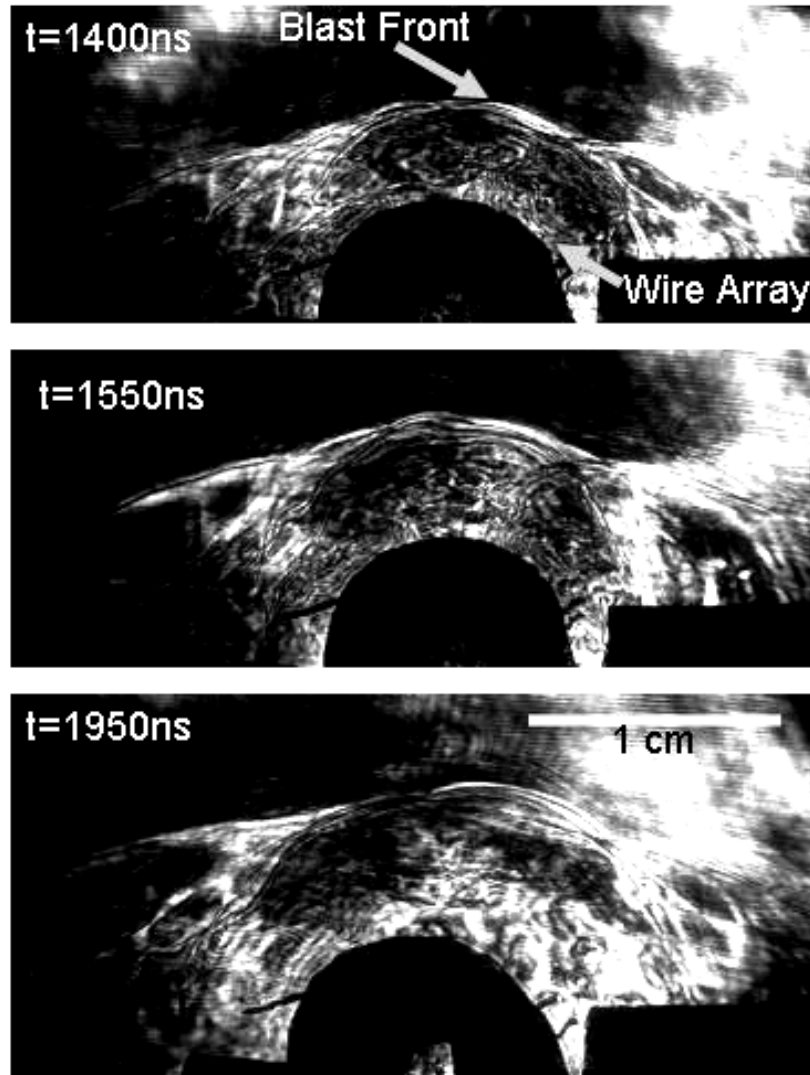


Figure 48. Images of blast waves in a mixed gas produced by 1000 J laser pulses. The images were captured with various delays relative to the drive beam as indicated. The blast waves are traveling past a 3mm spaced wire array.

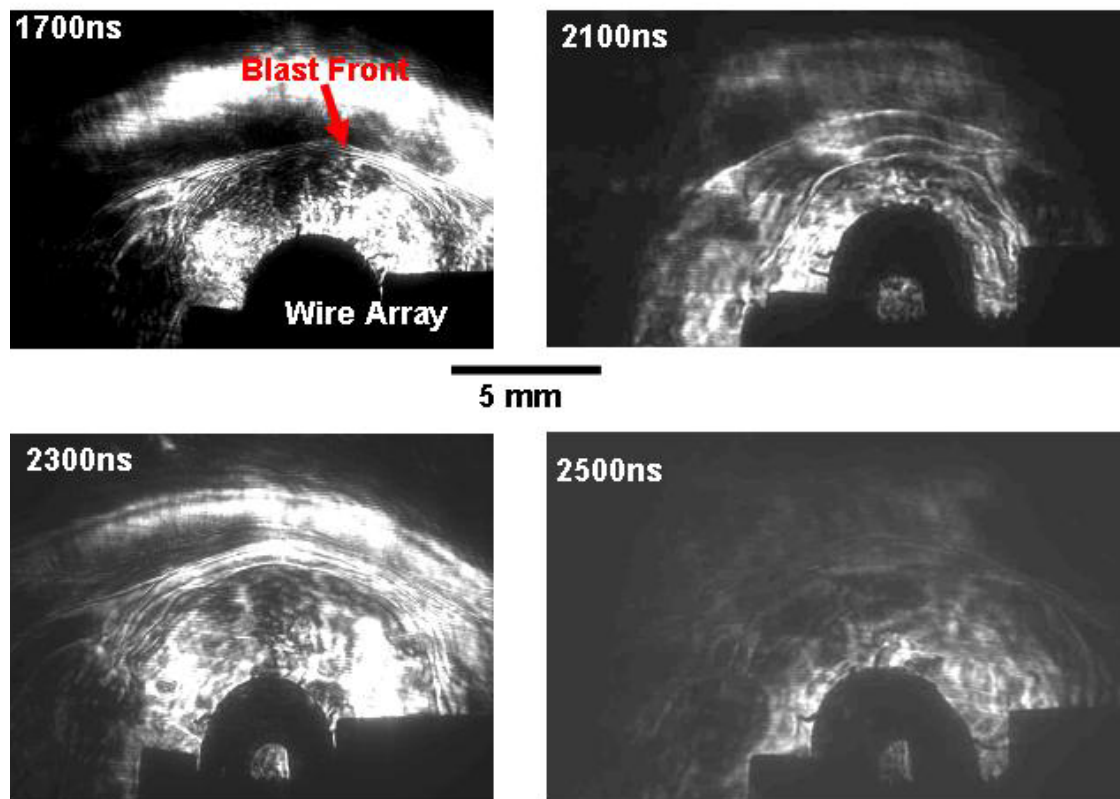


Figure 49. Images of blast waves in a mixed gas produced by 1000 J laser pulses. The images were captured with various delays relative to the drive beam as indicated. The blast waves are traveling past a 2 mm spaced wire array.

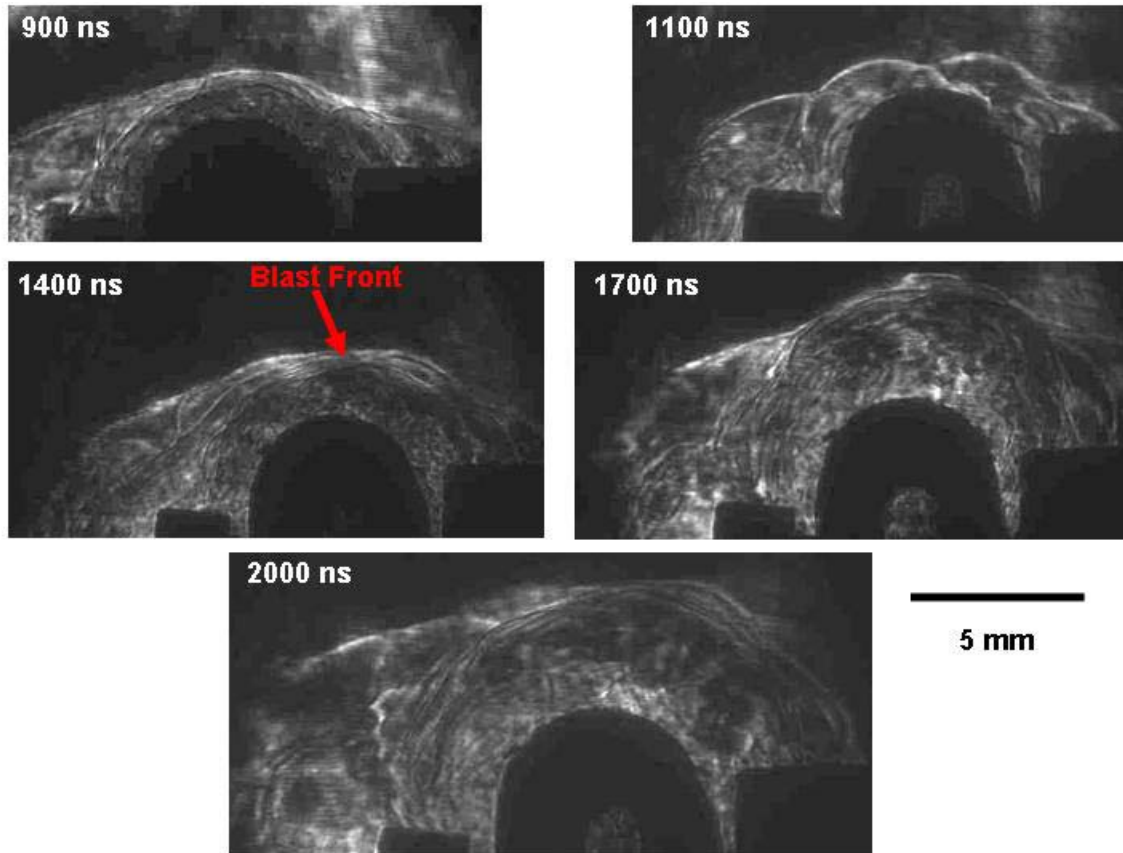


Figure 50. Images of blast waves in a mixed gas produced by 1000 J laser pulses. The images were captured with various delays relative to the drive beam as indicated. The blast waves are traveling past a 4 mm spaced wire array.

7.3.3 Analysis Method

For each image taken the edge of the blast wave was traced out by hand. The center of the blast wave was then estimated from the image by finding the edges of the blast wave and taking the mid point of each axis when possible. However, sometimes one edge of the blast wave was either not on screen or not discernable. In these cases a bit of curve was used to discern the center. Either two vertical position values at one horizontal position or two horizontal positions at one vertical position were measured and averaged to find the center. Using this center, the trace of the blast wave edge was then

transformed to polar coordinates. A sample plot of this for a blast wave in nitrogen traveling past a 6 mm spaced wire array is seen in Figure 51. This graph was then interpolated to provide even spacing between data points. The mean radius of the blast wave was determined from the resulting graph and subtracted from the data. In addition, the angular position was normalized to fractions of a circle so that frequency of any perturbation in the graph would correspond to its mode number. A sample of the result of this transformation for the graph shown in Figure 51 is seen in Figure 52.

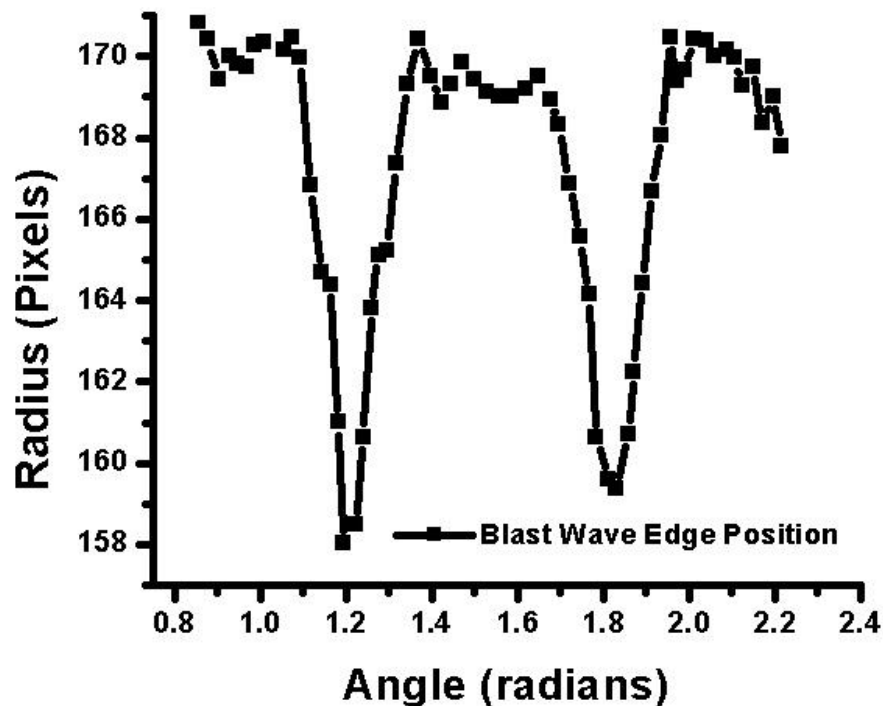


Figure 51. Sample plot of blast wave edge transformed to polar coordinates. This is a plot of the edge of a blast wave traveling through nitrogen after passing a 6mm spaced wire array. The effect of the wires is quite noticeable.

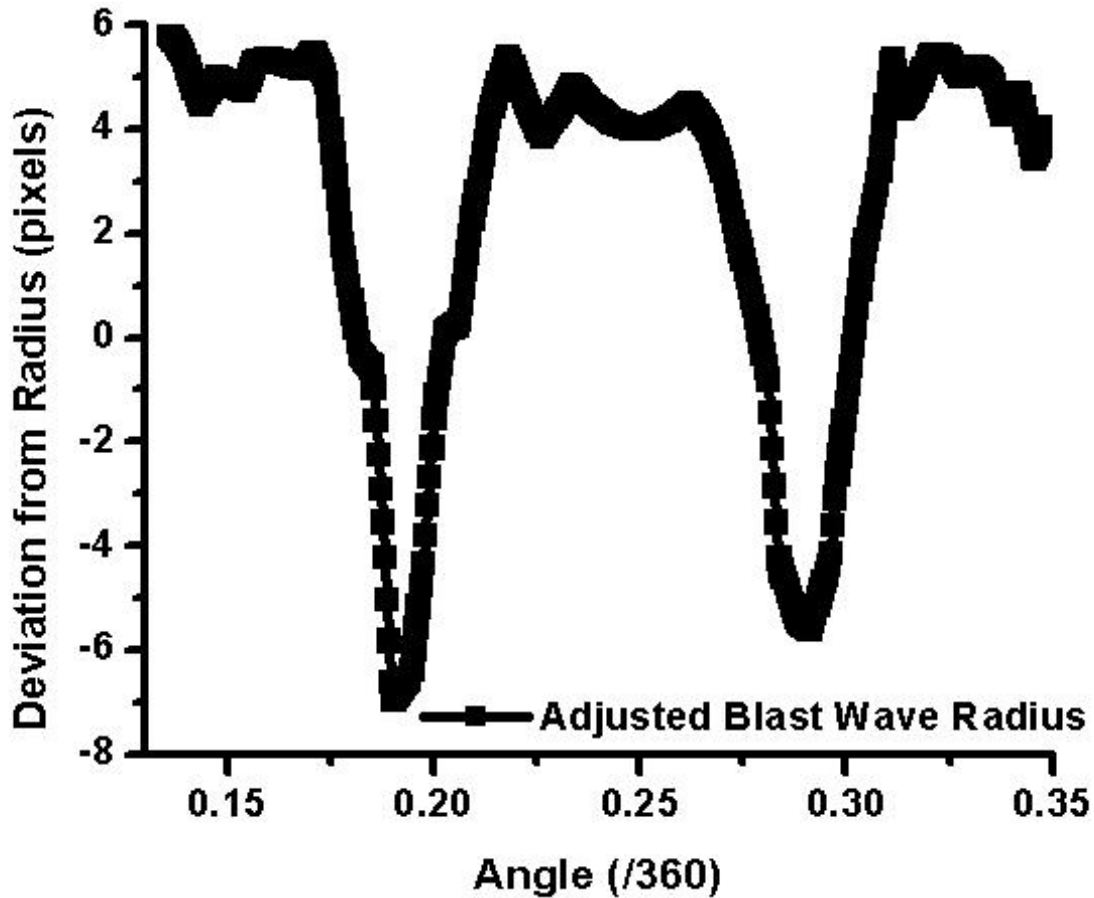


Figure 52. Sample plot of blast wave deviation from mean radius as a function of angular fraction of a circle. Data is from a blast wave traveling through nitrogen and passing a 6 mm spaced wire array.

The data for the radial deviation from the mean radius versus angle in fractions of a circle was Fourier transformed to isolate the mode number corresponding to the wire array spacing. This allowed us to limit the effect of the modal content induced by the limitations of the wire arrays and the low mode number ellipticity, by only looking at the amplitude of one mode number. The Fourier transform of the data in Figure 52 is shown in Figure 53. The amplitude of the desired mode number is then plotted as a fraction of the mean radius of the blast wave and this value is graphed as a function of time for each wire array. The error in the amplitude is set as a one pixel error divided by the square root of the number of wavelengths of the perturbation measured in the image. For

example, for a mode number 24 perturbation on which one quarter of the circumference of the blast wave is seen as usable data in an image, the error in the amplitude is set at one pixel divided by the square root of six (one quarter of the circumference times 24 wavelengths per circumference). This error is then normalized to the mean radius with the amplitude.

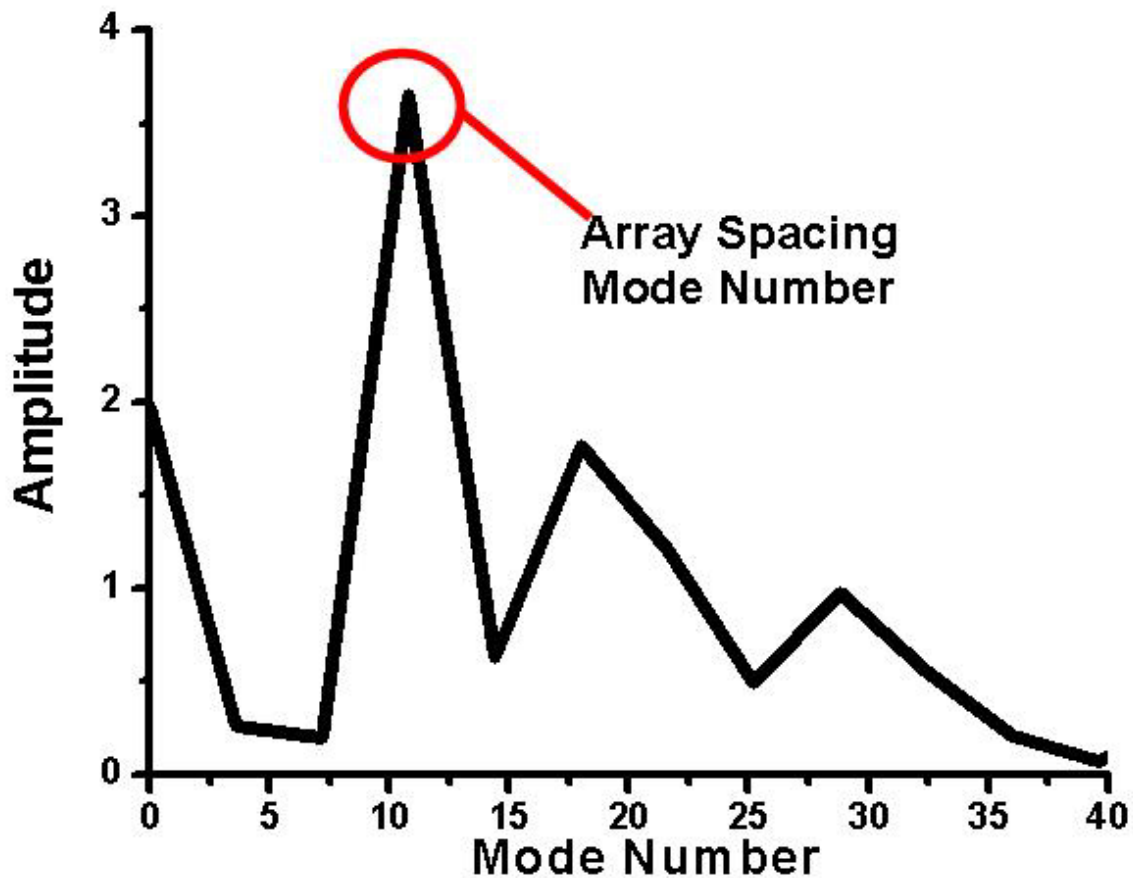


Figure 53. Sample plot of the Fourier transform of perturbation position data. The data is from a blast wave traveling in nitrogen and passing a 6 mm spaced wire array. The mode number corresponding to the wire array spacing at the point the blast wave intersects the array is highlighted.

The evolution of the normalized amplitude was fit to a power law in time to determine the exponent. This experimentally derived exponent could then be compared

to theoretical predictions. The data for blast waves in nitrogen gas traveling past a 6 mm spaced wire array is seen in Figure 54. A similar plot for blast waves in the mixed gas is shown in Figure 55. It is worth noting that all the points in this graph are consistent with the same value meaning that this data does not rule out the possibility of no growth or even a slow decay of the blast wave. However, the fact that the points fit the power law well inside the error bars may mean that the estimated error is too large and that the suggestion of growth is stronger than the error bars would lead one to believe. This idea is represented by the least squares fit error that is used to determine the error bars for the growth rate comparison to theory that will be discussed later.

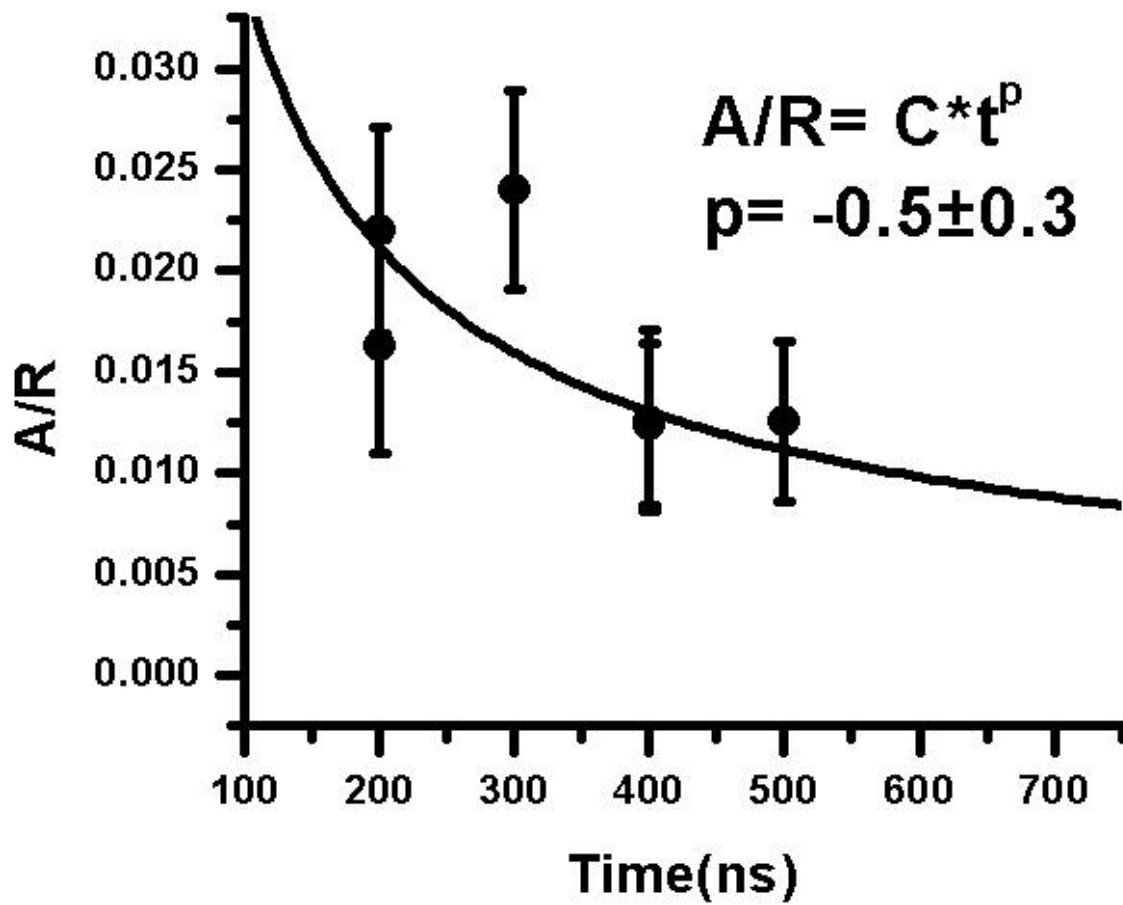


Figure 54. Plot of the amplitude of the induced perturbation mode number as a fraction of the mean blast radius versus time for blast waves in nitrogen traveling past a 6 mm wire array. The data is fit to a power law in time to compare to theory.

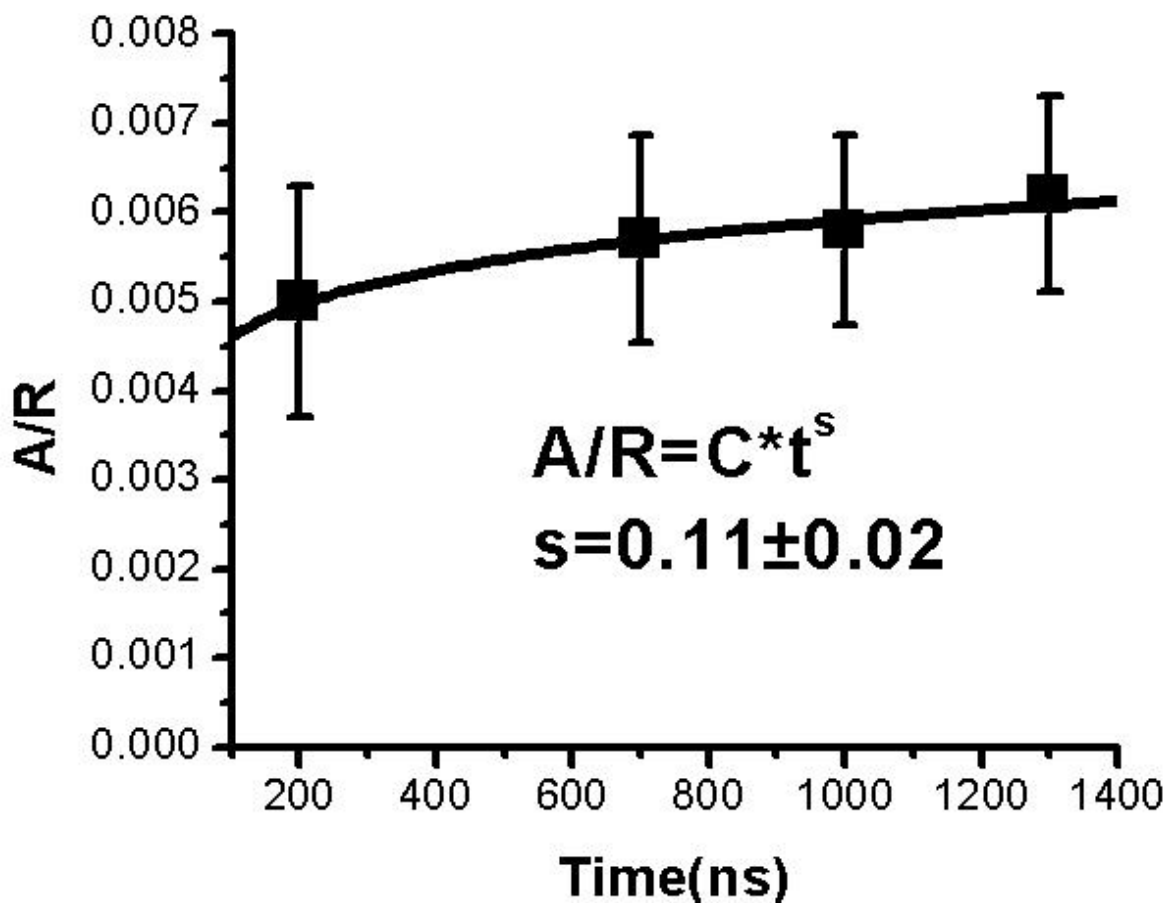


Figure 55. Plot of the amplitude of the induced perturbation mode number as a fraction of the mean blast radius versus time for blast waves in a 7.5 Torr Xe/2.5 Torr N₂ mixed gas traveling past a 4 mm spaced wire array. The data is fit to a power law in time to compare to theory.

The data taken on the cylindrical array was particularly difficult to analyze and a sample Fourier transform plot is seen in Figure 56 for helium gas and Figure 57 for the mixed gas. There are no peaks corresponding to the wire array spacing induced mode number. However, it was discovered that we could still take the amplitude at this mode number and plot it. It was important to get the same mode number on all arrays and the resolution of the Fourier transform was somewhat coarse. To overcome this, we interpolated between points to get the amplitude of the exact mode number we were interested in. This yielded a relatively smooth curve to fit a temporal power law. The

results of this method yielded a very close agreement between theory and experiment for the helium data as will be discussed in the next section which gave us some confidence it could be employed for the mixed gas data. However, the difficulty with this data means there is a low signal to noise ratio and the results must be treated with caution.

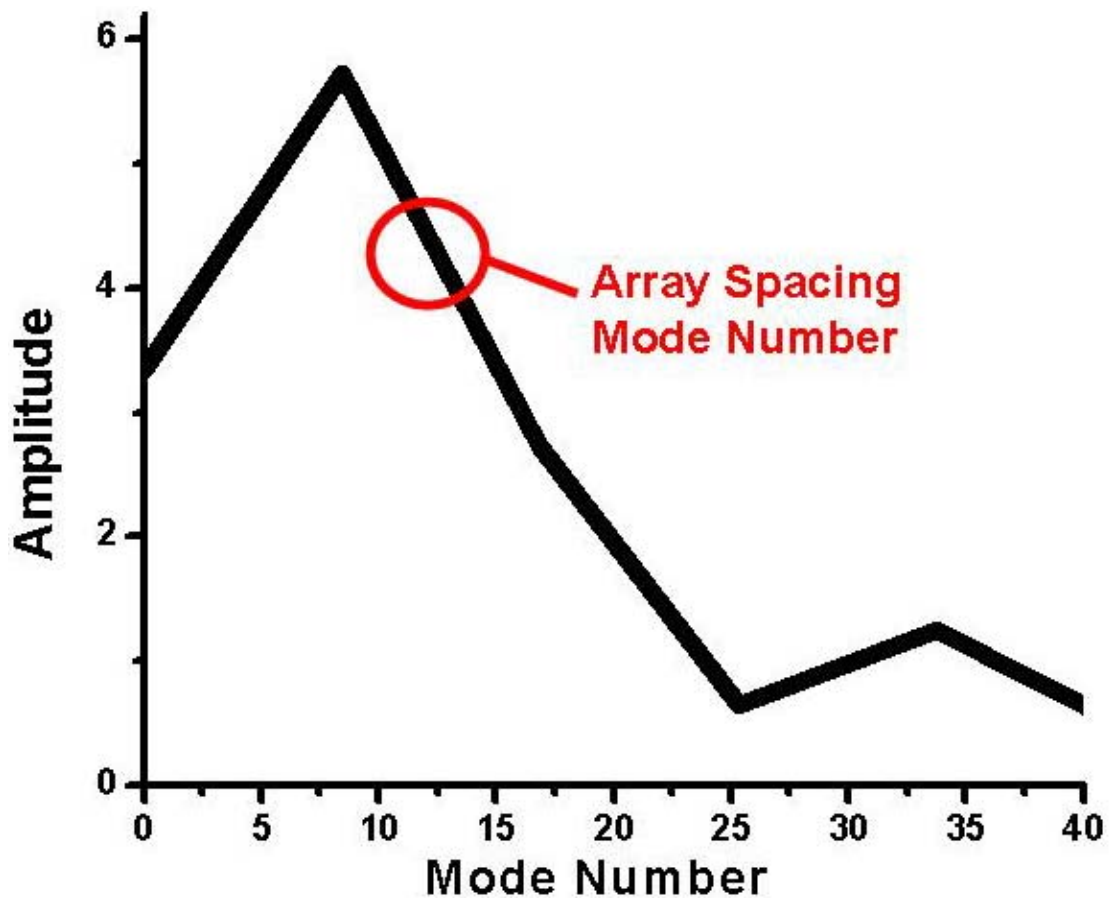


Figure 56. Sample Fourier transform plot for perturbations on blast waves traveling in helium gas and passing a 4 mm spaced wire array. The mode number corresponding to the wire array spacing at the radius where the blast wave intersected the array is 12.2. There is no peak at this point but the measured amplitude can still be measured and compared to theory.

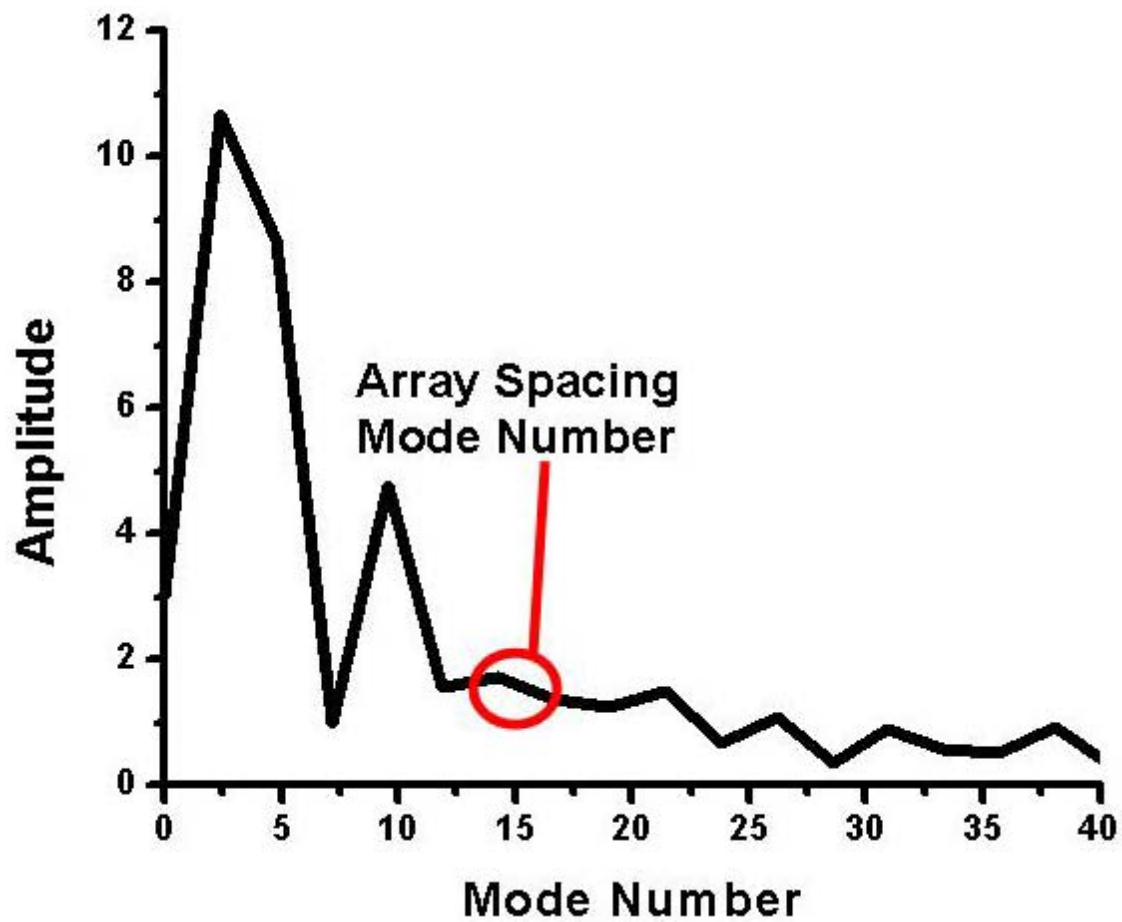


Figure 57. Sample Fourier transform plot for perturbations on blast waves traveling in a gas mixture of nitrogen and xenon and passing a 4 mm spaced wire array. The mode number corresponding to the wire array spacing at the radius where the blast wave intersected the array is 16.5. There is no peak at this point but the measured amplitude can still be measured and compared to theory.

7.3.4 Comparison of Experimental Results to Theory

As has been mentioned, growth or damping rates for the Vishniac overstability depend on two variables, the mode number, determined by the wire spacing of our arrays, and the polytropic index. Estimates for the polytropic index were obtained in different ways for the various gasses. For gasses where radiation is important, nitrogen and the mixed gas in our experiments, the temperature of the gas changes with time as the blast wave expands and radiation escapes. As the blast wave cools, the importance of radiation decreases and the polytropic index increases. Therefore for these gasses it may be true that there is no one polytropic index that is correct for all times, but that a range of polytropic indices apply over time.

For blast waves in helium gas radiation plays almost no part in the evolution as has been shown earlier in this chapter and so the behavior is that of an ideal monatomic gas. Such gasses have an adiabatic index of 1.67. This adiabatic index should be constant throughout the blast wave lifetime and so helium gas provides a valuable baseline test for quantitative comparison to theory.

Blast waves traveling in mixed gas were impossible to simulate due to the lack of a reliable equation of state for such gasses. For this data we relied solely on the polytropic index implied by comparison to theory. The polytropic index of blast waves in nitrogen gas can be estimated from the simulations described in chapter 4. This includes the simulations of Laming and Grun^{33, 34}, which predict a polytropic index ranging from 1.1-1.23 and our own Hyades simulations which estimate the polytropic index at 1.25.

To provide a consistency check of the simulation results for blast waves in nitrogen we used the theory by Liang and Keilty³⁰ described in section 2.5. Given the density ratio from Hyades along with the amplitude and exponent from the trajectory fit, this theory provides predictions for the importance of radiation, the polytropic index of the post-radiative-cooling gas, and the size of the initial energy deposition area,.

From the temporal exponent of the trajectory and the polytropic index implied by Hyades, we get an estimate for the value of the polytropic index of the post-radiative-cooling gas of 1.36 ± 0.12 . From these values and the trajectory amplitude and assuming that the energy in the blast wave is the initial laser energy, we can obtain an initial energy deposition area of 120 μm to 350 μm . This is consistent with the focal properties of the laser. The focal spot of the Z-Beamlet laser varies from 70 μm to 300 μm depending on the heat load of the laser. The final prediction we can gather is the fraction of energy lost due to radiation at the blast wave front, ϵ , would have to be 0.24. An ϵ of 0 indicates no net energy loss via radiation, while an ϵ of 1 indicates the fully radiative case, commonly referred to as the pressure driven snowplow. The theory of Laming and Grun³³ predicts an ϵ of 0.17 for our shock velocity.

One caveat to these results is the theory of Liang and Keilty assumes that ϵ is constant. The predictions of Laming and Grun show that this is not the case early on, but that the vast majority of the change in ϵ occurs before the blast wave slows to 45 km/s. This implies that at the point where we induce perturbations on the blast wave, the value of ϵ has already reached at point where it does not change much and we can apply the predictions of this theory. In total, the predictions resulting from the application of this theory seem consistent with the experiment and simulations.

We compare our helium experimental results with the predictions of Ryu and Vishniac¹⁹ in Figure 58. For helium, the experimental data closely matches the theoretical predictions for an adiabatic index of 1.67. This matches our assumption of what the adiabatic index should be. For the mixed gas there seems to be a sharp difference between the polytropic index implied by the highest mode number array and that implied by the other two arrays as seen in Figure 59. For the wider two arrays, the implied adiabatic index seems to be between 1.1 and 1.2, while for the final point the implied adiabatic index is closer to 1.3. Since data for all three points were taken over two experimental runs at the laser facility, it seems unlikely that there was any variation in the laser that would specifically affect experiments on one array and not the others. There is a possibility that the induced perturbations wavelength for this array is close to the thickness of the blast front and in this regime the blast wave's behavior is not well described by theory. This possibility is somewhat unlikely though, as the blast wave thickness should vary proportionally to the polytropic index. Therefore the higher polytropic index gasses should have thicker blast fronts and should see the same effect for the high mode number arrays. In the theory of Ryu and Vishniac it can be seen that the imaginary component of the temporal exponent of the perturbation evolution increases with increasing mode number. Therefore, the oscillation speed of the higher mode number blast waves should be higher. It may be possible that the higher mode number perturbations in the mixed gas are partially decreasing in size due to their oscillating behavior. Since the mixed gas is significantly heavier than the nitrogen or helium gasses, the time scales for the blast wave evolution are correspondingly longer and the oscillation behavior may have more of an effect, explaining the discrepancy

between this data and that of the other gasses. However, it is also true that the mixed gas data is the most difficult to analyze and that the higher mode number data is the most complicated. It may simply be that there is not enough data to statistically overcome the uncertainties associated with this particular experimental setup.

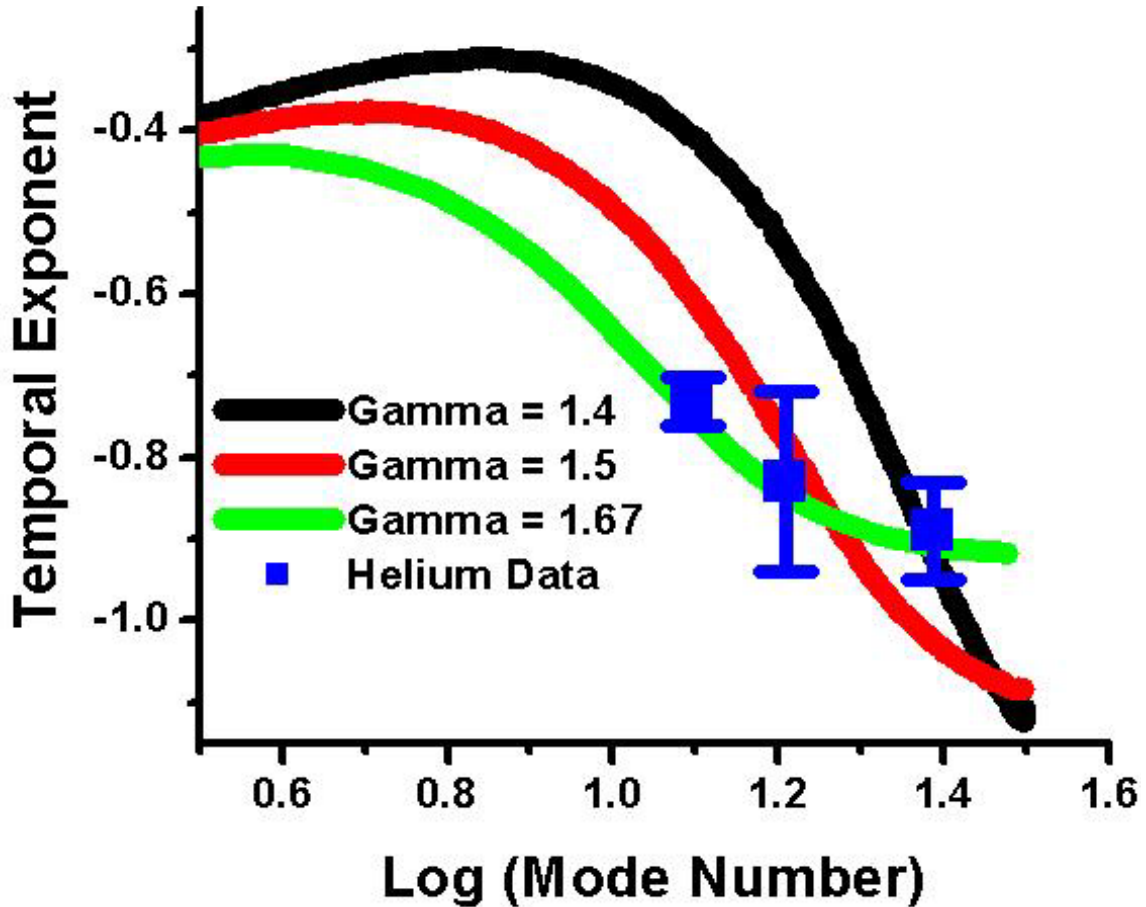


Figure 58. Comparison of experimental data for the temporal decay of perturbations on blast waves in helium (blue squares) to theoretical predictions for various polytropic indices (gammas). The data closely agree to the theoretical predictions for a polytropic index of 1.67, which matches the adiabatic index for an ideal monatomic gas.

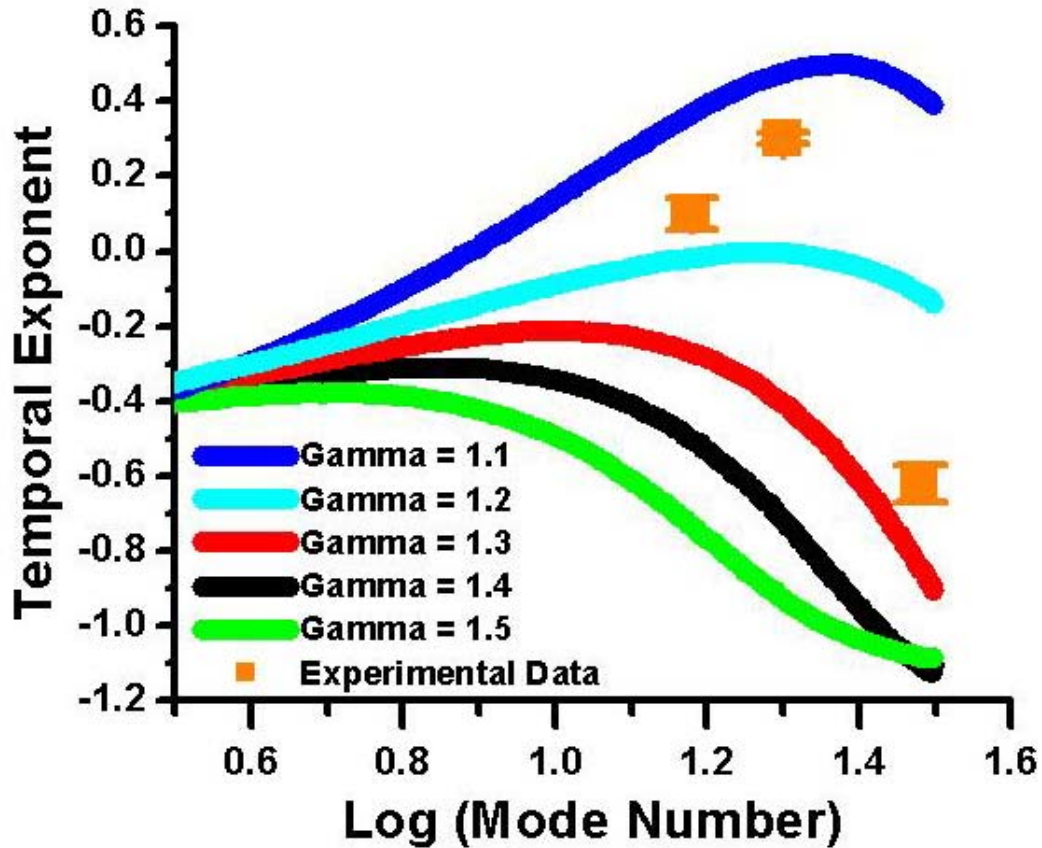


Figure 59. Comparison of experimental data for the evolution of perturbations on blast waves traveling through a mixture of nitrogen and xenon (orange squares) with theoretical predictions for various polytropic indices (gammas). The data points at lower mode number seem to imply a polytropic index between 1.1 and 1.2. The final data point is more consistent with a polytropic index of 1.3.

The experimental results for nitrogen seem most consistent with the predictions for a polytropic index of 1.4 as seen in Figure 60. However, the experimental data cannot exclude polytropic indices of 1.3-1.5. These values are all somewhat higher than the polytropic indices suggested by simulations, and are significantly different from the polytropic index of 1.1 suggested by the newer predictions of Laming and Grun³⁴. There are several possibilities for this discrepancy. The first possibility is the experimental data could be in error, possibly due to the sources of modal noise mentioned earlier.

Alternately, the mismatch with the theory curves from the work of Vishniac and Ryu¹⁹

could be because the effect of significant pressure in the pre-shock plasma due to preheating is not included.. For example, in these experiments the precursor is ionized 2.5 times on average indicating that the precursor region is heated to several eV. This degree of ionization and the implied temperature are significantly higher than appear in the simulation results, and would make the gas less compressible, raising the effective polytropic index.

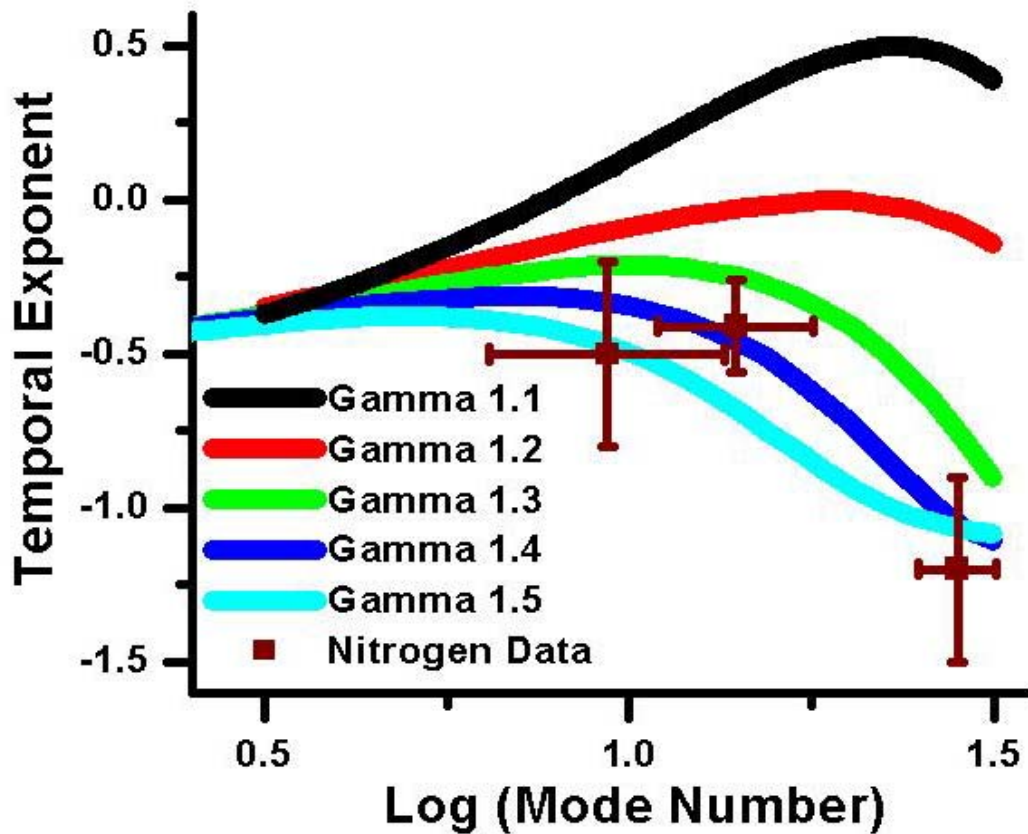


Figure 60. Comparison of experimentally determined decay rates for the amplitude of perturbations on blast waves traveling in nitrogen (brown squares) to theoretical predictions for various adiabatic index (gamma) gases.

7.4 Conclusions

We have shown that we are producing radiating blast waves and that the strength of radiation varies with the type of background gas, proportionally to its atomic number. In addition, we have shown that care must be taken in conducting these experiments as the passage of the drive laser used to create our blast waves can have a significant effect on the subsequent evolution of the blast wave created in the region of the drive laser's focal cone.

Finally we have reported the results of measurements of the temporal evolution of perturbations induced on the surface of high Mach-number blast waves. The results of these measurements would seem to generally confirm the published theoretical predictions of Vishniac et al.¹⁷⁻¹⁹ For blast waves in helium where radiation is minimal the experimental results agree with the theoretical predictions with a high degree of accuracy. In gasses where radiation plays a more significant role interpreting the results is more complicated. Because the temperature and thus the amount of radiation emitted changes in the blast waves as a function of time it is difficult to assign a single polytropic index to these blast waves. In addition, the presence of the radiative precursor preceding these blast waves adds an additional complicating factor. However, we can say that the general dependence of the perturbation evolution on mode number and polytropic index is as described in theory.

8. Conclusion

8.1 Summary

The goal of this work has been to experimentally measure the properties of high mach-number blast waves. Specifically, we have looked at the evolution of perturbations on the surface of these blast waves. Understanding how these perturbations evolve provides insight into the origin of structure seen in radiative supernova remnants (SNRs) that may play an important role in star formation. The primary method of study in this thesis is tracking the evolution of perturbations on laser produced blast waves induced by means of wire arrays and comparing the results to the published theories of Vishniac et al.¹⁷⁻¹⁹

In order to explain fully the physics of the perturbations measured, in chapter 2 of this thesis I have described the physics of disturbances in fluids leading to a discussion of shock waves and then blast waves. I have also discussed the various effects of radiation on blast waves and then in chapter 3 described the physics of the supernova remnants for which the original theory was developed, including a discussion of scaling laws to simulate these remnants in the laboratory.

In chapter 4 I summarized the results of simulations of both astrophysical and laboratory blast waves that have been performed. The astrophysical simulations confirm the mechanism causing the structure on the SNRs and some of the specific growth rates predicted. Simulations performed both in support of previously published experiments and our specific experiments are described. They provide predictions for the properties

of laser produces blast waves (including the polytropic index of the shocked gas) that can be used to assist in the comparison of theory to experiment.

I then provide a detailed description of the setups used for experiments performed on both the Janus laser at Lawrence Livermore National Laboratory and the Z-Beamlet laser at Sandia National Laboratories and describe how the various diagnostics fielded during these experiments work. Diagnostics fielded include several types of interferometers as well as a schlieren telescope.

Finally, I describe the results of the various experiments we performed. The first result of the experiments was the confirmation that radiation plays a role in the blast waves we produce and that the amount of radiation varied with the atomic number of the background gas used in the experiment. The next experimental result is that the drive laser used to create our blast waves creates a warm channel in the background gas in the region of its focal cone that affects the evolution of the blast wave that area. The final experimental result is the measurement of the evolution of perturbations induced by means of regularly spaced wire arrays on blast waves traveling in a number of different background gasses. The variation of background gas and spacing of the wire arrays allowed variation of the two main variables expected to control the evolution of the induced perturbations: the mode number of the perturbation and the polytropic index of the shocked gas. The comparison of our experimental results to theory showed general agreement with the published theory.

8.2 Future Work

There are a number of directions in which this work could be potentially extended. Since the original theoretical work of Vishniac et al.¹⁷⁻¹⁹ was developed to understand structure on supernova remnants, it would be useful to make the experiments more closely match these phenomena. The two main paths toward doing this are to further examine cases where growth of perturbations is expected and to look at perturbation evolution in collisionless shocks. In addition, it may strengthen the conclusions contained herein if data were collected over a wider range of perturbation mode numbers.

8.2.1 Growth of Perturbations

The most obvious next step in continuing these experiments would be to further examine perturbations under conditions where growth is expected. The mixed gas data presented in chapter 7 hints at growth, but the signal to noise ratio is poor and there is no readily available equation of state for such a mixed gas to enable easy modeling. There are two potential ways that these problems can be avoided. More data on the mixed gas would allow us to statistically overcome the poor signal to noise ratio and draw stronger conclusions about whether or not growth is occurring. Alternatively, instead of a mixed gas, blast waves could be created in krypton gas, for which the equation of state is known. This gas has a slightly lower atomic number than xenon (36 as compared to 54) but still a significantly higher one than nitrogen (atomic number 7). The radiation from such blast waves should then have an intermediate amount of radiation, and may act

much like blast waves in the mixed gas. Since the equation of state for krypton gas is known, it should be possible to model blast waves in krypton which would further strengthen the comparison to theory.

8.2.2 Collisionless Shocks

The other major means by which this work could be brought more in line with the astrophysical case is to look at collisionless shocks. By reducing the pressure of background gas in the chamber to less than one Torr (thus also reducing the gas' density and increasing the mean free path of gas particles) and applying a large magnetic field (greater than 1 Tesla), the ion gyroradius of the gas could be brought below the mean free path of the particles. This would cause the major energy dissipation mechanism in a blast wave traveling through this low density gas to become magnetic turbulence instead of particle collisions and bring the experiment closer in line with the astrophysical situation since all SNRs are collisionless shocks. Performing this experiment would allow the impact of magnetic fields on the evolution of perturbations to be discerned. In addition, by using techniques such as Faraday rotation³⁸, the structure of the magnetic fields in these blast waves could be explored. This in itself would be of interest in the astrophysical community. Finally, it is believed that many cosmic rays have their origin in supernova remnants due to the interplay of the shock and the magnetic field⁴⁴. By creating a similar type of shock we could look for ion acceleration and study the physics of cosmic rays.

8.2.3 Extension of Mode Numbers

Acquiring data from a larger number of perturbation mode numbers would strengthen the conclusions presented in this work. Looking at higher mode number would be difficult as the features would be smaller compared to the overall blast wave and either the resolution of the optical setup would have to be improved or one small section of the blast wave would have to be focused on. The difficulty with choosing one section to focus on is that this section would constantly move with time, meaning the region of focus would have to change with every shot. If one were instead to look at lower mode number perturbations, it might be more practical. In order to look at lower mode number perturbations, a larger angular region of the blast wave would need to be examined in order to induce enough wavelengths of the perturbation to avoid any edge effects and limit the induced modal content. This would require redesigning the target and wire array. The target would need to become more mass limited in order to remove the low mode number noise in the blast wave. One way to do this would be to change the target to a flat plastic disk with a radius similar to that of the current wire target (0.5 mm) but a thickness that is substantially smaller (0.1 mm or less). This would lessen the ellipticity of the created blast waves and the low mode number noise. The wire array would have to be redesigned to allow for a larger angular fraction of the blast wave to be perturbed and pass through the array. This could possibly be done by designing an array with two flat circular plates attached by a single bar and machined with matching grooves for stringing the wires through.

8.3 Conclusions

The field of laboratory astrophysics is rapidly growing thanks to our ability to access ever more exotic states of matter in the laboratory. As our observational ability continues to grow, we increasingly rely on complex computer codes to understand the wealth of phenomena we see. Validation and verification of these codes is important if we are to believe their results and this task is only possible through comparison with the results of experiments designed to simulate some aspect of an astrophysical phenomenon. As the field of laboratory astrophysics continues to grow, we will be able to understand more and more of the amazing phenomena we see throughout the universe.

References

- 1 A. H. Nelson, Reports on Progress in Physics **63**, 1851 (2000).
- 2 J. M. Dawson, The Physics of Fluids **7**, 981 (1964).
- 3 H. Takabe, Progress of Theoretical Physics Supplement, 202 (2001).
- 4 R. W. Boyd, *Nonlinear optics* (Academic Press, San Diego, CA, 2003).
- 5 D. Strickland and G. Mourou, Optics Communications **56**, 219 (1985).
- 6 N. C. Woolsey, Y. A. Ali, R. G. Evans, et al., Physics of Plasmas **8**, 2439 (2001).
- 7 M. S. Wei, S. P. D. Mangles, Z. Najmudin, et al., Physical Review Letters **93**
(2004).
- 8 S. C. Wilks, H. Chen, E. Liang, et al., Astrophysics and Space Science **298**, 347
(2005).
- 9 Y. P. Zakharov, Ieee Transactions on Plasma Science **31**, 1243 (2003).
- 10 B. A. Remington, R. M. Cavallo, M. J. Edwards, et al., Astrophysics and Space
Science **298**, 235 (2005).
- 11 D. Ryutov, R. P. Drake, J. Kane, et al., Astrophysical Journal **518**, 821 (1999).
- 12 A. R. Miles, M. J. Edwards, and J. A. Greenough, Astrophysics and Space
Science **298**, 17 (2005).
- 13 O. Sadot, K. Levy, A. Yosef-Hai, et al., Astrophysics and Space Science **298**, 305
(2005).
- 14 S. Bouquet, C. Stehle, M. Koenig, et al., Physical Review Letters **92** (2004).
- 15 M. J. Edwards, A. J. MacKinnon, J. Zweiback, et al., Physical Review Letters **87**,
art. no. (2001).
- 16 J. Grun, J. Stamper, C. Manka, et al., Physical Review Letters **66**, 2738 (1991).
- 17 E. T. Vishniac, Astrophysical Journal **274**, 152 (1983).
- 18 D. Ryu and E. T. Vishniac, Astrophysical Journal **368**, 411 (1991).
- 19 D. Ryu and E. T. Vishniac, Astrophysical Journal **313**, 820 (1987).
- 20 B. G. Elmegreen and D. M. Elmegreen, Astrophysical Journal **220**, 1051 (1978).
- 21 G. Welter and J. Schmidburgk, Astrophysical Journal **245**, 927 (1981).
- 22 J. M. Blondin, E. B. Wright, K. J. Borkowski, et al., Astrophysical Journal **500**,
342 (1998).
- 23 M. M. MacLow and M. L. Norman, Astrophysical Journal **407**, 207 (1993).
- 24 L. D. Landau and E. M. Lifshits, *Fluid mechanics* (Pergamon Press, Oxford,
England ; New York, 1987).
- 25 D. Mihalas and B. Weibel-Mihalas, *Foundations of radiation hydrodynamics*
(Dover, Mineola, N.Y., 1999).
- 26 I. A. B. Zel*dovich, I. U. P. Raizer, W. D. Hayes, et al., *Physics of shock waves
and high-temperature hydrodynamic phenomena* (Academic Press, New York,,
1966).
- 27 L. Sedov, Prikl. Mat. Mekh. **10**, 241 (1946).

- 28 G. B. Rybicki and A. P. Lightman, *Radiative processes in astrophysics* (Wiley,
New York, 1979).
- 29 L. D. Landau and E. M. Lifshits, *The Classical theory of fields* (Butterworth
Heinemann, Amsterdam ; Boston, 2003).
- 30 E. Liang and K. Keilty, *Astrophysical Journal* **533**, 890 (2000).
- 31 R. S. Sutherland and M. A. Dopita, *Astrophysical Journal Supplement Series* **88**,
253 (1993).
- 32 C. F. McKee and B. T. Draine, *Science* **252**, 397 (1991).
- 33 J. M. Laming and J. Grun, *Physical Review Letters* **89** (2002).
- 34 J. M. Laming and J. Grun, *Physics of Plasmas* **10**, 1614 (2003).
- 35 J. T. Larsen and S. M. Lane, *Journal of Quantitative Spectroscopy & Radiative
Transfer* **51**, 179 (1994).
- 36 J. A. Glaze, W. W. Simmons, and W. F. Hagen, *Status of large neodymium glass
lasers* (Soc. Photo-Optical Instrumentation Engrs, Palos Verdes Estates, CA, USA
Reston, VA, USA, 1976).
- 37 P. K. Rambo, J. L. Porter, G. R. Bennett, et al., *OSA Trends in Optics and
Photonics, Conference on Lasers and Electro-Optics* **73**, 362 (2002).
- 38 I. H. Hutchinson, *Principles of Plasma Diagnostics* (Cambridge University Press,
New York, 1987).
- 39 N. Fröman, P. O. Fröman, and ebrary Inc., *Physical problems solved by the
phase-integral method* (Cambridge University Press, Cambridge ; New York,
2002).
- 40 S. G. Taylor, *Proc. Roy. Soc. A* **201**, 159 (1950).
- 41 E. Cohen, T. Piran, and R. Sari, *Astrophysical Journal* **509**, 717 (1998).
- 42 *CALE Users Manual* (Lawrence Livermore National Laboratory, 1991).
- 43 A. D. Edens, T. Ditmire, J. F. Hansen, et al., *Physics of Plasmas* **11**, 4968 (2004).
- 44 A. M. Hillas, *Journal of Physics G-Nuclear and Particle Physics* **31**, R95 (2005).

Vita

Aaron Douglas Edens was born in Ft. Worth Texas on November 1, 1978, the son of Gene and Lynn Edens. After completing his work at J.J. Pearce High School, Richardson, Texas he entered Harvey Mudd College in Claremont, California.

Permanent Address: 5836 Mossbrook Tr., Dallas, TX, 75252

This dissertation was typed by the author.